THE UNIVERSITY OF CHICAGO

DESIGN, SYNTHESIS, AND CHARACTERIZATION OF NON-FULLERENE ACCEPTORS FOR ORGANIC SOLAR CELLS

A DISSERTATION SUBMITTED TO
THE FACULTY OF THE DIVISION OF THE PHYSICAL SCIENCES
IN CANDIDACY FOR THE DEGREE OF
DOCTOR OF PHILOSOPHY

DEPARTMENT OF CHEMISTRY

BY
DONGLIN ZHAO

CHICAGO, ILLINOIS
DECEMBER 2016

Table of Contents

List of figures

List of Tables

ACKNOWLEDGEMENT

I would like to thank Prof. Luping Yu for giving me the opportunity to work in his group for five years. The constant guidance he gave during my PhD has been extremely valuable and has allowed me to overcome the difficulties I encountered. If there is one thing to take away from all his mentoring, it would be to always look beyond the surface and think critically about it. It has been a great honor working under Prof. Yu for my PhD degree.

I would also like to thank Prof. Viresh Rawal and Prof. Dmitri Talapin for agreeing to serve on my dissertation committee.

I want to thank the past and present Yu group members for their help in my research, in particular Dr. Qinghe Wu, Dr. In Hwan Jung, and Dr. Zhengxu Cai for offering their advices and working with me on solar sell acceptor project. Thank you to my lab mates Alex, Wai-yip, Valerii, and Andriy. It has been a pleasure working with you all.

Also thank you to Dr. Qiti Guo, Dr. Justin Jureller, Dr. Antoni Jurkiewicz and Dr. Jin Qin for their help with various equipment and measurements.

Chapter 1 Introduction

This chapter contains parts of the published work [Lu, L.; Zheng T.; Wu Q.; *et al. Chem. Rev.* **2015**, 115, 12666–12731] Copyright (2015) American Chemical Society.

1.1 Organic solar cells

1.1.1 Introduction

Solar energy is the largest source of clean and renewable energy that is poorly utilized by human society. Extensive research is pursued worldwide to change that scenario. Strategies were developed to convert solar energy to electricity or chemical fuels so that they can be stored in the forms other than light. Research and development of photovoltaic solar cells (mainly based on inorganic semiconductors) is a part of the effort in solar energy harvest. Organic solar cells (OSCs) provide an alternative way to utilize solar energy to inorganic solar cells. Compared to inorganic counterparts, organic solar cells hold the promise because they are flexible and lightweight, and can be produced via low-cost bulk synthesis and wet solution processing.

Introduced in 1986 by C.W. Tang, the first organic solar cell was made via layer-by-layer high-vacuum evaporation of p-type (electron donor) and n-type (electron acceptor) small molecules. The efficiency of this bilayer solar cell was close to 1%. [1] However, bilayer devices require costly and lengthy vacuum deposition or unorthodox solvent choice, both of which limit the research progress. Moreover, exciton diffusion length in organic semiconductors is typically in the scale of 10 nm, meaning most excitons generated far away from the p-n interface in bilayer devices are wasted without generating charges.

The next breakthrough of OSC research was the introduction of bulk heterojunction (BHJ) structure instead of bilayer structure in the active layer. Fabrication of BHJ active layer can be easily achieved by spin-coating or roll-to-roll printing of mixed stock solution containing both donor and acceptor directly onto electrodes. Not only does this method greatly reduce production cost and make material design easier, but it also leads to more efficient OSCs. In this method, donor and acceptor can form interpenetrating network with a domain size similar to exciton diffusion length, resulting in higher charge generation rate. Currently the state-of-the-art BHJ solar cells can achieve more than 10% power conversion efficiencies.

Structure of OSC consists of a transparent conductive electrode which allow light goes in, the organic active layer (mostly BHJ) sandwiched between two thin charge-selective layers, and a metal counter electrode. Depending on which kind of charge is collected by the transparent electrode and the metal electrode, device structures are grouped into ‘conventional’ or ‘inverted’ (Figure 1.1). The device structure of conventional devices is ITO electrode/hole transporting layer/active layer/electron-selecting layer/counter electrode, while that for Inverted devices is ITO electrode/electron selective layer/organic active layer/hole selective layer/counter electrode. Conventional or inverted device structure is selected according to the energy levels of the active layer and the vertical distribution of the active layer components. Generally inverted structure is more chemically stable in long term and is more widely adopted in recent research.

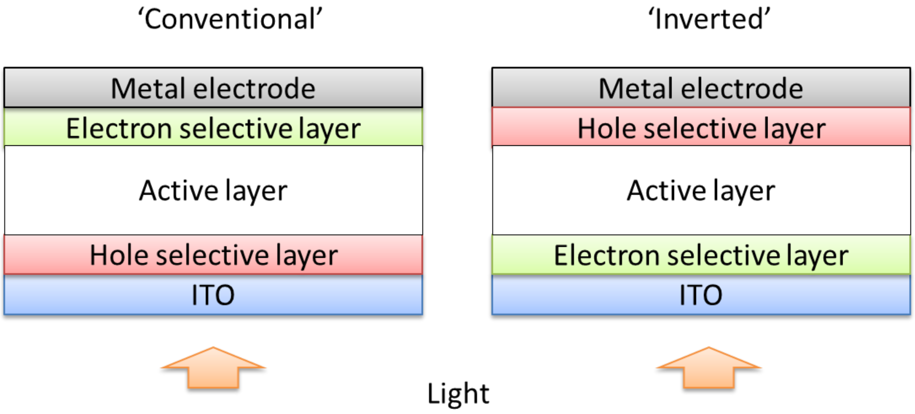

Figure 1.1 Device structures of organic solar cells.

Our research focuses on developing materials for the active layer, where charges are generated upon irradiation. Normally, the active layer consists of two organic components, p-type electron donor material and n-type electron acceptor material.

The working mechanism of OSC is summarized as followed. When light excites the organic material, electron on the HOMO will be excited to the LUMO forming an exciton. The exciton moves to the donor-acceptor interface and undergoes charge separation, leaving a positive charge on the donor and a negative charge on the acceptor. If this bonded electron-hole pair can overcome the coulomb attraction, free charge carriers can be generated. Current can then be generated provided that these free charge carriers can make their way to the corresponding electrodes before recombining with the counter charge.

Considering the charge generation mechanism, ideal OSC materials should at least have: wide absorption spectrum and high optical absorption coefficient for higher number of generated charge carriers; high charge carrier mobility for more efficient charge transport in order to minimize quenching; optimized solubilizing groups and crystallinity for ideal phase separation of donor and acceptor when the film was forming, generating interpenetrating network with domain size of 10 nm scale.

1.2 Parameters

The performance of solar cell is generally evaluated by four parameters: short circuit current (J_{sc}), open circuit voltage (V_{oc}), fill factor (*FF*), and power conversion efficiency (PCE). An example of typical current density-voltage (*J*-*V*) curve is shown in Figure 1.2 with the parameters labeled. In organic solar cells, each of the parameters reflects some properties of the device.

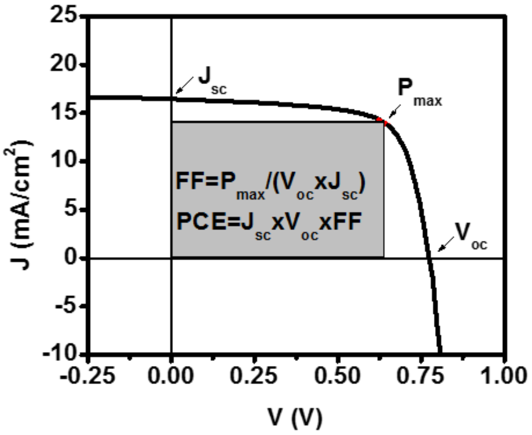

Figure 1.2 Typical *J-V* parameters of solar cell

J_{sc} - J_{sc} is correlated with charge carriers generated upon irradiation. Materials with wider absorption spectrum and higher absorption coefficient are desired, since more photons can be absorbed to generate excitons.

V_{oc}- Although V_{oc} is determined by multiple physical properties, such as the dielectric constant of the material, the morphological grain size, and the structure of donor/acceptor interface, an empirical method to predict V_{oc} of a BHJ device is from the difference between the HOMO of the acceptor and the LUMO of the donor.[2,3]

FF- Fill factor is the 'squareness' of the J-V curve. *FF* is affected by multiple parameters, and is ascribed to be correlated with the charge carrier mobility. In most cases, BHJ film with pure and interpenetrating small domains has better *FF* value. [4,5]

PCE- Or Eff, is the overall power conversion efficiency.

1.2.1 Donor materials

Since the first OSC reported by C.W. Tang, efficiency of single junction OSCs have been improved from 0.95% to over 10%. Most efforts and improvements have been made in donor small molecules and polymers. Here several most studied or successful donor materials are listed. Structures of the representative donor materials are shown in Figure 1.3. Unless otherwise stated, all devices mentioned in this section employ PCBM as the acceptor.

P3HT was one of the most studied donor polymers. BHJ devices using PCBM as acceptors typically yield 5% PCE.[6] Although the performance efficiency of **P3HT** has been surpassed by many new generation donor polymers, it is still a strong candidate for bulk production and commercialization due to its simple structure. It is also commonly used in physical studies and theoretical modeling.

PTB7 developed in our group is a bench mark which started the era of low bandgap donor-acceptor (D-A) polymers.[7] **PTB7-Th**, a **PTB7** derivative with thieno-alkyl side chain, is still one of the best performing donor polymers. It is now commercially available as PCE-10. Over 10% was achieved by **PTB7-Th**/PCBM device through careful device engineering.

Following the success of highly amorphous low bandgap polymers such as the **PTB7** and **PTB7-Th** series, semi-crystalline low bandgap polymers are developing rapidly recently as a new family of efficient solar cell donors, already achieving 9 to 10% efficiency.[8-10] The common feature of this new family of donor polymer is that they all contain few un-alkylated thiophenes in the backbone, resulting in the polymer having strong tendency toward aggregation. Aggregation in the solid state can be confirmed from the large red shift observed in the UV-Vis absorption spectrum. This aggregation behavior is also highly temperature-dependent. Another feature of semi-crystalline donor polymers is that the optimal device thickness is usually 200-300nm, which is much thicker than the 80-100nm optimum thickness for amorphous donor polymers. An example of a semi-crystalline donor polymer is the polymer **PffBT4T-2OD** shown in Figure 1.3 developed by the He group. This material is commercialized with the name of PCE-11. Excellent performance of **PffBT4T-2OD** greatly relies on the careful design of the size and branching position of the alkyl chain, otherwise the desired pure but small-sized polymer phase could not be formed in the blend film. The best efficiency achieved by **PffBT4T-2OD**/$PC_{71}BM$ is 10.5%, with a V_{oc} of 0.77 V, a J_{sc} of 18.4 mA/cm^2, and a *FF* of 0.76. The *FF* value for this device is higher than that for amorphous donor material devices because of the enhanced charge mobility in the semi-crystalline polymers.

Some newly emerging wide bandgap polymers also show promising results. Polymer **PDBT-T1** achieved 9.7% with $PC_{71}BM$.[11] Although wide band gap polymers do not have optimal optical absorption at higher wavelength compared with low bandgap donors, they can be good donors when coupled with small band gap acceptors to achieve wide spectrum coverage.

Although most advances in solar cell donors are polymer materials, small molecule materials also show good potential. The BHJ morphology of small molecule devices are more difficult to control than in polymer devices. However with careful molecular structure design and blend film process condition engineering, high efficiency can be achieved. One of the best example is ***p*-DTS(FBTTh$_2$)$_2$** developed by Bazan and coworkers.[12,13]

Other efforts to boost the BHJ efficiency include, but not limited to, processing additive[14], interfacial engineering[15,16], annealing and post processing, ternary active layer, and building tandem cells[17].

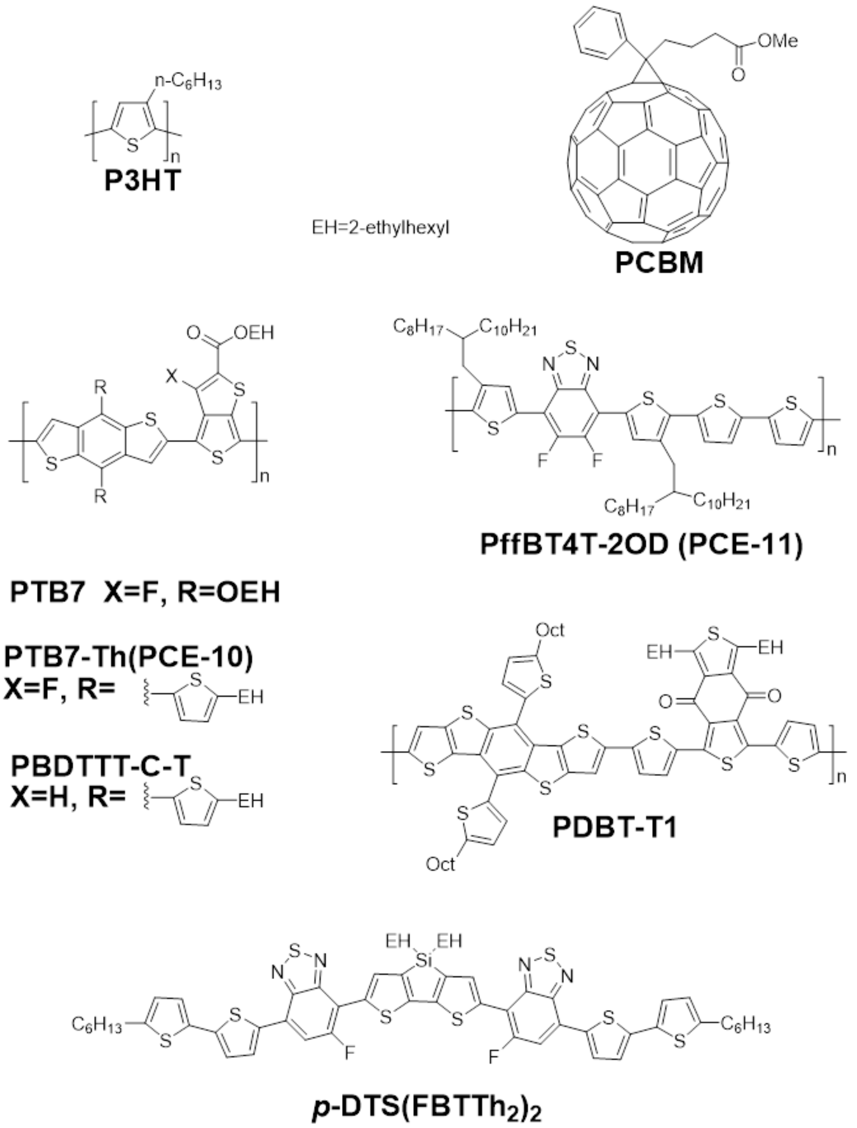

Figure 1.3 Structures of representative donor materials and PCBM.

1.3 Polymer non-fullerene acceptors

Although with fullerene acceptors exhibit excellent properties for solar cell applications due to their unique chemical structures, polymer acceptors have certain advantages, such as potentially lower cost and easier modification of optoelectronic properties.[18] At this stage, the development of all-polymer solar cells, which consist of both polymer donor and polymer acceptor, is still lagging behind that of polymer:PCBM system.

In this section, advances in non-fullerene polymer acceptors are discussed. Chemical structures of all the donor and acceptor polymers discussed in this section are summarized in Figure 1.4 and Figure 1.5. For polymer acceptors to be useful and competitive against fullerenes, the following features are desirable: (1) easy solution processing, (2) well-aligned HOMO and LUMO energy levels for efficient charge transfer with donor polymers, (3) strong and broad absorption in the visible range, (4) high electron mobility for efficient charge transport, (5) favorable molecular interactions and suitable miscibility with donor polymers to form phase separated BHJ structure. Polymer electron acceptors for OPVs are designed and synthesized with a similar pattern of extensively investigated donor polymers. Biggest difference between donor polymers and acceptor polymers is their HOMO and LUMO energy levels. To efficiently facilitate hole transfer from acceptor to donor and electron transfer from donor to acceptor, LUMO and HOMO energy levels of the acceptor must be lower than LUMO and HOMO of donor respectively. To lower the energy levels of polymers, electron withdrawing functional groups and moieties such as cyano, imide, and benzothiazole and perylenes are introduced to acceptor polymers.

1.3.1 Benzothiadiazole based polymer acceptors

The benzothiadiazole (BT) unit exhibits the low lying energy levels that are necessary to be utilized as a building block for acceptor polymers. Huch and co-workers reported all-polymer solar cells based on the **P3HT:PF8TBT** system with a PCE of 1.9%. They were able to control nanostructure morphology of the active layer through a double nanoimprinting process.[19] The domain sizes can be as small as 25 nm. Later, Yu *et al.* also demonstrated the ability to control the morphology of the **P3HT:PF8TBT** system by forming **P3HT** crystalline nanowires which achieved a very high V_{oc} of 1.35 V and an overall PCE of 1.87%.[20]

Miyake and co-workers studied the effects of acceptor polymer molecular weight on the solar cell performance of the **P3HT:PF12TBT** devices.[21] When the molecular weight of **PF12TBT** increased from 8.5 to 78 kg/mol, PCE was enhanced from 1.8% to 2.7%. The enhancement was attributed to more optimal blend morphology in the high molecular weight device after thermal annealing, which provided efficient avenues for charge generation and transport.

The Pei group replaced thiophenyl groups in the traditional TBT unit with thiazole units to produce TABT.[22] The LUMO energy levels of the resulting polymer **DTABT-IDT** decreased from -3.21 eV to -3.45 eV compared to the original polymer

DTBT-IDT. This change to the energy level was responsible for an enhancement of the electron mobility by two orders of magnitude. In addition, better miscibility with **P3HT** was observed for the **DTABT-IDT** based polymer compared to **DTBT-IDT**, resulting in a PCE of 1.18% for the **P3HT:DTABT-IDT** system compared to 0.58% for the **P3HT:DTBT-IDT** system.

Yao *et al.* demonstrated a bilayer **P3HT:PIDSe-DFBT** device with a PCE of 2.5% by optimizing each component in the all-polymer solar cell.[23] In this case, the BHJ structure was replaced by bilayer to reduce bimolecular recombination which had resulted from the unfavorable formation of large separated domains. NPE-PEIE was used to modify ZnO interface to increase V_{oc} and a co-solvent system was used to control the diffusion of **P3HT** into **PIDSe-DFBT**. The results illustrated the importance of optimizing processing conditions for all-polymer solar cell performance.

1.3.2 Perylene diimide based polymer acceptors

Perylene diimide (PDI) and its derivatives represent one of the most promising class of electron acceptors because of their outstanding chemical and physical properties, including high electron mobility, strong intermolecular π-π interactions, and high absorption coefficients.[24] In addition, the PDI molecule offers two positions for functionalization, one via substitution at the β-positions of the central perylene ring and another via substitution at the imide positions. Roy and co-workers reported a copolymer with perylene bisimide moieties as acceptor and phenylenevinylene as donor units attached to the imide position.[25] The corresponding polymer showed a high SCLC electron mobility at 8.5×10^{-3} cm^2/Vs with HOMO and LUMO energy levels at -5.75 eV and -3.95 eV, respectively. Solar cells made from this accepting polymer and **P3HT** as the donor material exhibited a PCE of 2.32% after the films were thermally annealed.

An electron transporting polymer based on PDI and dithienothiophene unit (PDI-DTT) was reported by Zhan *et al.*, which showed a high FET mobility at 1.3×10^{-2} cm^2/Vs.[26] The **PDI-DTT** showed a broad absorption in the visible range with an extension to the near-IR region. Solar cells fabricated from **PT1** and **PDI-DTT** gave a PCE of 1.48%. The same group investigated the application of **PDI-DTT** acceptor in large area devices with roll-to-roll processing with **PSBTBT** as the electron donor. However, a poor PCE of only 0.2% was attained.[27]

A series of D-A type polymers containing β-substituted PDI as electron-accepting (A) unit with various electron-donating (D) units such as thiophene, fluorene and carbazole were developed by Zhou *et al.*[28]. Two donor polymers, **P3HT** and **PT1**, were used to test the solar cell performance of the PDI based polymers. Compared to **P3HT**, **PT1** exhibited lower HOMO energy levels and better film morphology in the blends. Among all the devices, the combination between **PT1** and the carbazole based PDI polymer (**PC-PDI**) gave the best performance with V_{oc} of 0.70 V, J_{sc} of 6.35 mA/cm^2, *FF* of 50%, ultimately resulting in a PCE of 2.23%.

The Yu group recently developed electron-deficient TPTI and CN monomers and synthesized a series of alternating acceptor polymers containing different monomer combinations.[29] They found that the LUMO energy levels of the polymers were strongly dependent on the more electron deficient monomers while the HOMO energy levels were largely determined by the less electron deficient monomers. Fluorescent quantum yield was found to be closely related to the photovoltaic properties, indicating that internal polarization played a role in determining the photovoltaic properties. Among all the acceptor polymers investigated, polymer **PNPDI** gave the best performance with a PCE of 1.03% when **PTB7** was used as donor material.

PDI-2DTT, a 3-unit small molecule fragment of the polymer **PDI-DTT**, was used as a processing additive to improve the performance of **PBDTTT-CT:PDI-DTT** solar cells.[30] The use of PDI-2DTT smoothed the polymer domains and enhances donor/acceptor mixing for more efficient charge transfer, leading to an improvement of average PCEs from 1.16% to 1.43%. In addition, DIO facilitated the aggregation and crystallization of

PBDTTT-CT, leading to improved average PCEs of 2.92%. By combining the two additives together, PCE was further pushed to 3.45%.

To control phase separation, a novel strategy of introducing a small percentage of polystyrene side chain to the donor polymer was applied.[4] A series of isoindigo containing polymers were studied as donor polymers and a perylene tetracarboxlic diimide (PTCDI) based acceptor polymer **PTP** was used. Among the donor/acceptor combinations, **PiI-2T** donor showed highest PCE at 3.48%. After introducing 5 mol% polystyrene side chain, the efficiency was further increased to 4.21%, mainly due to the increase in J_{sc} from the decreased phase separation due to smaller domain length scales.

1.3.3 Naphthalene diimide based polymer acceptors

The polymer **N2200** (also named as P(NDI2OD-T2)) is the most thoroughly studied polymer acceptor so far. Composed of NDI and bithiophene moieties, **N2200** was first reported for use in organic thin film transistors.[31] A high electron mobility of 0.45-0.85 cm^2/Vs was demonstrated for **N2200** under ambient conditions in combination with Au contacts and various polymeric dielectrics. Later, it was introduced as an acceptor material for all-polymer photovoltaic devices.

At the initial efforts by Moore *et al.*,[32] despite the high electron mobility, deep LUMO energy level and a complementary absorption with **P3HT**, the efficiency of **P3HT**:**N2200** device was only 0.2% with very poor J_{sc} and *FF*. They found that fast geminate recombination within 200 ps of excitation resulted in the low J_{sc}. This was due to a poor morphology with widely varied and overly large domain sizes up to 1 micron in the blend. Fabiano *et al.* found that due to balanced electron and hole mobility, high *FF* approaching 70% could be achieved in **P3HT**:**N2200** devices.[33] Later, Neher and co-workers solved the strong tendency for **N2200** to aggregate by using suitable solvents with large and highly polarizable aromatic cores.[34] The pre-aggregation could be completely suppressed and intermixing between **P3HT** and **N2200** was increased. Further tuning of donor/acceptor ratios, spin casting conditions and additives pushed efficiency to 1.4% due to improved morphology, which led to improved J_{sc}.

Fabiano *et al.* further showed that by using different solvents, the film morphology of **P3HT**:**N2200** could be controlled, resulting in changes to the hierarchical structure, polymer aggregations, and phase separations.[35] Both solar cell devices and FET devices were fabricated and studied. By using the Xylene:CN co-solvents, laterally phase-separated blends were obtained, leading to a high solar cell performance with a PCE of 1.31%. When DCB was used as processing solvent, the device showed large and balanced ambipolar field effect mobility, but unfortunately solar cell performance diminished.

To address the low photocurrent generation, Schubert *et al.* studied the processes that controlled free charge carrier generation for **P3HT**:**N2200** devices.[36] They correlated the amount of photocurrent produced to the polymer crystallite orientations. EQE results indicated that both donor and acceptor polymers contributed to current generation, however, the acceptor only contributed 1/2 to 1/3 of the donor. After the addition of CN (1-Chloronaphthalene) additive, **N2200** domains became smaller and **P3HT** domains became more pure. By increasing the amount of CN, **N2200** stacking changed from face-on to edge-on. This indicated that face-to-face stacking of the donor and acceptor polymer crystals is necessary to generate free charges, while miss-oriented chains inevitably cause geminate recombination and loss of excitons.

Schmitt-Mende *et al.* introduced a comb-like bilayer structure for **P3HT**:**N2200** devices.[37] The bilayer structure was achieved via photo-crosslinking of the **N2200** network followed by solution deposition of **P3HT**. They found that when the interfacial area was increased by this process, J_{sc} increased due to enhanced exciton separation while V_{oc} was slightly decreased due to increased bimolecular recombination. They proposed that the ideal morphology should not only consider D/A domain sizes, but also the spatial arrangement.

In addition to using **P3HT** as the donor polymer, several other donor polymer systems are studied with **N2200** as acceptor. Ito and co-workers used PTQ1 as the donor polymer and achieved a large PCE of 4.1%.[38]

Tang *et al.* reported all-polymer BHJ PSCs with **PTB7** as the donor and **N2200** as acceptor.[39] The two polymers exhibited complimentary absorption spectra. Both electron transfer from **PTB7** to **N2200** and hole transfer from **N2200** to **PTB7** were observed by EQE spectra. Morphology showed crystalline **N2200** domains dispersed in amorphous **PTB7** and a **N2200** rich top layer was shown in the device. A modest PCE of 1.1% was achieved. Later, Marks and co-workers tuned the morphology of **PTB7**:**N2200** devices via careful selection of processing solvents.[40] Morphology, charge transport property and solar cell performance of the corresponding devices are found to be sensitive to the processing solvents. Xylene processed films exhibit significantly more ordered π-π stacking for the two polymers with higher mobility for both electrons and holes. A PCE of 2.66% was realized when xylene was used as the solvent, which was much higher than devices fabricated with CB (1.35%) and chloroform (1.78%).

Kim and co-workers achieved over 4.5% PCE by using **PTB7**-Th and **N2200** blends as the active layer materials.[41] Morphology studies showed that the blend had highly intermixed domains in the BHJ due to low interfacial tension. Also, face on π-π stacking of **PTB7-Th** and **N2200** domains was shown to be emphasized in the optimized devices as observed in X-ray data. The processing additive DIO, was shown to be crucial to device performance by increasing the crystalline characteristics of **N2200** together with the appearance of highly ordered polymer organizations with face-on geometry, which largely enhanced electron mobility and J_{sc} in the devices. In parallel, Ito and co-workers achieved a PCE of 5.73% for **PTB7-Th**:**N2200** devices with a maximum EQE of ~60%.[42] Authors ascribed the success to high charge generation and collection efficiency (both over 80%), which was comparable to those in efficient polymer:PCBM devices.

Yan and co-workers mixed **N2200** with the donor polymer NT and achieved a high PCE of 5.0% with a high J_{sc} of 11.5 mA/cm^2.[43] The high J_{sc} is attributed to low bandgap of the donor polymer and favorable morphology in the blend films. Detailed studies indicated that donor polymer NT maintains its crystallinity with a face-on orientation in the BHJ blends, resulting in a high hole mobility that was balanced with the electron mobility of **N2200**.

Recently, McNeill and co-workers achieved >4% PCE for all-polymer solar cells based on a BFS4:**N2200** blend.[44] V_{oc} of the best device reached 0.9 V, which is the highest value for **N2200** devices. The blends showed a coarse phase separated morphology with domains of a semicrystalline nature. In addition, the top surface of the blends was found to be 100% BFS4 while the bottom surface showed a mixed composition roughly correlated to the overall blend ratio, indicating vertical phase separations. TA spectra revealed that device efficiency was limited by incomplete exciton separation and high geminate recombination.

Became the standard of polymer acceptors, **N2200** enjoyed more efficiency enhancement and mechanistic study since 2015. **N2200** enjoyed more efficiency enhancement and mechanistic study.[45-49] One of the interesting studies was done by the Marks group and coworkers, where relationship of molecular weight M_n of both donor and acceptor polymer is studied. Most studies so far employ the same acceptor while varying Mn of donor polymer, which generally lead to conclusion that the higher the M_n the better the efficiency.[49] However in this recent work, by varying M_n of both donor polymer and acceptor polymer, the authors found that the best combination is not the highest Mn for both, but a ‘sweet point’ in the middle. [48] This work implies that to achieve high performance in all polymer solar cell, donor and acceptor need to have proper match.

Champion efficiency of all polymer solar cell is 8.27% PCE of **N2200** and specially developed wide band gap polymer. [50]Absorption of **N2200** peaks at 400nm and 800 nm, with low absorption coefficient between 450-to 650nm. This feature determined that to achieve high efficiency instead of widely used low bandgap polymer, wide band gap polymer that has complimentary absorption could be better donor. In addition to designing new donor polymers, adding commercial available wide bandgap polymer as ternary additive also boosted efficiency of **PTB7-Th**/**N2200** device to 6.7%[47]

Another polymer containing NDI and selenophene units shows great potential towards application in all-polymer solar cells.[51] Jenekhe and co-workers reported using a NDI-selenophene copolymer (PNDIS-HD) as the acceptor and a thiazolothiazole copolymer (PSEHTT) as the donor with a PCE of 3.3%. Selenophene containing polymers have higher electron mobility than their thiophene counterparts, which is ascribed to better orbital overlapping from the larger π orbitals in the selenium atom. The crystalline morphology of PNDIS-HD also helped to achieve balanced charge mobility in the blends. Later, the same group enhanced the performance of PSEHTT:PNDIS-HD devices by using CB/DCB co-solvents with a 9:1 volume ratio.[52] Co-solvents reduced polymer domain sizes (to 20-40 nm) on the surface of the active layer compared to films processed from CB (>100 nm) and suppressed bimolecular recombination. In addition, in the co-solvent system, carrier mobilities were found to be even further balanced. A PCE of 4.8% was achieved with a high J_{sc} of 10.5 mA/cm^2. The performance of PSEHTT:PNDIS-HD could also be improved through side chain engineering of PNDIS acceptor. By tuning the ratios of 2-decyltetradecyl (DT) and 2-butyloctyl (BO) side chains on the backbone, crystallinity and electron mobility could be optimized, resulting in a PCE of 4.4%.[53]

Finally, Zhou *et al.* reported all-polymer solar cells based on **PTB7** as donor and a NDI family copolymer based on naphthodithiophene diimide as acceptor monomer and bithiophene as the donor to produce the polymer (PNDTI-BT-DT) as an acceptor material.[54] PNDTI-BT-DT showed strong absorption in the near infrared region. A PCE of 2.56% was attained with CF as the solvent.

Accepting polymer is developed by modifying donor polymer moieties to make them more electron deficient. For example, Janssen group synthesized an acceptor polymer PDPP2TzT which was based on DPP units by replacing the two thiophene units in the high performance donor polymer PDPP3T[55] with two thiazole units. PDPP2TzT exhibited deep HOMO and LUMO energy levels at -5.63 eV and -4.00 eV, high electron mobility, and a broad absorption range up to 850 nm. By mixing with the structurally similar donor polymer PDPP5T and carefully optimizing processing conditions, a PCE of 2.9% was accomplished.[56]

Research on acceptor polymers is advancing quickly in recent years. In order to be viable, they will need to exhibit similar features to PCBM both electrochemically and morphologically in the BHJ active layer when combined with donor polymers. The electrochemical features have thus far proved relatively easy to properly engineer, with promising properties such as complementary absorption with donor, low lying energy levels, and certain dipole moment. However, molecular engineering of the morphology of all polymer devices has proved more difficult as compared to polymer:fullerene devices. For example, phase separated domain sizes and intermixing between donor and acceptor are hard to control. Detailed theoretical computing may help to address this issue.

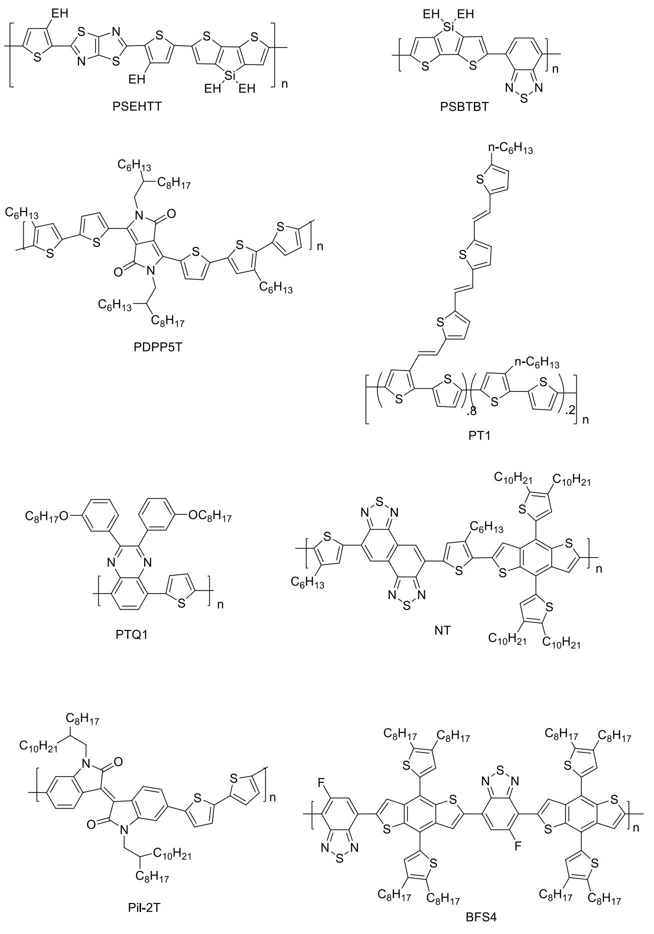

Figure 1.4 Chemical structures of all the donor polymers used in all-polymer solar cells discussed in this section.

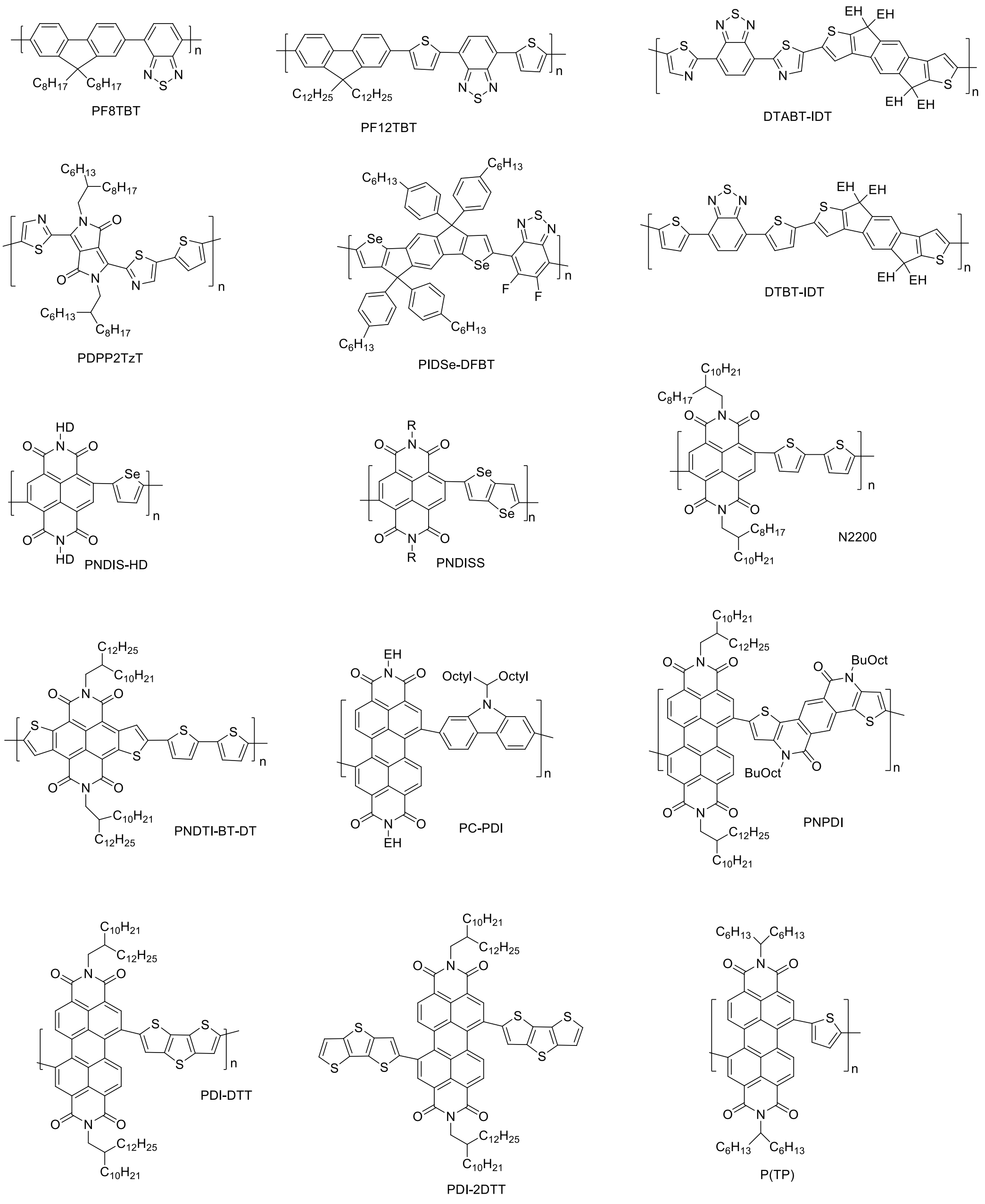

Figure 1.5 Chemical structures of all the acceptor polymers used in all-polymer solar cells discussed in this section.

1.4 Small molecule based non-fullerene acceptors

Other than polymers, small molecules are also good candidates for acceptors.

Small molecules have intrinsic advantage over polymers for they are easier to be purified and quality-controlled, thus eliminating the batch-to-batch variation that exists for polymers.

Initailly, miscibility between donor polymer and acceptor small molecules presents challenges to prepare uniform films. Thus vacuum deposited bilayer structured non-fullerene devices were pursued at early stage of acceptor research. [57,58]

1.4.1 Non-PDI acceptors

When the search for non-fullerene acceptors just started in early 2010s, there was no clear guideline for molecular design and a variety of structures were tested by using benchmark donor polymer **P3HT**. [59-62] Efficiency of early-generation acceptors could hardly achieve 1% PCE.

Later on, with the emergence of push-pull type high efficiency donor polymer such as **PTB7** and **PTB7-Th**, and better understanding of design principles of acceptor materials, efficiency of non-fullerene acceptors enhanced dramatically over the past few years.

Ladder shaped molecules with electron rich core and electron withdrawing flanked groups on two ends was shown to be an effective design idea. Electron withdrawing end groups includes naphthalene imide, rhodanine,

One of the good examples is the rhodanoine flanked ladder shape acceptor, **FBR** shown in Figure 1.6, first reported in 2014 by McCulloh group.[63] Acceptor molecule **FBR** was built via simple two steps synthesis procedure, cross coupling of fluorene core with benzothiadiazole, followed by condensation with rhodamine end capping groups. The central fluorene unit provides an aromatic and rigid core for the molecule; benzothiadiazole further extends the conjugation along the molecule while introducing some electron deficiency, and strong electron withdrawing rhodamine flank groups are capped at the two ends of the molecule. Solubilizing alkyl chains are introduced to central electron rich fluorene area, so that it won't affect intermolecular packing and charge transporting along the electron deficient wings of the molecules. DFT modeling suggests FBR has a twisted structure, which may prevent the formation of undesired large crystalline domains. Inverted solar cell devices were fabricated using **FBR** as acceptor and **P3HT** as donor, and 4.1% was achieved. This PCE is quite impressive because the optimized devices based on **P3HT**/ fullerene acceptor $PC_{71}BM$ could only reach 5%. In the same work, the authors fabricated **P3HT**/$PC_{61}BM$ under similar condition for control experiment, which actually yielded lower PCE (3.5%) than **FBR**. The higher OPV performance of **FBR** mainly comes from the higher LUMO level of **FBR** (-3.57eV for **FBR** VS -3.84eV for PC61BM) which enables the high V_{oc} value of the solar cell (0.82V for **FBR** vs 0.59V for PC61BM). Ultrafast transient absorption spectroscopy was used to study charge generation process and result suggests that charge carriers are generated faster in **P3HT/FBR** blend film due to interpenetration morphology of donor and acceptor. **IDTBR**, a ladder shape acceptor highly resembles **FBR** but with longer center core unit, was reported later by the same group.[64] By replacing fluorene core with indacenodithiophene, **IDTBR** has strong absorption coefficient, red-shifted absorption which is complimentary with **P3HT**, and has more pristine domain in bulk hetero-junction blend. Best efficiency achieved with **P3HT** was 6.4%, which is highest record for non-fullerene **P3HT** devices.

NIDCS is another example of linear structured molecule with strong electron withdrawing end group. First reported by Park group in 2014, **NIDCS/P3HT** device gave 2.7% efficiency.[65] By carefully choosing semi-crystalline **PPDT2FBT** as donor polymer and annealing condition, efficiency of 7.6% was achieved with high V_{oc} of 1.03V and high FF of 0.63.[66] Small molecular donor/ small molecular acceptor devices with ***p*-DTS(FBTTh$_2$)$_2$** can also achieve satisfying efficiency of 5.3% by carefully control device morphology. [67]

One of the most successful non-fullerene acceptor is **ITIC**, a nearly-ladder-shaped molecule composed of a planer backbone and perpendicular 4-hexyl-phenyl side chain. This rigid out-of-plane side chain is introduced to modify crystallinity and to prevent excessive self-aggregation of large conjugation back bone. The back bone consists of central 7 member ring aromatic electron rich core (indacenodithieno[3,2-b]thiophene) and two strong electron withdrawing pendants (2-(3-oxo-2,3-dihydroinden-1-ylidene) malononitrile) on each side. The A-D-A structure enables intramolecular charge transfer, thus enhancing optical absorption.

First reported in 2015, **ITIC** initially show 6.8% PCE with **PTB7-Th** as the donor. [68] The PCE is inferior to PCBM partially due to **ITIC** and **PTB7** or **PTB7-Th** has overlapped optical absorption, and the blend film lacks utilization of photons below 500nm.

Compared to PDI based acceptors which absorb mainly between 400-500nm, **ITIC**'s max absorption reside at 600-780nm.

As the one of the most well-studied non-fullerene acceptor, huge amount of device fabrication results show that a matching donor polymer is important for achieving high PCE. The champion polymer for fullerene may not be the ideal one for non-fullerene acceptor. **ITIC** absorbs in 600-780 which is similar to low bandgap donors, so medium bandgap donors are developed to replace them. After side chains are carefully adjusted, PCE values of 9.5% was achived.[69]

Highest non-fullerene BHJ solar cell performance is 11%, achieved via **ITIC** and wide bandgap and crystalline polymer PBDB-T.[70] **PBDB-T**/**ITIC** device showed 16.80

mA/cm$_2$ J_{sc} which is much higher than reference **PBDB-T**/PC$_{71}$BM device which has J_{sc} of 12.80mA/cm2. The enhanced J_{sc} is due to **ITIC**'s strong absorption at 700-800 nm which PCBM device does not absorb at all. High fill factor value over 0.70 and approaching 0.75 for best devices is ascribed to highly balanced electron and hole mobility of blend device. The e/h mobility ratio is less than 1.5 which is very small for non-fullerene solar cells.

Tetraazabenzodifluoranthene Diimides (BFI), an 11 member ring ladder type heterocyclic monomer was designed and synthesized as a new candidate for n-type semiconductor.[71] Nitrogen in hetero cycle was to reduce energy levels and extended conjugation and flat geometry was to increase intermolecular orbital overlap and to enhance charge transport. An electron acceptor molecule **DBFI-T** was built by linking two of BFI monomers with a thiophene monomer in the middle and two phenyl end groups on two sides. This large (2nm by size), x shaped molecule showed superior charge generation and electron accepting effects when blended with donor polymer **PSEHTT** and PCE higher than 5% was achieved.[72] By engineering dihedral angle between the two BFI monomers of acceptor molecule, as well as fine-tuning device composition, efficiency as high as 8.5% was achieved.[73]

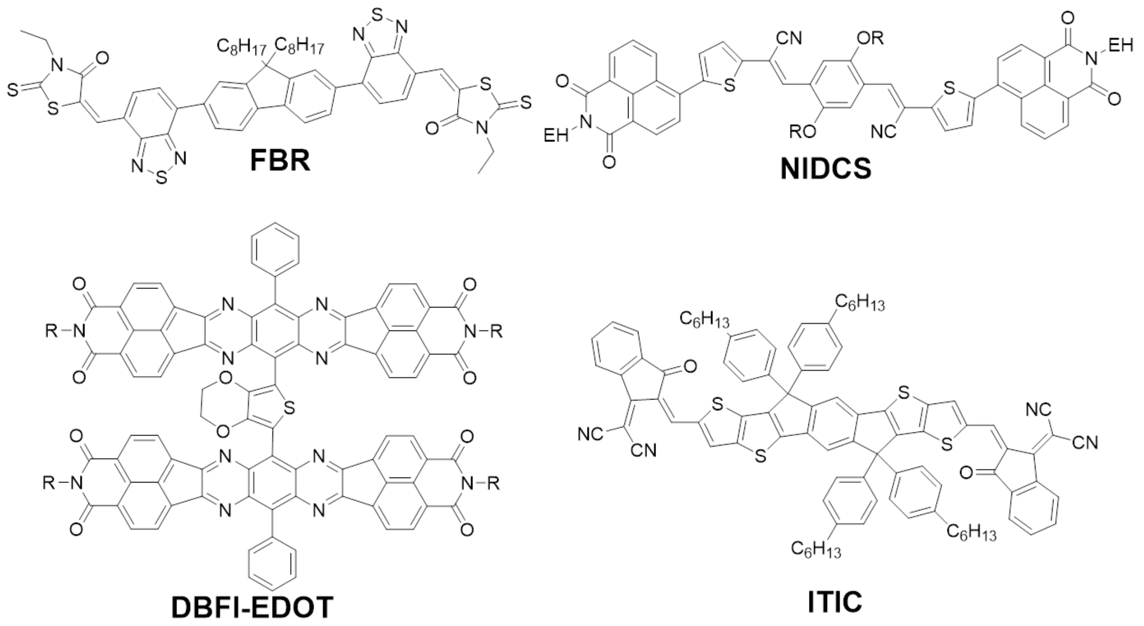

Figure 1.6 Representative small molecule acceptors.

1.4.2 Perylene Diimide based acceptors

As a commercial available pigment, perylene diimide is one of the best candidates for solar cell acceptors for its high absorption coefficient, high chemical stability, high electron affinity, and low cost. However, efficiency of perylene diimide acceptors was impaired by oversized PDI crystalline and trapped charge carriers in large crystals. Modified PDI with interrupted pi stacking is desired. [74], [75]

Although after careful device morphology control, mono PDI and **PBDTTT-C-T** device could achieve 3.7% PCE, and all small molecule device with ***p*-DTS(FBTTh$_2$)$_2$** as donor achieved 3.1% PCE, structural engineering of PDI is highly on demand for higher performance.[76,77]

One attempt to alleviate aggregation was to link PDI dimers through imide nitrogen atoms and forms a head-to-head dimer. (Also referred as **H-diPDI,** H is for it was produced by hydrazine reacted with perylene anhydride). First of all non-planar structure should lead to weaker pi-pi interaction and better solubility and miscibility with donor materials. Another concern of designing non-planar PDI acceptors is that by enlarging donor/acceptor distance at the BHJ interface, charge separation could be facilitated. As expected J_{sc} of dimer device was significantly enhanced by 10 folds compared to PDI monomer, proofing introducing non-planar arranged PDIs could be a valid way circumventing undesired over phase separation. [78,79]

Introducing steric hindrance to bay area of PDI is one of the most commonly applied methods to alter their solubility and packing properties. Since substitutions on bay position are conjugated with PDI aromatic core, altering bay substitution changes not only configuration but also electronic properties. [80-82]

SdiPDI, two PDIs directly connected at bay position via single bond was reported with high PCE. Efficiency as high as 6.29% was achieved with **PTB7-Th** as donor polymer and PDI derivative modified electron transport layer. However if the PDIs are forced to be co-plane by forming two parallel bonds at both beta position, the PCE was not diminished, indicating twisted PDI dimers are necessary.[83,84,85] **SdiPDI** can also be further modified by incorporating hetero atoms to outside bay-positions to form **SdiPDI-S**. Incorporation of heteroatom sulfur into PDI backbone resulted in elevated LUMO energy level and larger dihedral angle between the two PDI units. Instead of commonly used low band gap donors such as PCE-10 or PCE-11, **SdiPDI-S** was reported to work most efficiently with wide bandgap donor **PDBT-T1** to give 7.16% PCE. [11]

Fusing two PDI with an ethylene group in the middle could force the two PDIs form helical geometry. Helical PDI dimer (**Helical PDI 1**) was first reported by Nuckolls group in 2015, followed by expanding the design idea to four parallel PDIs, **hPDI4**. [86,87] With **PTB7-Th** as donor, helical dimer device gave 6.05% PCE and tetramer gave 8.3% with high fill actor value of 0.68.

Besides linking two beta-PDIs directly, inserting electron-rich linker between the two beta-substituted PDIs can fine-tune the energy levels and packing properties. One successful example is single thiophene linked diPDI, **Bis-PDI-T-EG**, developed by Yao's group. [81,88]

Another high-performing di-PDI is spirofluorene-linked diPDI, **SF-PDI2**. Efficiency of **SF-PDI2** devices highly relies on donor material. While amorphous **PTB7-Th** donor only gave 3% PCE, semi-crystalline donor **PffBT4T-2DT** doubles the efficiency to 6.3%.[82] By using a novel low bandgap high aggregating donor polymer **P3TEA**, efficiency as high as 9.5% was achieved with high V_{oc} value of 1.11V.[89] These results suggest that choosing the proper door material is of importance.

Cyclizing bay area of PDI with electron-rich linker is another way to tune both electron affinity and molecular geometry of the acceptor. Elimination of the intramolecular donor-acceptor charge transfer widened acceptor’s bandgap and enhance V_{oc} of the device.[90]

Other that imide N position and bay position, α position is another chemically modifiable position on PDI monomer. PDI with four substituents on all alpha positons were synthesized to evaluate their effect on PDI monomer packings. [91]

3D structure with three or four PDI connected to a core is another way to control extent of aggregation and intermolecular charge transport. A tri-PDI acceptor was reported by Zhan group in 2014, using triphenylamine (TPA) to hold together three PDI units (**S-(TPA-PDI**)).[92] Because of the sp^3 hybridized nitrogen in the center, the whole molecular geometry is propeller shaped. Using **PBDTTT-C-T** donor polymer and DIO as processing additive, 3.3% PCE could be achieved; proofing 3D multi-PDI should be a valid design concept.

The success of fullerene generates from its favorable phase separation and isotropic charge transport. To mimic this unique feature, highly spherical shaped 3D structures are designed and tested. Multiple examples of tetra PDI compounds have been published since 2015. The tetra-functinalized center linker can be tetraphenyl methane/silane/germane[93], tetraphenyl ethylene[94,95] , tetraphenylpyrazine[95], or spiro-fluorene (**SF-PDI4**)[96,97].

One of the earlier and representative result is tetraphenylethylene cored tetra PDI, **TPE-PDI4**, developed by He group. [94] Tetraphenethylene was chosen as core for the phenyl groups can form a propeller structure and hold four PDIs in 3D structure. At the same time, biphenyl diPDI was synthesized as a linear geometry control compound. Solar cell devices of **TPE-PDI4** or diphenyl diPDI and **PTB7-Th** were fabricated and evaluated. **TPE-PDI4** devices showed 5.5% PCE which was among the highest at that time, while PDI dimer device only gave 3.1% PCE. The outstanding performance was ascribed to 3D interconnecting charge transfer channels among the PDIs. It is worth to mention that, 3D geometry that mimics fullerenes is beneficial in designing other electron accepting moieties. [98,99]

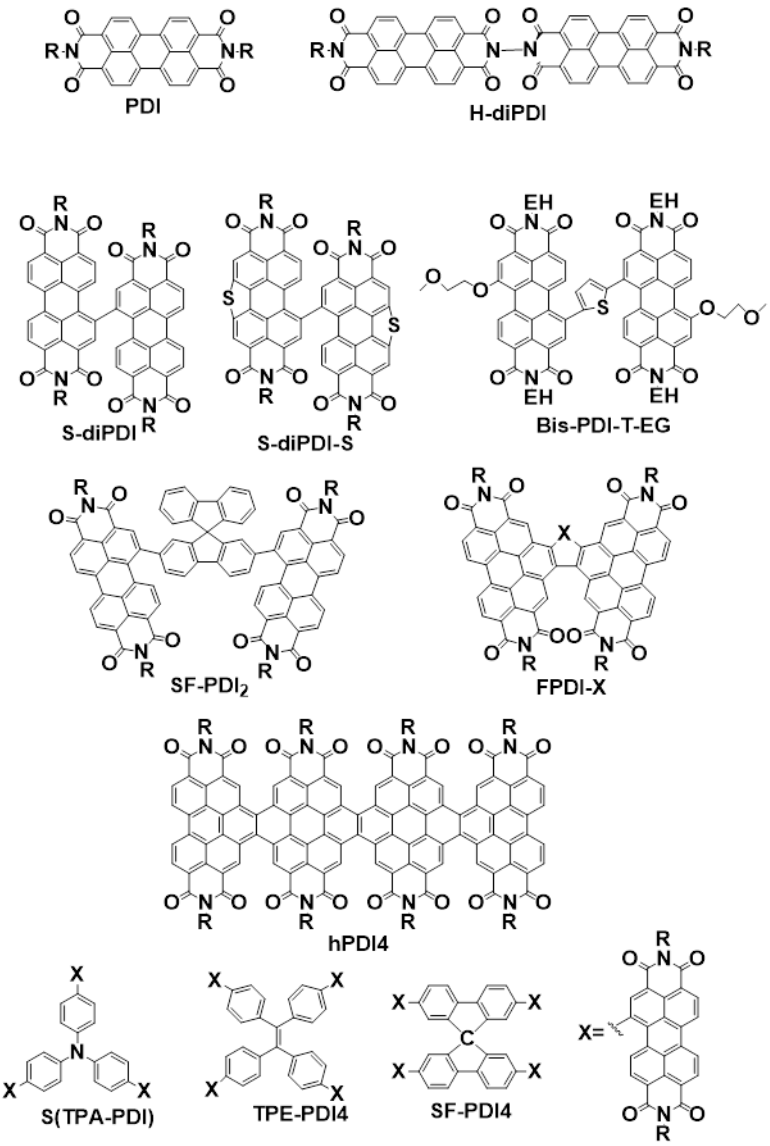

Figure 1.7 PDI-based non-fullerene acceptors.

1.5 Conclusion

In this chapter, I presented a brief overview on the background of organic solar cell and focused my attention on reviewing the development of non-fullerene acceptors and its status. The general conclusion is that non-fullerene acceptors have the potential to rival the fullerene as electron acceptor, which is the initial motivation we had in my research effort.

1.6 References

(1) Tang, C. W. *Applied Physics Letters* **1986**, *48*, 183.

(2) Scharber, M. C.; Mühlbacher, D.; Koppe, M.; Denk, P.; Waldauf, C.; Heeger, A. J.; Brabec, C. J. *Advanced Materials* **2006**, *18*, 789-794.

(3) Burke, T. M.; Sweetnam, S.; Vandewal, K.; McGehee, M. D. *Advanced Energy Materials* **2015**, *5*, n/a-n/a.

(4) Zhou, Y.; Kurosawa, T.; Ma, W.; Guo, Y.; Fang, L.; Vandewal, K.; Diao, Y.; Wang, C.; Yan, Q.; Reinspach, J.; Mei, J.; Appleton, A. L.; Koleilat, G. I.; Gao, Y.; Mannsfeld, S. C. B.; Salleo, A.; Ade, H.; Zhao, D.; Bao, Z. *Advanced Materials* **2014**, *26*, 3767-3772.

(5) Bartesaghi, D.; Perez Idel, C.; Kniepert, J.; Roland, S.; Turbiez, M.; Neher, D.; Koster, L. J. *Nat Commun* **2015**, *6*, 7083.

(6) Dennler, G.; Scharber, M. C.; Brabec, C. J. *Advanced Materials* **2009**, *21*, 1323-1338.

(7) Liang, Y.; Xu, Z.; Xia, J.; Tsai, S. T.; Wu, Y.; Li, G.; Ray, C.; Yu, L. *Adv Mater* **2010**, *22*, E135-138.

(8) Liu, Y.; Zhao, J.; Li, Z.; Mu, C.; Ma, W.; Hu, H.; Jiang, K.; Lin, H.; Ade, H.; Yan, H. *Nat Commun* **2014**, *5*, 5293.

(9) Nguyen, T. L.; Choi, H.; Ko, S. J.; Uddin, M. A.; Walker, B.; Yum, S.; Jeong, J. E.; Yun, M. H.; Shin, T. J.; Hwang, S.; Kim, J. Y.; Woo, H. Y. *Energy Environ. Sci.* **2014**, *7*, 3040-3051.

(10) Zhao, J.; Li, Y.; Hunt, A.; Zhang, J.; Yao, H.; Li, Z.; Zhang, J.; Huang, F.; Ade, H.; Yan, H. *Adv Mater* **2015**.

(11) Sun, D.; Meng, D.; Cai, Y.; Fan, B.; Li, Y.; Jiang, W.; Huo, L.; Sun, Y.; Wang, Z. *Journal of the American Chemical Society* **2015**, *137*, 11156-11162.

(12) van der Poll, T. S.; Love, J. A.; Nguyen, T. Q.; Bazan, G. C. *Adv Mater* **2012**, *24*, 3646-3649.

(13) Kyaw, A. K.; Wang, D. H.; Wynands, D.; Zhang, J.; Nguyen, T. Q.; Bazan, G. C.; Heeger, A. J. *Nano Lett* **2013**, *13*, 3796-3801.

(14) Schmidt, K.; Tassone, C. J.; Niskala, J. R.; Yiu, A. T.; Lee, O. P.; Weiss, T. M.; Wang, C.; Frechet, J. M.; Beaujuge, P. M.; Toney, M. F. *Adv Mater* **2014**, *26*, 300-305.

(15) Yu, W.; Huang, L.; Yang, D.; Fu, P.; Zhou, L.; Zhang, J.; Li, C. *J. Mater. Chem. A* **2015**, *3*, 10660-10665.

(16) Lethy Krishnan Jagadamma , M. A.-S., Abdulrahman El-Labban ,; Issam Gereige , G. O. N. N., Jorge C. D. Faria , Taesoo Kim , Kui Zhao ,; Federico Cruciani , D. H. A., Martyn A. McLachlan , Pierre M. Beaujuge ,; Amassian, a. A. *Advanced Energy Materials* **2015**, *5*, 1500204.

(17) You, J.; Dou, L.; Yoshimura, K.; Kato, T.; Ohya, K.; Moriarty, T.; Emery, K.; Chen, C. C.; Gao, J.; Li, G.; Yang, Y. *Nat Commun* **2013**, *4*, 1446.

(18) Facchetti, A. *Materials Today* **2013**, *16*, 123-132.

(19) He, X.; Gao, F.; Tu, G.; Hasko, D.; Hüttner, S.; Steiner, U.; Greenham, N. C.; Friend, R. H.; Huck, W. T. S. *Nano Letters* **2010**, *10*, 1302-1307.

(20) Yu, W.; Yang, D.; Zhu, X.; Wang, X.; Tu, G.; Fan, D.; Zhang, J.; Li, C. *ACS Applied Materials & Interfaces* **2014**, *6*, 2350-2355.

(21) Mori, D.; Benten, H.; Ohkita, H.; Ito, S.; Miyake, K. *ACS Applied Materials & Interfaces* **2012**, *4*, 3325-3329.

(22) Cao, Y.; Lei, T.; Yuan, J.; Wang, J.-Y.; Pei, J. *Polymer Chemistry* **2013**, *4*, 5228.

(23) Yao, K.; Intemann, J. J.; Yip, H.-L.; Liang, P.-W.; Chang, C.-Y.; Zang, Y.; Li, Z. a.; Chen, Y.; Jen, A. K. Y. *Journal of Materials Chemistry C* **2014**, *2*, 416-420.

(24) Kozma, E.; Catellani, M. *Dyes and Pigments* **2013**, *98*, 160-179.

(25) Mikroyannidis, J. A.; Stylianakis, M. M.; Sharma, G. D.; Balraju, P.; Roy, M. S. *The Journal of Physical Chemistry C* **2009**, *113*, 7904-7912.

(26) Zhan, X.; Tan, Z. a.; Domercq, B.; An, Z.; Zhang, X.; Barlow, S.; Li, Y.; Zhu, D.; Kippelen, B.; Marder, S. R. *Journal of the American Chemical Society* **2007**, *129*, 7246-7247.

(27) Liu, Y.; Larsen-Olsen, T. T.; Zhao, X.; Andreasen, B.; Søndergaard, R. R.; Helgesen, M.; Norrman, K.; Jørgensen, M.; Krebs, F. C.; Zhan, X. *Solar Energy Materials and Solar Cells* **2013**, *112*, 157-162.

(28) Zhou, E.; Cong, J.; Wei, Q.; Tajima, K.; Yang, C.; Hashimoto, K. *Angewandte Chemie International Edition* **2011**, *50*, 2799-2803.

(29) Jung, I. H.; Lo, W.-Y.; Jang, J.; Chen, W.; Zhao, D.; Landry, E. S.; Lu, L.; Talapin, D. V.; Yu, L. *Chemistry of Materials* **2014**, *26*, 3450-3459.

(30) Cheng, P.; Ye, L.; Zhao, X.; Hou, J.; Li, Y.; Zhan, X. *Energy & Environmental Science* **2014**, *7*, 1351-1356.

(31) Yan, H.; Chen, Z.; Zheng, Y.; Newman, C.; Quinn, J. R.; Dotz, F.; Kastler, M.; Facchetti, A. *Nature* **2009**, *457*, 679-686.

(32) Moore, J. R.; Albert-Seifried, S.; Rao, A.; Massip, S.; Watts, B.; Morgan, D. J.; Friend, R. H.; McNeill, C. R.; Sirringhaus, H. *Advanced Energy Materials* **2011**, *1*,

230-240.

(33) Fabiano, S.; Chen, Z.; Vahedi, S.; Facchetti, A.; Pignataro, B.; Loi, M. A. *Journal of Materials Chemistry* **2011**, *21*, 5891.

(34) Schubert, M.; Dolfen, D.; Frisch, J.; Roland, S.; Steyrleuthner, R.; Stiller, B.; Chen, Z.; Scherf, U.; Koch, N.; Facchetti, A.; Neher, D. *Advanced Energy Materials* **2012**, *2*, 369-380.

(35) Fabiano, S.; Himmelberger, S.; Drees, M.; Chen, Z.; Altamimi, R. M.; Salleo, A.; Loi, M. A.; Facchetti, A. *Advanced Energy Materials* **2014**, *4*, n/a-n/a.

(36) Schubert, M.; Collins, B. A.; Mangold, H.; Howard, I. A.; Schindler, W.; Vandewal, K.; Roland, S.; Behrends, J.; Kraffert, F.; Steyrleuthner, R.; Chen, Z.; Fostiropoulos, K.; Bittl, R.; Salleo, A.; Facchetti, A.; Laquai, F.; Ade, H. W.; Neher, D. *Advanced Functional Materials* **2014**, *24*, 4068-4081.

(37) Pfadler, T.; Coric, M.; Palumbiny, C. M.; Jakowetz, A. C.; Strunk, K.-P.; Dorman, J. A.; Ehrenreich, P.; Wang, C.; Hexemer, A.; Png, R.-Q.; Ho, P. K. H.; Müller-Buschbaum, P.; Weickert, J.; Schmidt-Mende, L. *ACS Nano* **2014**, *8*, 12397-12409.

(38) Mori, D.; Benten, H.; Okada, I.; Ohkita, H.; Ito, S. *Advanced Energy Materials* **2014**, *4*, n/a-n/a.

(39) Tang, Y.; McNeill, C. R. *Journal of Polymer Science Part B: Polymer Physics* **2013**, *51*, 403-409.

(40) Zhou, N.; Lin, H.; Lou, S. J.; Yu, X.; Guo, P.; Manley, E. F.; Loser, S.; Hartnett, P.; Huang, H.; Wasielewski, M. R.; Chen, L. X.; Chang, R. P. H.; Facchetti, A.; Marks, T. J. *Advanced Energy Materials* **2014**, *4*, n/a-n/a.

(41) Kang, H.; Kim, K.-H.; Choi, J.; Lee, C.; Kim, B. J. *ACS Macro Letters* **2014**, *3*, 1009-1014.

(42) Mori, D.; Benten, H.; Okada, I.; Ohkita, H.; Ito, S. *Energy & Environmental Science* **2014**, *7*, 2939-2943.

(43) Mu, C.; Liu, P.; Ma, W.; Jiang, K.; Zhao, J.; Zhang, K.; Chen, Z.; Wei, Z.; Yi, Y.; Wang, J.; Yang, S.; Huang, F.; Facchetti, A.; Ade, H.; Yan, H. *Advanced Materials* **2014**, *26*, 7224-7230.

(44) Deshmukh, K. D.; Qin, T.; Gallaher, J. K.; Liu, A. C. Y.; Gann, E.; O'Donnell, K.; Thomsen, L.; Hodgkiss, J. M.; Watkins, S. E.; McNeill, C. R. *Energy & Environmental Science* **2015**, *8*, 332-342.

(45) Tang, Z.; Liu, B.; Melianas, A.; Bergqvist, J.; Tress, W.; Bao, Q.; Qian, D.; Inganas, O.; Zhang, F. *Advanced materials* **2015**, *27*, 1900-1907.

(46) Ye, L.; Jiao, X.; Zhou, M.; Zhang, S.; Yao, H.; Zhao, W.; Xia, A.; Ade, H.; Hou, J. *Advanced materials* **2015**, *27*, 6046-6054.

(47) Benten, H.; Nishida, T.; Mori, D.; Xu, H.; Ohkita, H.; Ito, S. *Energy Environ. Sci.* **2016**, *9*, 135-140.

(48) Zhou, N.; Dudnik, A. S.; Li, T. I.; Manley, E. F.; Aldrich, T. J.; Guo, P.; Liao, H. C.; Chen, Z.; Chen, L. X.; Chang, R. P.; Facchetti, A.; Olvera de la Cruz, M.; Marks, T. J. *Journal of the American Chemical Society* **2016**, *138*, 1240-1251.

(49) Kang, H.; Uddin, M. A.; Lee, C.; Kim, K. H.; Nguyen, T. L.; Lee, W.; Li, Y.; Wang, C.; Woo, H. Y.; Kim, B. J. *Journal of the American Chemical Society* **2015**, *137*, 2359-2365.

(50) Gao, L.; Zhang, Z. G.; Xue, L.; Min, J.; Zhang, J.; Wei, Z.; Li, Y. *Advanced materials* **2015**.

(51) Earmme, T.; Hwang, Y.-J.; Murari, N. M.; Subramaniyan, S.; Jenekhe, S. A. *Journal of the American Chemical Society* **2013**, *135*, 14960-14963.

(52) Earmme, T.; Hwang, Y.-J.; Subramaniyan, S.; Jenekhe, S. A. *Advanced Materials* **2014**, *26*, 6080-6085.

(53) Hwang, Y.-J.; Earmme, T.; Subramaniyan, S.; Jenekhe, S. A. *Chemical communications* **2014**, *50*, 10801-10804.

(54) Zhou, E.; Nakano, M.; Izawa, S.; Cong, J.; Osaka, I.; Takimiya, K.; Tajima, K. *ACS Macro Letters* **2014**, *3*, 872-875.

(55) Hendriks, K. H.; Heintges, G. H. L.; Gevaerts, V. S.; Wienk, M. M.; Janssen, R. A. J. *Angewandte Chemie International Edition* **2013**, *52*, 8341-8344.

(56) Li, W.; Roelofs, W. S. C.; Turbiez, M.; Wienk, M. M.; Janssen, R. A. J. *Advanced Materials* **2014**, *26*, 3304-3309.

(57) Verreet, B.; Cnops, K.; Cheyns, D.; Heremans, P.; Stesmans, A.; Zango, G.; Claessens, C. G.; Torres, T.; Rand, B. P. *Advanced Energy Materials* **2014**, *4*, n/a-n/a.

(58) Cnops, K.; Zango, G.; Genoe, J.; Heremans, P.; Martinez-Diaz, M. V.; Torres, T.; Cheyns, D. *Journal of the American Chemical Society* **2015**.

(59) Gong, X.; Tong, M.; Brunetti, F. G.; Seo, J.; Sun, Y.; Moses, D.; Wudl, F.; Heeger, A. J. *Advanced materials* **2011**, *23*, 2272-2277.

(60) Schwenn, P. E.; Gui, K.; Nardes, A. M.; Krueger, K. B.; Lee, K. H.; Mutkins, K.; Rubinstein-Dunlop, H.; Shaw, P. E.; Kopidakis, N.; Burn, P. L.; Meredith, P. *Advanced Energy Materials* **2011**, *1*, 73-81.

(61) Zhou, Y.; Ding, L.; Shi, K.; Dai, Y. Z.; Ai, N.; Wang, J.; Pei, J. *Advanced materials* **2012**, *24*, 957-961.

(62) Lu, R.-Q.; Zheng, Y.-Q.; Zhou, Y.-N.; Yan, X.-Y.; Lei, T.; Shi, K.; Zhou, Y.; Pei, J.; Zoppi, L.; Baldridge, K. K.; Siegel, J. S.; Cao, X.-Y. *J. Mater. Chem. A* **2014**, *2*, 20515-20519.

(63) Holliday, S.; Ashraf, R. S.; Nielsen, C. B.; Kirkus, M.; Rohr, J. A.; Tan, C. H.; Collado-Fregoso, E.; Knall, A. C.; Durrant, J. R.; Nelson, J.; McCulloch, I. *Journal of the American Chemical Society* **2015**, *137*, 898-904.

(64) Holliday, S.; Ashraf, R. S.; Wadsworth, A.; Baran, D.; Yousaf, S. A.; Nielsen, C. B.; Tan, C. H.; Dimitrov, S. D.; Shang, Z.; Gasparini, N.; Alamoudi, M.; Laquai, F.; Brabec, C. J.; Salleo, A.; Durrant, J. R.; McCulloch, I. *Nat Commun* **2016**, *7*, 11585.

(65) Kwon, O. K.; Park, J.-H.; Park, S. K.; Park, S. Y. *Advanced Energy Materials* **2015**, *5*, n/a-n/a.

(66) Kwon, O. K.; Uddin, M. A.; Park, J. H.; Park, S. K.; Nguyen, T. L.; Woo, H. Y.; Park, S. Y. *Advanced materials* **2015**.

(67) Kwon, O. K.; Park, J. H.; Kim, D. W.; Park, S. K.; Park, S. Y. *Advanced materials* **2015**, *27*, 1951-1956.

(68) Lin, Y.; Wang, J.; Zhang, Z. G.; Bai, H.; Li, Y.; Zhu, D.; Zhan, X. *Advanced materials* **2015**, *27*, 1170-1174.

(69) Bin, H.; Zhang, Z. G.; Gao, L.; Chen, S.; Zhong, L.; Xue, L.; Yang, C.; Li, Y. *Journal of the American Chemical Society* **2016**, *138*, 4657-4664.

(70) Zhao, W.; Qian, D.; Zhang, S.; Li, S.; Inganas, O.; Gao, F.; Hou, J. *Advanced materials* **2016**, *28*, 4734-4739.

(71) Li, H.; Kim, F. S.; Ren, G.; Hollenbeck, E. C.; Subramaniyan, S.; Jenekhe, S. A. *Angewandte Chemie* **2013**, *52*, 5513-5517.

(72) Li, H.; Earmme, T.; Ren, G.; Saeki, A.; Yoshikawa, S.; Murari, N. M.; Subramaniyan, S.; Crane, M. J.; Seki, S.; Jenekhe, S. A. *Journal of the American Chemical Society* **2014**, *136*, 14589-14597.

(73) Hwang, Y. J.; Li, H.; Courtright, B. A.; Subramaniyan, S.; Jenekhe, S. A. *Advanced materials* **2015**.

(74) Dittmer, J. J.; Marseglia, E. A.; Friend, R. H. *Angewandte Chemie* **2000**, *12*, 1270-1274.

(75) Keivanidis, P. E.; Howard, I. A.; Friend, R. H. *Advanced Functional Materials* **2008**, *18*, 3189-3202.

(76) Singh, R.; Aluicio-Sarduy, E.; Kan, Z.; Ye, T.; MacKenzie, R. C. I.; Keivanidis, P. E. *Journal of Materials Chemistry A* **2014**, *2*, 14348.

(77) Sharenko, A.; Gehrig, D.; Laquai, F.; Nguyen, T.-Q. *Chemistry of Materials* **2014**, *26*, 4109-4118.

(78) Rajaram, S.; Shivanna, R.; Kandappa, S. K.; Narayan, K. S. *The Journal of Physical Chemistry Letters* **2012**, *3*, 2405-2408.

(79) Shivanna, R.; Shoaee, S.; Dimitrov, S.; Kandappa, S. K.; Rajaram, S.;

Durrant, J. R.; Narayan, K. S. *Energy Environ. Sci.* **2014**, *7*, 435-441.

(80) Yan, Q.; Zhou, Y.; Zheng, Y.-Q.; Pei, J.; Zhao, D. *Chemical Science* **2013**, *4*, 4389.

(81) Zhang, X.; Lu, Z.; Ye, L.; Zhan, C.; Hou, J.; Zhang, S.; Jiang, B.; Zhao, Y.; Huang, J.; Zhang, S.; Liu, Y.; Shi, Q.; Liu, Y.; Yao, J. *Advanced materials* **2013**, *25*, 5791-5797.

(82) Zhao, J.; Li, Y.; Lin, H.; Liu, Y.; Jiang, K.; Mu, C.; Ma, T.; Lin Lai, J. Y.; Hu, H.; Yu, D.; Yan, H. *Energy Environ. Sci.* **2015**, *8*, 520-525.

(83) Zang, Y.; Li, C. Z.; Chueh, C. C.; Williams, S. T.; Jiang, W.; Wang, Z. H.; Yu, J. S.; Jen, A. K. *Advanced materials* **2014**, *26*, 5708-5714.

(84) Jiang, W.; Ye, L.; Li, X.; Xiao, C.; Tan, F.; Zhao, W.; Hou, J.; Wang, Z. *Chemical communications* **2014**, *50*, 1024-1026.

(85) Yu, J.; Xi, Y.; Chueh, C.-C.; Zhao, D.; Lin, F.; Pozzo, L. D.; Tang, W.; Jen, A. K. Y. *Advanced Materials Interfaces* **2016**, *3*, 1600476.

(86) Zhong, Y.; Trinh, M. T.; Chen, R.; Wang, W.; Khlyabich, P. P.; Kumar, B.; Xu, Q.; Nam, C. Y.; Sfeir, M. Y.; Black, C.; Steigerwald, M. L.; Loo, Y. L.; Xiao, S.; Ng, F.; Zhu, X. Y.; Nuckolls, C. *Journal of the American Chemical Society* **2014**, *136*, 15215-15221.

(87) Zhong, Y.; Trinh, M. T.; Chen, R.; Purdum, G. E.; Khlyabich, P. P.; Sezen, M.; Oh, S.; Zhu, H.; Fowler, B.; Zhang, B.; Wang, W.; Nam, C. Y.; Sfeir, M. Y.; Black, C. T.; Steigerwald, M. L.; Loo, Y. L.; Ng, F.; Zhu, X. Y.; Nuckolls, C. *Nat Commun* **2015**, *6*, 8242.

(88) Zhang, X.; Zhan, C.; Yao, J. *Chemistry of Materials* **2015**, *27*, 166-173.

(89) Liu, J.; Chen, S.; Qian, D.; Gautam, B.; Yang, G.; Zhao, J.; Bergqvist, J.; Zhang, F.; Ma, W.; Ade, H.; Inganäs, O.; Gundogdu, K.; Gao, F.; Yan, H. *Nature Energy* **2016**, *1*, 16089.

(90) Zhong, H.; Wu, C. H.; Li, C. Z.; Carpenter, J.; Chueh, C. C.; Chen, J. Y.; Ade, H.; Jen, A. K. *Advanced materials* **2015**.

(91) Hartnett, P. E.; Timalsina, A.; Matte, H. S.; Zhou, N.; Guo, X.; Zhao, W.; Facchetti, A.; Chang, R. P.; Hersam, M. C.; Wasielewski, M. R.; Marks, T. J. *Journal of the American Chemical Society* **2014**, *136*, 16345-16356.

(92) Lin, Y.; Wang, Y.; Wang, J.; Hou, J.; Li, Y.; Zhu, D.; Zhan, X. *Advanced materials* **2014**, *26*, 5137-5142.

(93) Liu, Y.; Lai, J. Y. L.; Chen, S.; Li, Y.; Jiang, K.; Zhao, J.; Li, Z.; Hu, H.; Ma, T.; Lin, H.; Liu, J.; Zhang, J.; Huang, F.; Yu, D.; Yan, H. *J. Mater. Chem. A* **2015**, *3*, 13632-13636.

(94) Liu, Y.; Mu, C.; Jiang, K.; Zhao, J.; Li, Y.; Zhang, L.; Li, Z.; Lai, J. Y.; Hu, H.; Ma, T.; Hu, R.; Yu, D.; Huang, X.; Tang, B. Z.; Yan, H. *Advanced materials* **2015**, *27*, 1015-1020.

(95) Lin, H.; Chen, S.; Hu, H.; Zhang, L.; Ma, T.; Lai, J. Y.; Li, Z.; Qin, A.; Huang, X.; Tang, B.; Yan, H. *Advanced materials* **2016**.

(96) Lee, J.; Singh, R.; Sin, D. H.; Kim, H. G.; Song, K. C.; Cho, K. *Advanced Materials* **2016**, *28*, 69-+.

(97) Yi, J.; Wang, Y.; Luo, Q.; Lin, Y.; Tan, H.; Wang, H.; Ma, C. Q. *Chemical communications* **2016**, *52*, 1649-1652.

(98) Li, S.; Liu, W.; Shi, M.; Mai, J.; Lau, T.-K.; Wan, J.; Lu, X.; Li, C.-Z.; Chen, H. *Energy Environ. Sci.* **2016**.

(99) Lin, Y.; Li, Y.; Zhan, X. *Advanced Energy Materials* **2013**, *3*, 724-728.

Chapter 2 Acceptor polymer based on thieno[2',3':4,5]pyrido[2,3-g]thieno[3,2-c]quinoline-4,10-dione

This chapter contains parts of the published work [Jung, I. H.; Zhao, D.; Jang J. *et al.* *Chem. Mater.* **2015**, 27, 5941–5948] Copyright (2015) American Chemical Society.

2.1 Background

Currently, research effort is shifting towards developing electron accepting polymers that can match and replace these fullerenes as electron acceptors. These efforts are important because the fullerenes are expensive compounds and exhibit limited absorption in longer wavelength region of the solar spectrum and thermal instability in the morphology of blend films, which potentially obstruct the commercialization of BHJ solar cells. Surely, a great challenge exists to develop accepting polymers that match or even surpass the property of fullerene because it is very difficult to mimic the spherical molecular structure of fullerenes. A relaxed design idea is to develop molecular acceptors with comparable energy levels as those of fullerenes. [1,2]

However, it was realized that energy level match along is not enough to achieve high efficiency in all-polymer solar cells.[3] Previously, our group reported alternating electron accepting polymers with the following monomer-comonomer combination: a) Weak donating monomer-strong accepting monomer (WD-SA), b) Weak accepting monomer-strong accepting monomer (WA-SA), c) Strong donating monomer-strong accepting monomer (SD-SA). Several criteria for designing electron accepting polymers for all-polymer solar cells are suggested.[3] It was found that accepting polymers prefer to exhibit proper energy levels, internal polarization and high charge carrier's mobility.

In this chapter, we have synthesized a new weak accepting monomer, 5,11-bis(2-butyloctyl)-dihydrothieno[2',3':4,5]pyrido[2,3-g]thieno[3,2-c]quinoline-4,10-dione (TPTQ), which is an isomer of previously synthesized cyclic diamide monomer (TPTI).[4,5] TPTQ also has highly planar structure, facilitating intermolecular ordering and the end thiophene structures enable further functionalization at the 2-position of the thiophenes to introduce distannanyl groups. The two electron withdrawing carbonyl moieties enhance the electron affinity of the conjugated system, resulting in a weak accepting monomer. For comparing the effect of polarity, we also developed difluorinated TPTQ (FTPTQ) exhibiting stronger electron accepting properties. These monomers allowed us to synthesize polymers with combination of strong accepting monomer-strong accepting monomer (SA-SA) and weak donating monomer-strong accepting monomer (WD-SA). The photovoltaic *J*-*V* characteristics were investigated in details and discussed in terms of molecular structure, charge carrier mobility and morphology of the blended film.

2.2 Results and discussion

2.2.1 Synthesis and Structural Characterization

Synthesis and structures of TPTQ and FTPTQ are shown in Figure 2.1. TPTQ monomer was synthesized according to a similar approach with the TPTI monomer.[3] FTPTQ was synthesized via a similar route with TPTI and TPTQ, starting from difluoro dibromo benzene. Synthesis of PIP can be found in our pervious publication.[6] Synthesis scheme is shown as follows.

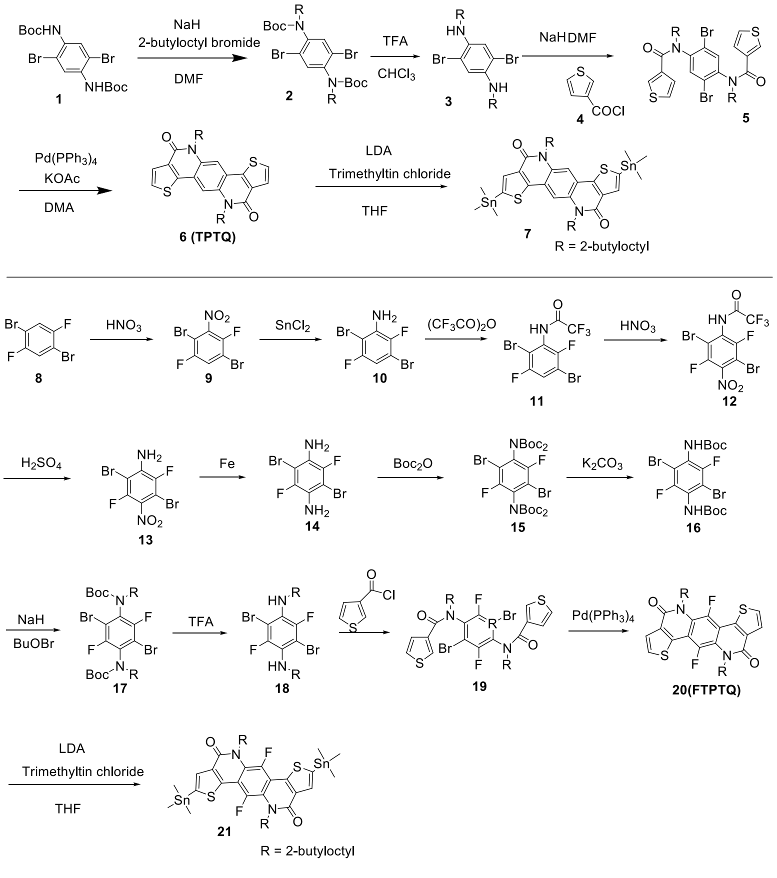

Figure 2.1 Structures and Synthesis route of TPTQ and FTPTQ.

To develop electron accepting polymers, the perylene diimide (PDI) was used as a co-monomer. The accepting polymers, **PQP**, **PFP** and **PIP**, were synthesized through the Stille polycondensation of monomer PDI with stannylated TPTQ, FTPTQ and TPTI, respectively (Figure 2.2). All of these polymers contain WA-SA monomer repeating units. The number average molecular weights (M_n) of the resulting polymers were determined by gel permeation chromatography (GPC) using polystyrene as standard to be 21,600 g/mol (PDI = 2.83) for **PQP**, 12307g/mol (PDI = 2.74) for **PFP** and 18,100 g/mol (PDI = 2.17) for **PIP**. All of the polymers showed excellent solubility in common organic solvents (i.e., THF, hexane, dichloromethane, chloroform, chlorobenzene, dichlorobenzene). The thermal stability of the polymers was evaluated by TGA under N_2 atmosphere. **PQP**, **PFP** and **PIP** exhibited good stability, showing less than 5% weight loss up to 379, 358, and 387 °C, respectively. The physical properties of the polymers are summarized in Table 2-1.

Table 2-1 Physical properties of the polymers PIP, PQP and PFP

	M_n [(a)]	M_w [(b)]	PDI	T_d [(c)]	θ (°) [(d)]	μ (D) [(e)]
PQP	21,600	61,000	2.83	379	57.99	1.73
PFP	12,307	33,880	2.74	358	59.59	0.99
PIP	18,100	39,300	2.17	387	60.27	1.58

(a) Number average molecular weight, (b) Weight average molecular weight, (c) Decomposition temperature determined by TGA under N_2 based on a 5% weight loss. (d) Dihedral angle between the two donor/acceptor units in the polymer backbones and (e dipole moment of the oligomers with three repeating units calculated from the DFT methods using the GAUSSIAN.

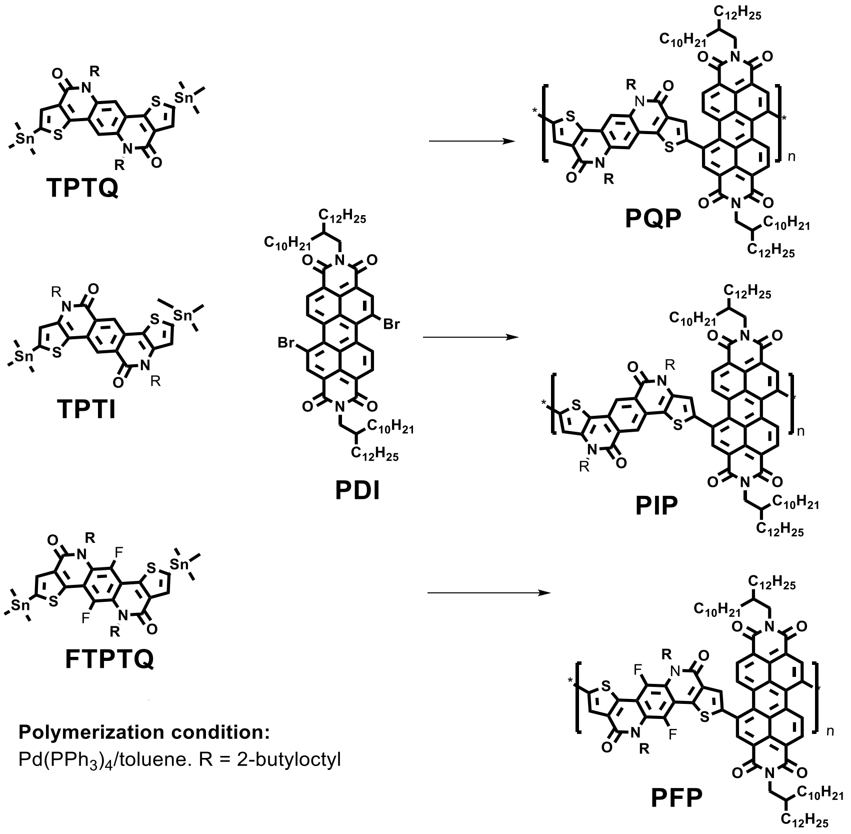

Figure 2.2 Synthetic scheme for the electron accepting polymers

2.2.2 Optical properties

The absorption spectra of the polymers were recorded in chloroform (CF) or in films, and are shown in Figure 2.3. The absorption maxima for **PIP** were observed at 409, 504 and 618 nm in chloroform; and 413, 509 and 652 nm in the film state. **PQP** exhibited absorption maxima at 427 and 494 nm in chloroform, and 432 and 505 nm in the film state. **PFP** showed 2 major absorption peaks at 407 and 502 nm in CF solution and 410 and 525 nm in film state. The absorption bandwidths of the polymer films are broader and their absorption onsets are red-shifted comparing to those in solution because of the stronger intermolecular interactions between neighboring molecules in the film state. Significant differences can be observed among the polymers, **PIP**, **PQP** and **PFP**, caused by a small structural variation. This is likely due to the difference in electronic effect on conjugated backbones. In **PIP**, the amide nitrogen is directly connected to thiophene rings that make them more electron rich due to the donating properties of lone pair electron on nitrogen atoms. That will enhance the HOMO energy level more than when they are connected with central benzene ring.

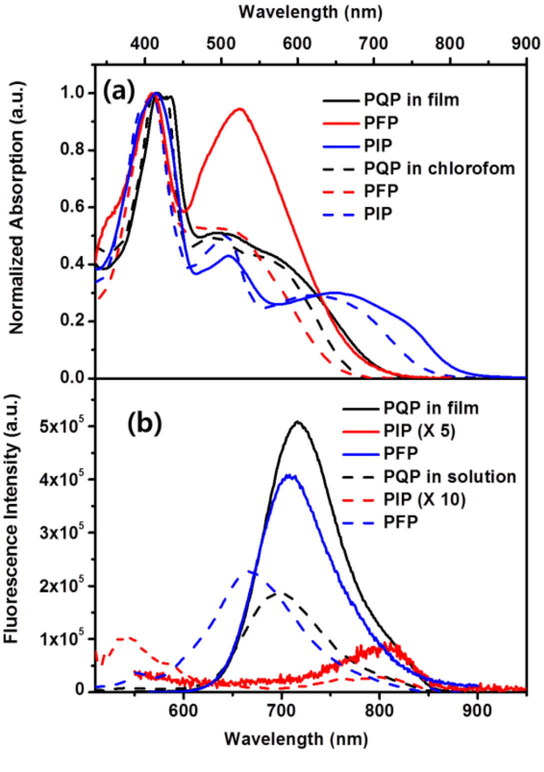

Figure 2.3 a) UV-vis absorption spectra of the copolymers and (b) fluorescence spectra of the polymers excited at 507 nm for PIP and 509 nm for PQP and PFP in CF solution after the absorption intensity in chloroform solution was adjusted as 0.04, and in film after spin-coating from chloroform solution (1.0 w%) by 1500 rpm.

To understand the optical properties, the ground-state (S0) geometric structures of the oligomers with three repeating units were calculated with density functional theory (DFT) using the B3LYP functional and a 3-21G basis set[7-9]. The calculated structures of the compounds are shown in Figure 2.4, which show that all of the polymer structures are fairly twisted. The dihedral angles at the junction of two monomers in the polymer backbones are almost 60 °. However, three polymers showed quite different electron distribution in the HOMOs. The electron distribution of **PIP** is completely localized within the TPTI monomer in the HOMO. Therefore, the HOMO energy level of the **PIP** polymer almost resembles that of TPTI monomer. On the other hand, the electron density of **PFP** in HOMO is delocalized along the polymer backbone through both PDI and FTPTQ monomers. In case of **PQP**, the HOMO involves those mostly from the TPTQ monomer and a small amount of PDI monomer. Therefore, HOMO energy level of **PQP** resembles that of TPTQ, but slightly decreased due to the PDI unit. In case of LUMO orbitals, all of the polymers show almost identical orbital distribution only localized at PDI unit. Therefore, three polymers showed same LUMO level of -4.0 eV just like that of PDI. As a result, the difference in the bandgap of polymers is mainly determined by HOMO energy levels of polymers.

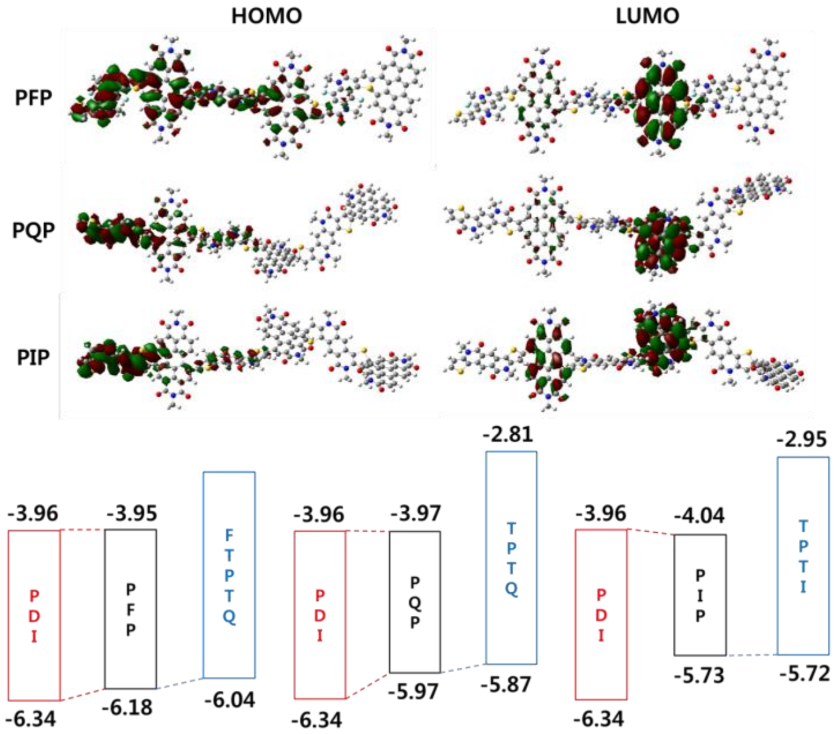

Figure 2.4 HOMO and LUMO diagrams of the monomers and polymers, calculated with DFT method.

The fluorescence spectra and the emission quantum yield (QY) of the polymers were measured in a diluted solution and are shown in Figure 2.3(b). The solution used for these measurements exhibit the intensity at the absorption maxima at 0.04 to prevent the aggregation effect. Fluorescein was used as a reference fluorescence dye, whose QY in ethanol is known to be 0.79.[10] All of the polymers exhibited minimal fluorescent emission, but **PIP** containing TPTI derivatives exhibited lowest QY of 0.06%. Previouly, we suggested that the effective internal polarization between the two monomers reduces the fluorescent quantum yield of the polymers.[3] The repeating unit of strong electron accepting PDI and weak electron accepting TPTI exhibits strong internal polarization, leading to small quantum efficiency in emission of **PIP**. This is the same as for **PQP** and **PFP**. However, a small increase in quantum efficiency from **PQP** to **PFP** is noticeable which may reflect the decrease in internal polarization although it must be cautious not to over emphasize this point.

2.2.3 Electrochemical properties

The electrochemical properties of the synthesized monomers and polymers were investigated by using cyclic voltammetry (CV) and the related cyclic voltammograms are shown in Figure 2.5. The HOMO and the LUMO energy levels of the monomers and polymers were calculated from the oxidation and reduction onset potentials relative to ferrocene (as an internal standard) and are summarized in Figure 2.6.[11,12] The oxidation and the reduction potentials of PQP were determined to be 1.26 eV and –0.74 eV, respectively, which corresponded to the HOMO and the LUMO energy levels of –5.97 eV and –3.97 eV, respectively. After introducing two fluorine atoms, the HOMO energy level of PFP was significantly decreased to -6.18 eV while the LUMO energy levels was almost not affected (-3.95 eV), which also coincide with DFT calculation.

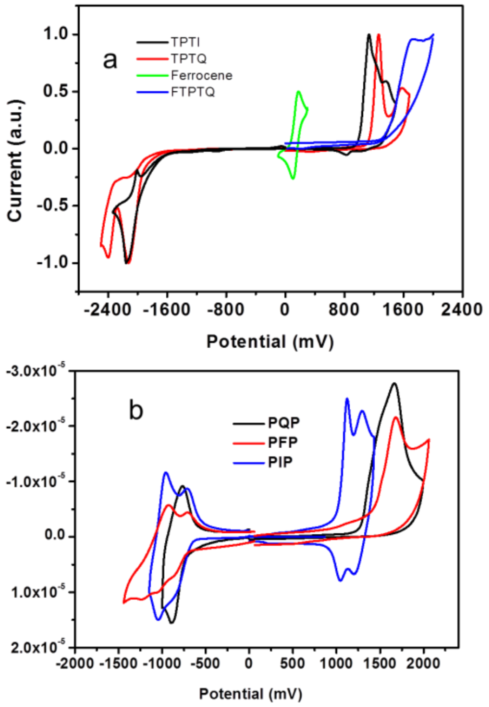

Figure 2.5 Cyclic voltammograms of the electron accepting (a) monomers and (b) polymers.

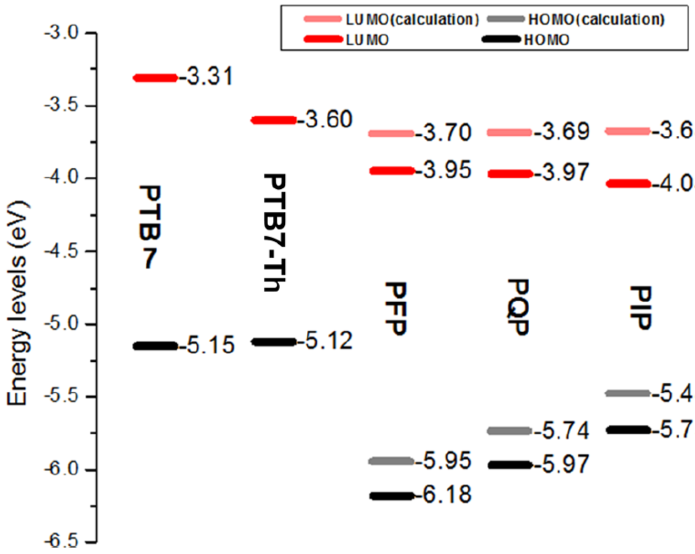

Figure 2.6 Electrochemical bandgap diagram of the synthesized electron accepting polymers.

2.2.4 Photovoltaic effect

Based on the energy level values, these polymers are suitable to serve as electron acceptors in couple with many electron donating polymers. The PV properties of the polymers were examined based on bulk heterojunction solar cells with the following configuration: ITO/PEDOT:PSS/polymer blends/Ca/Al. The current-voltage (*J*-*V*) characteristics of the devices (under AM 1.5G condition, 100 W/cm^2) of the donor polymers: accepter polymers mixtures are shown Figure 2.7(a) and (b), and the corresponding PV parameters are summarized in Table 2-2.

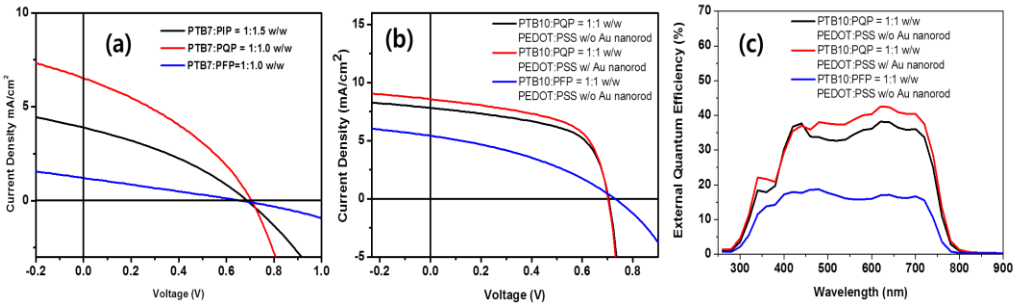

Figure 2.7 *J*–*V* characteristics of BHJ photovoltaic devices with an active layer composed of (a) PTB7:accepting polymers and (b) PTB7-Th: accepting polymers, and (c) EQE of BHJ photovoltaic devices with an active layer composed of PTB7-Th:accepting polymers, under simulated AM 1.5 G solar irradiation.

Table 2-2 Summary of photovoltaic properties.

Active layer	Solvent	J_{sc} (mA/cm^2)	V_{oc} (V)	Fill factor	PCE$_{max}$ (PCE$_{average}$) [%]
PTB7:**PIP**	CF:DIO (3% v/v)	-4.13	0.69	0.34	0.97 (0.96)
PTB7:**PFP**	CF:DIO (3% v/v)	-1.21	0.66	0.26	0.21(0.18)
PTB7:**PQP**	CF:DIO (3% v/v)	-5.92	0.69	0.34	1.43 (1.41)
PTB7:**PQP**	CF:CN (6% v/v)	-6.51	0.69	0.36	1.62 (1.58)
PTB7:**PQP** with Au rod	CF:CN (6% v/v)	-7.20	0.69	0.37	1.86 (1.81)
PTB7-Th :**PFP**	CF:CN (6% v/v)	-5.16	0.70	0.39	1.43 (1.33)
PTB7-Th :**PQP**	CF:CN (6% v/v)	-7.80	0.71	0.58	3.22 (3.11)
PTB7-Th :**PQP** with Au rod	CF:CN (6% v/v)	-8.57	0.71	0.58	3.52 (3.38)

These polymers exhibited energy levels that are suited as electron accepting polymers. The initial devices fabricated by spin-coating the solutions of Poly[[4,8-bis[(2-ethylhexyl)oxy]benzo[1,2-b:4,5-b']dithiophene-2,6-diyl][3-fluoro-2-[(2-ethylhexyl)carbonyl]thieno[3,4-b]thiophenediyl]] (**PTB7**)/ **PQP** or **PFP** in CF (1:1 w/w) exhibited PCE of 0.76, and 0.03 %, respectively. It was found that the performance of **PTB7**/**PQP** blends is very sensitive to the kinds of additives. **PTB7**/**PQP** device exhibited higher PCE value of 1.43 % (V_{oc} = 0.69 V, J_{sc} = 5.92 mA/cm^2, FF = 0.34) at a weight ratio of **PTB7**/**PQP** = 1:1 when 3% v/v of 1,8-diiodooctane (DIO) was mixed with chloroform, which was further increased to 1.62 % (V_{oc} = 0.69 V, J_{sc} = 6.51 mA/cm2, FF = 0.36) when 6% of CN as mixed with chloroform. Atomic force microscopy (AFM) studies indicated that the **PTB7**/**PQP** blend films prepared from pure chloroform solution showed rather uniform morphology with a root-mean-square (rms) roughness of 0.72 nm as shown in Figure 2.8(d). The films also exhibited a minimal face-on ordering as shown in the grazing incidence wide angle x-ray scattering (GIWAXS) pattern (Figure 2.8 (a)). These results indicate relatively homogeneous topography and good miscibility, which is not favorable for effective charge dissociation and transport. When DIO was used as additive co-solvent, the roughness of blend film was increased to 1.44 nm (Figure 2.8 (e)) and GIWAXS pattern (Figure 2.7 (b)) indicated a clearer face-on ordering with a d-spacing of ~4.0 Å. When 1-chloronaphthalene was used, much rougher surface with an average roughness of 2.20 nm was observed (Figure 2.8(f)) and face-on orientation of blended films was further enhanced (Figure 2.8(c)). Since 1-CN has a higher boiling point (263 °C), a slower evaporation rate seems to allow favorable phase separation between electron donor and acceptor and to form molecular ordering suitable for vertical electron transport pathway.[13]

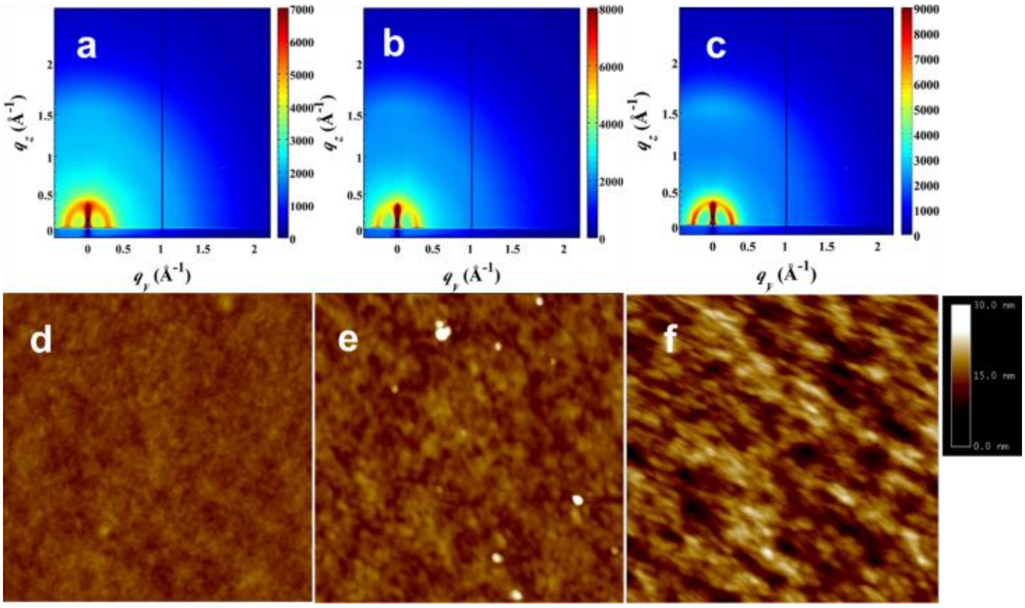

Figure 2.8 2D GIWAXS patterns of PTB7:PQP (1:1 w/w) film from (a) CF, (b) CF:DIO (3% v/v) and (c) CF:CN (6% v/v) and AFM topographic images of PTB7:PQP (1:1 w/w) film from (d) CF, (e) CF:DIO (3% v/v) and (f) CF:CN (6% v/v).

It was also found that the photovoltaic performance of **PQP** device could be further enhanced when a different donor polymer with better LUMO alignment was used. When we introduced Poly[4,8-bis(5-(2-ethylhexyl)thiophen-2-yl) benzo[1,2-b;4,5-b']dithiophene-2,6-diyl-alt-(4-(2-ethylhexyl)-3-fluorothieno[3,4-b]thiophene-)-2-carboxylate-2-6-diyl)] (**PTB7-Th**) polymer developed in our lab,[14] as an electron donating polymer, which is a **PTB7** derivative containing 2-alkylthienyl groups instead of alkoxy side chain, devices made from the **PTB7-Th**:**PQP** blend (weight ratio 1:1), prepared from chloroform solution with 6% of 1-chloronaphthalene as an additive, exhibited an enhanced PCE value of 3.22 % (V_{oc} = 0.71 V, J_{sc} = 7.80 mA/cm^2, FF =

0.58). As shown in Figure 2.6, the LUMO energy level of **PTB7-Th** is closer to that of **PQP**, showing better energy matching between donor and acceptor with a difference around 0.37 eV. This can facilitate charge transfer from donor to acceptor, resulting in higher current density and fill factor. When fluorinated **PFP** polymer was blended with **PTB7-Th**, similar solvent effect was observed. The device performance was enhanced form the PCE of 0.19 % made from chloroform solution to 1.43% with polymer blends (1:1 w/w) spin-coated from CF with 6% of CN. The device showed almost identical V_{oc} values, but the J_{sc} value is smaller than **PQP** system, indicating charge generation is not as efficient as that with **PQP** system. Since the only difference between **PFP** and **PQP** is two fluorine atoms in the weak accepting monomer units, all of the optical properties are quite similar. The two fluorine atoms in **PFP** reduced the internal polarization of the **PFP** polymers, which made the charge separation less favorable. The net electronic effect is similar to what we observed in our PTB series of donor polymers.[15] This result echoes the fluorescent measurement results.

To gain more insight into the structure-property correlation, the carrier mobility of the **PTB7-Th**:electron accepting polymers was measured by using sandwich-type devices and the steady-state space-charge limited current (SCLC) technique.[16] The hole mobilities (μ_{Hole}) of polymer blend films were evaluated in vertical hole-only devices with structures of ITO/PEDOT:PSS/**PTB7-Th**:electron accepting polymers (1:1 w/w, 2.5 vol% 1-CN) (blend state)/Au, and the electron mobilities ($\mu_{Electron}$) are measured with structures of ITO/ZnO/**PTB7-Th**:electron accepting polymers (1:1 w/w, 2.5 vol% 1-CN) (blend state)/LiF/Al. It was found that the hole mobilities of **PTB7-Th**:**PQP** and **PTB7-Th**:**PIP** films exhibited similar values as 1.12×10^{-4} and 1.34×10^{-4} cm^2/Vs, respectively. The **PTB7-Th**:**PFP** polymer blends exhibited a much higher hole mobility of 8.35×10^{-4} cm^2/Vs. In contrast, the electron mobility of PTB10:**PQP** films was highest as 1.75×10^{-7} cm^2/Vs. As a result, **PTB7-Th**/**PQP** devices showed more balanced electron/hole mobility than **PTB7-Th**/**PFP** devices. The better hole/electron balance in the devices contributes to the higher J_{SC} and FF values in photovoltaic devices because the extent of recombination processes can be minimized.[17]

GIWAXS studies (**Figure 2.9**) showed that neat **PFP** and **PQP** films are amorphous and show no obvious diffraction feature. The blended film spin cast from CF/CN solution of **PTB7-Th**/**PQP** exhibited much stronger face-on orientation than **PTB7-Th**/**PFP** film. An average interval of (*h*00) reflections along the Q_r axis of 0.27 $Å^{-1}$ was observed, corresponding to the layer spacing of 23.06 Å for (100) crystal, $d_{(100)}$. An intermolecular π-stacking distance of 3.93 Å can be assigned to the layer spacing of the (010) crystal planes, $d_{(010)}$. The better face-on ordering of **PTB7-Th**/**PQP** films facilitated the vertical electron transport pathway, resulting in higher J_{sc} characteristic on **PTB7-Th/PQP** devices. It can also be noted that **PTB7-Th/PQP** films exhibited stronger face-on ordering than **PTB7/PQP** films as shown in **Figure 2.9** (e) and (f). Thus, all of these factors lead to highest PCE of 3.22 % for **PTB7-Th/PQP** system.

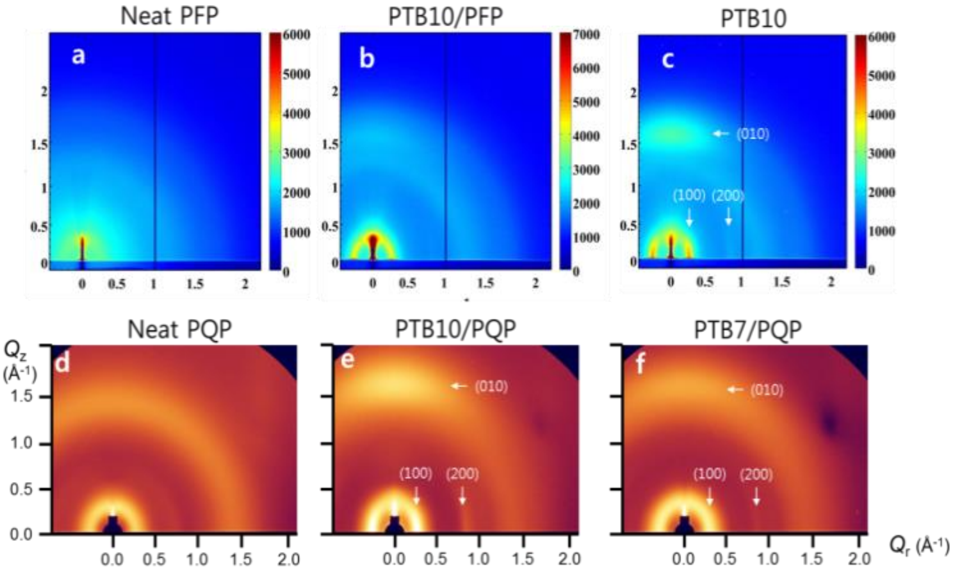

Figure 2.9 D GIWAXS patterns of (a) the neat PFP polymer, (b) PTB7-Th:PFP (1:1 w/w, CF:CN 6% v/v) blends, (c) the neat PTB7-Th polymer, (d) the neat PQP polymer and (e) PTB7-Th:PQP (1:1 w/w, CF:CN 6% v/v) blends (f) PTB7:PQP (1:1 w/w, CF:CN 6% v/v) blends.

Further enhancement of all-polymer cells can be achieved by introducing plasmonic effect, as shown in our previous work.[18] It was found that the addition of Au nanorods into the PEDOT:PSS layer in **PTB7-Th/PQP** solar cells increased the J_{sc} value to 8.57 mA/cm^2, and further pushed the PCE value to 3.52 % (V_{oc} = 0.71 V, J_{sc} = 8.57 mA/cm^2, FF = 0.58). The $J-V$ curves of **PTB7-Th/PQP** devices with and without

Au nanorods are shown in Figure 2.7(b) and their photovoltaic parameters are summarized in Table 2-2. Figure 2.7(c) showed the EQE of **PTB7-Th/PQP** device with Au nanorods increased due to the intensified absorption within visible region, resulting in 9.8% enhancement of J_{sc} in the devices.

2.2.5 Experimental section

1, Synthesis

Compound **2**: Sodium hydride (1.2 g, 30.0 mmol, 60 % dispersion in mineral oil) was suspended in dry DMF (30 ml). Compound **1** (4.66 g, 10.0 mmol) dissolved in DMF (50 ml) was added dropwise to the suspension of sodium hydride at 0ºC. After 30 min, 2-butyloctyl bromide (7.5 g, 30.0 mmol) was slowly added to the mixture and the mixture was stirred at room temperature overnight. The mixture was poured into water (100 mL) and extracted with dichloromethane. The organic layer was washed three times with water and dried over magnesium sulfate. After removal of the solvent under reduced pressure, the residue was purified by column chromatography on silica gel (hexane: ethyl acetate = 30: 1 v/v) and dried under vacuum to give product (6.2 g, 78%). ^{1}H-NMR (400 MHz, $CDCl_3$): δ (ppm) 7.40 (s, 2H), 3.65 (s, 2H), 3.22 (s, 2H), 1.72 (m, 2H), 1.33 (s, 18H), 1.26 (m, 32H), 0.88 (m, 12H). ^{13}C-NMR (100 MHz, $CDCl_3$): δ (ppm)

154.35, 149.03, 131.04, 128.95, 84.1, 53.42, 36.93, 31.95, 29.88, 28.57, 28.18, 26.33, 24.83, 23.23, 22.84, 14.25, 14.21. MS (MALDI-TOF) *m/z* 802.52 (M+), calcd 802.80.

Compound **5**: Compound **2** (5.6 g, 7.0 mmol) was dissolved in a mixture of $CHCl_3$ and TFA (30 ml, 1:2 v/v) and stirred at room temperature overnight. After extraction with dichloromethane, the organic layer was washed three times with water and dried over magnesium sulfate. After removal of the solvent under reduced pressure, the compound **3** was used directly for next step. A solution of thiophene-3-carboxylic acid (2.3 g, 17.9 mmol) in thionyl chloride (20 ml) was refluxed for 6 hours. The solvent was removed by reduced pressure to yield an acid chloride compound **4** as a yellow solid. After the acid chloride **4** was dissolved in dry DMF (20 mL), it was slowly added dropwise into a mixture of compound **3** and NaH (0.72 g, 17.9 mmol, 60 % dispersion in mineral oil) in dry DMF (30 mL) at 0 °C. The mixture was stirred at room temperature for 24 hours and poured into water (50 ml). The mixture was extracted with dichloromethane and washed three times with water. After drying over magnesium sulfate, the residue was purified by column chromatography on silica gel (hexane: ethyl acetate = 15: 1 v/v) and dried under vacuum to give product (2.9 g, 51 %). ^{1}H-NMR (400 MHz, $CDCl_3$): δ (ppm) 7.44 (d, 2H, J = 2.8 Hz), 7.13 (s, 2H), 7.04 (s&d, 4H), 4.09 (m, 2H), 3.37 (m, 2H), 1.56 (m, 2H), 1.23 (m, 32H), 0.86 (m, 12H). MS (MALDI-TOF) *m*/*z* 822.21 (M+), calcd 822.84

Compound **12**: compound **12** was synthesized by a similar method with compound **5**. Compound **10** was synthesized by the Boc deprotection of compound **9** (5.6 g, 7.0 mmol) and thiophene-3-carbonyl chloride was synthesized from thiophene-3-carboxylic acid (2.3 g, 17.9 mmol). To a solution of NaH (0.72 g, 17.9 mmol) and compound **10** was added thiophene-3-carbonyl chloride. The crude product was purified by column chromatography on silica gel (hexane: ethyl acetate = 15: 1 v/v) to give a white solid (2.9 g, 51 %). ^{1}H-NMR (400 MHz, $CDCl_3$): δ (ppm) 7.44 (d, 2H, J = 2.8 Hz), 7.13 (s, 2H), 7.04 (s&d, 4H), 4.09 (m, 2H), 3.37 (m, 2H), 1.56 (m, 2H), 1.23 (m, 32H), 0.86 (m, 12H). ^{13}C-NMR (100 MHz, $CDCl_3$): δ (ppm) 164.83, 142.96, 136.59, 135.42, 128.54, 127.93, 125.02, 122.77, 53.11, 36.50, 31.90, 31.26, 30.94 29.70. 28.56, 26.38, 23.02, 23.00, 14.25. MS (MALDI-TOF) *m*/*z* 822.21 (M+), calcd 822.84

Compound **6**: A solution of compound **5** (2.0 g, 2.4 mmol), $Pd(PPh_3)_4$ (115 mg, 0.1 mmol), and AcOK (70 mg, 7.2 mmol) in anhydrous DMA (150 mL) was degased for 30 min using nitrogen gas and then stirred at 120 °C for 4 h. The mixture was extracted with dichloromethane and dried over magnesium sulfate. After solvent was evaporated under reduced pressure, the residue was chromatographed on a silica gel column with hexane/ethyl acetate (15:1 v/v) as eluent and recrystallized from dichloromethane/methanol to give a yellow product **6** (1.3g, 80%).

^{1}H-NMR (400 MHz, $CDCl_3$): δ (ppm) 7.76 (d, 2H, J = 5.2 Hz), 7.74 (s, 2H), 7.43 (d, 2H, J = 5.6 Hz), 4.40 (br, 4H), 2.02 (m, 2H), 1.24-1.34 (m, 32H), 0.82-0.91 (m, 12H). ^{13}C-NMR (100 MHz, $CDCl_3$): δ (ppm) 158.81, 144.41, 132.31, 131.91, 127.52, 125.65, 119.43, 110.27, 46.16, 37.06, 31.96, 31.71, 29.89, 29.39, 27.17, 23.31, 22.77, 14.28, 14.22. MS (MALDI-TOF) *m/z* 661.41 (M+), calcd 661.01.

Compound **7**: LDA was prepared by adding *n*-BuLi (1.5 mL, 3.75 mmol, 2.5 M in hexanes) to a solution of diisopropylamine (0.40 g, 3.95 mmol) in 10 mL of THF, at –78 °C. The solution was stirred 30 min at 0 °C and then cooled again to –78 °C. The LDA was added dropwise to a solution of compound **6** (1.0 g, 1.51 mmol) in THF (250 mL) at -78 °C. The mixture was stirred at -78 °C for 2 hours and then 7.5 ml of trimethyltin chloride (1 M in hexanes) was added dropwise. The reaction was allowed to warm to room temperature and stirred for 16 hours. The mixture was poured into water (200 mL) and extracted with diethyl ether. The organic layer was washed three times with water and dried over magnesium sulfate. After drying solvent, the residue was purified by recrystallization from isopropyl alcohol to give a yellow product 7 (1.0 g, 67%).

^{1}H-NMR (400 MHz, $CDCl_3$): δ (ppm) 7.85 (s, 2H), 7.81 (s, 2H), 4.42 (br, 4H), 2.02 (m, 2H), 1.27-1.54 (m, 32H), 0.90 (m, 12H), 0.46 (s, 18H). ^{13}C-NMR (100 MHz, $CDCl_3$): δ (ppm) 159.23, 149.51, 140.20, 135.44, 132.83, 131.98, 119.39, 110.71, 46.06, 37.18, 32.14, 32.07, 31.87, 29.95, 29.65, 27.39, 23.38, 22.80, 14.40, 14.24, -8.00. MS (MALDI-TOF) *m/z* 986.30 (M+), calcd 986.63.

4-dibromo-2,5-difluoro-3-nitrobenzene (9): To a solution of 1,4-dibromo-2,5-difluorobenzene **8** (50g,184mmol) in 100ml conc. H_2SO_4, fuming nitric acid (19ml) was added drop wise through addition funnel. The mixture was stirred overnight. After the reaction is done, the mixture was poured onto ice, extracted with ethyl acetate. After evaporation of solvent, the brown oil (39.33g, 67%) was carried on to next step without purification. ^{1}H-NMR (400 MHz, $CDCl_3$): δ (ppm) 7.55 (1H, m). m/z=316.88 found 317.07.

2,5-dibromo-3,6-difluoroaniline(10): 1,4-dibromo-2,5-difluoro-3-nitrobenzene **9** (83g, 260mmol) and $SnCl_2$ (200g,1050mmol) were stirred in 1740ml ethanol and 440ml conc. hydrochloric acid. The mixture was heated at 85°C overnight. After removal of ethanol by evaporation, mixture was neutralized by sat. potassium carbonate solution, and then extracted by ethyl acetate. Organic layer was washed by water. Compound **10** (48g, 64%) was carried on to next step without purification. ^{1}H-NMR (400 MHz, CDCl$_3$): δ (ppm) 6.72 (dd, 1H), 4.93 (s, 2H). m/z=286.90, found 287.15.

N-(2,5-dibromo-3,6-difluorophenyl)-2,2,2-trifluoroacetamide (11): 2,5-dibromo-3,6-difluoroaniline **10** (30g, 104mmol) was dissolved in 1.5L chloroform, then 90mL trifluoroacetic anhydride was added drop wise at room temperature. The reaction was stirred at room temperature overnight, naturalized with saturated NaHCO$_3$ solution, extracted with dichloromethane. The organic layer was washed water twice. After removal of solvent, the brown solid was further purified by column chromatography with hexane/dichloromethane=3/2. Compound 4 was obtained as white solid (22g, 55%). ^{1}H-NMR (400 MHz, CDCl$_3$): δ (ppm) 7.87 (s, 1H), 7.44 (m, 1H). m/z=382.91, found 383.90.

N-(2,5-dibromo-3,6-difluoro-4-nitrophenyl)-2,2,2-trifluoroacetamide (12): Compound **11** was prepared with similar condition of compound **9**. The crude product was further purified by column chromatography (hexane/dichloromethane=3/1). Pure **12** was obtained as white solid (36%). ^{1}H-NMR (400 MHz, CDCl$_3$): δ (ppm) 8.21 (s, 1H).

^{13}C-NMR (100 MHz, $CDCl_3$): δ (ppm) 155.2, 154.8, 152.9, 150.4, 149.4, 146.8, 125.2, 125.0, 116.7, 113.8, 110.5, 110.3, 103.3, 103.1. m/z=427.91, found 429.99.

2,5-dibromo-3,6-difluoro-4-nitroaniline (13): To 0.21g (0.5mmol) of compound **12**, 5ml water and 1.5ml conc. H_2SO_4 was added. The reaction was heated to reflux for 3 h. After cooled down to room temperature, aqueous KOH solution then K_2CO_3 solution was added to adjust pH to 8. The mixture was then extracted with ethyl acetate. Organic layer was washed with water. Crude **13** (0.16g, 98%) was obtained as yellow oil after evaporation of solvent. ^{1}H-NMR (400 MHz, DMSO): δ (ppm) 3.66 (2H, s), ^{13}C-NMR (100 MHz, DMSO): δ (ppm) 152.4, 149.9, 145.0, 142.6, 141.8, 141.6, 128.2, 103.5, 103.2, 95.0, 94.8. m/z=331.90, found 332.80.

2,5-dibromo-3,6-difluorobenzene-1,4-diamine (14): Compound **14** was prepared with similar condition of compound **10**. Crude product was further purified by recrystallization from hexane. **14** was obtained as white, needle like crystal (yield: 62%). ^{1}H-NMR (400 MHz, DMSO): δ (ppm) 3.64 (s, 4H). ^{13}C-NMR (100 MHz, DMSO): δ (ppm) 146.4, 144.1, 126.7, 126.5, 98.0, 97.7. m/z=301.91 found 302.69.

2,5-dibromo-3,6-difluoro-N,N,N',N'-tetra-(*tert*-butoxycarbonyl)-p-phenylenediamine (15): Compound **14** (130mg, 0.43mmol), Boc_2O (563mg, 2.58mmol) and DMAP

(1.5mg, 3%mol) was dissolved in 3ml THF. The mixture was reflexed for 2.5 h then cooled back to rt. After rotovapting the solvent, solid mixture was purified by column chromatography (hexane/ethyl acetate=6/1) to yield **15** (162mg, 53%) as a white solid. ^{1}H-NMR (400 MHz, $CDCl_3$): δ (ppm) 1.38 (s, 18H). ^{13}C-NMR (100 MHz, $CDCl_3$): δ (ppm) 153.1, 151.1, 148.6, 128.5, 110.5, 84.2, 27.8. m/z=702, found 725.1 (+Na^+).

2,5-dibromo-3,6-difluoro- N,N'-di-(*tert*-butoxycarbonyl)-p-phenylenediamine (16): A suspension of **15** (5.1g, 7.26mmol) and K_2CO_3 (6g, 43.6mmol) in methanol was refluxed overnight. After cooled to room temperature, the mixture was extracted with dichloromethane. Organic layer was washed by water, dried over sodium sulfate. After removing the solvent, the crude solid was recrystallized from hexane. Pure product obtained as white powder (3.15g, 86%). ^{1}H-NMR (400 MHz, $CDCl_3$): δ (ppm) 9.23 (s, 2H), 1.47 (s, 18H). ^{13}C-NMR (100 MHz, $CDCl_3$): δ (ppm) 153.5, 153.3, 151.6, 125.5, 111.1, 80.5, 28.5. m/z=638.55, found 638.84.

2,5-dibromo-3,6-difluoro-N,N'-dibutyloctyl-N,N'-di-(*tert*-butoxycarbonyl)-p-phenylenediamine (17): A suspension of sodium hydride (0.96g, 60%, 24mmol) in anhydrous DMF 200ml was cooled to 0ºC. Compound **16** (3.0g, 6mmol) suspended in another 20ml DMF was added drop wise to sodium hydride suspension at 0ºC. After addition, the suspension was warmed up to room temperature and stirred for 1 hour. The suspension was then cooled to 0ºC again, butyloctyl bromide was added dropwise. After addition, the reaction was left to warm back to room temperature, and stirred overnight. After reaction is done, the mixture is cooled to 0ºC, water was added slowly to quench excess sodium hydride. The mixture was extracted by dichloromethane. The organic layer was washed with water, then dried over sodium sulfate. After removing the solvent, the crude product was purified by column chromatography (hexane/ethyl acetate=24/1) to yield **17** as a colorless oil (4.0g, 80%). ^{1}H-NMR (400 MHz, $CDCl_3$): δ (ppm) 3.32-3.62 (m, 4H) 1.25-1.59 (m, 52H) 0.84-0.87 (m, 12H). ^{13}C-NMR (100 MHz, $CDCl_3$): δ (ppm) 154.32, 153.42, 151.85, 130.49, 111.12, 80.96, 52.42, 52.17, 37.68, 37.53, 31.73, 31.43, 31.29, 31.07, 30.94, 29.66, 29.62, 28.72, 28.48, 27.86, 27.83, 26.53, 26.26, 26.23, 23.01, 22.98, 22.63, 14.06, 14.05. m/z=838.78, found 727.844 (losing 2 *t*-Bu groups).

2,5-dibromo-3,6-difluoro-N,N'-di-butyloctyl-p-phenylenediamine (18): Solution of **17** (4g, 4.8mmol) in dichloromethane was cooled to 0ºC. 15ml of trifluoroacetic acid was added drop wise. The reaction was then warmed up to room temperature then stirred overnight. The mixture was then poured into 500ml water, extracted with dichloromethane. The organic layer was washed with saturated $NaHCO_3$ solution then water, dried over Na_2SO_4. After removing the solvent, crude product was purified by column chromatography (hexane/dichloromethane=5/1) to yield clear oil **18** (2.5g, 82%). ^{1}H-NMR (400 MHz, $CDCl_3$): δ (ppm) 3.61 (s, 2H), 3.14 (d, 4H), 1.52 (s, 2H), 1.27 (s, 32H), 0.89 (m, 12H). ^{13}C-NMR (100 MHz, $CDCl_3$): δ (ppm) 147.9, 145.5, 128.7, 102.4, 50.8, 38.6, 31.9, 31.7, 29.7, 28.8, 26.6, 23.1, 22.7, 14.1. m/z=638.55, found 639.26.

2,5-dibromo-3,6-difluoro-N,N'-di-butyloctyl-N,N'-di-(thiophene-3-carbonyl)-pphenylenediamine (19): Compound **18** (2.5g, 3.9mmol) and N,N-diisopropylethylamine (5.4ml, 31.2mmol) was dissolved in 15ml dichloromethane. The solution was stirred at room temperature for 40 min, and then cooled to 0ºC. A solution of thiophene-3-carbonyl chloride (3.0g, 23.4mmol) in 6ml dichloromethane was added dropwise at 0ºC. After addition, reaction was warmed up to room temperature and stirred overnight. Reaction was poured into water and extracted with dichloromethane. Organic layer was washed with water twice, dried with Na_2SO_4. After evaporated solvent, crude product was purified by column chromatography (hexane/ethyl acetate=40/3). Product **19** was obtained as pale yellow oil (1.2g, 36%). Mono-carbonyl product was also isolated (1.8g, 61%), and was carried on for a second acylation reaction. **19** consists rotamers of 2/1 ratio. ^{1}H-NMR (400 MHz, $CDCl_3$): δ (ppm) 7.23 (dd, *J*=2.8, 1.2 Hz, 0.67H), 7.16 (dd, *J*=5.2, 2.8 Hz, 1.33H), 7.08 (dd, *J*=5.2, 2.8 Hz, 0.67H), 7.06 (dd, *J*=2.8, 1.2 Hz, 1.33H), 7.02 (dd, *J*=5.2, 1.2 Hz, 1.33H), 6.98 (d, *J*=4.8 Hz, 0.67H), 4.11-4.13, 3.33-3.45 (m, 4H), 1.16-1.59 (m, 34H), 0.82-0.91(m, 12H). ^{13}C-NMR (100 MHz, $CDCl_3$): δ (ppm) 165.5, 165.3, 154.4, 152.0, 136.0, 135.9, 132.3, 132.1, 127.2, 127.1, 126.8, 125.4, 125.2, 111.8, 111.6, 52.3, 51.9, 37.3, 37.2, 31.9, 31.9, 31.7, 31.6, 31.5, 31.3, 29.6, 29.5, 29.5, 28.9, 28.8, 28.6, 26.8, 26.5, 26.3, 22.8, 22.9, 14.0. m/z=858.82, found 858.81.

FTPTQ (20): Anhydrous DMAc was bubbled with nitrogen gas for 2 h before reaction. To a round bottom flask, **19** (1.0g, 1.16mmol), KOAc (342mg, 3.48mmol) and $Pd(PPh_3)_4$ (134mg, 0.12mmol) were added. Then 100ml degased DMAc was added. The mixture was further bubbled with nitrogen for 1 h before heated at 80°C for 1.5 h. After cooled to room temperature, the mixture was poured into water, extracted with dichloromethane. The organic layer was washed with water, and then dried over Na_2SO_4. After evaporating the solvent, product was purified by column chromatography (hexane/ethyl acetate=10/1). Product **20** was obtained as yellow powder (0.44g, 54%). ^{1}H-NMR (400 MHz, $CDCl_3$): δ (ppm) 7.82 (d, *J*=5.2 Hz, 2H), 7.59 (d, *J*=5.6 Hz, 2H), 4.62 (s, 4H), 1.88 (s, 2H), 1.18-1.24 (m, 32H), 0.83 (m, 12H). ^{13}C-NMR (100 MHz, $CDCl_3$): δ (ppm) 158.9, 142.6, 140.2, 137.5, 132.0, 128.7, 126.4, 120.8, 110.7, 48.8, 37.8, 31.8, 31.3, 31.0, 29.6, 28.6, 26.4, 23.0, 22.6, 14.1, 14.0. m/z=697.00, found 697.20.

FTPTQ-ditin (21): Compund **21** was synthesized with same procedure of compound **6**. ^{1}H-NMR (400 MHz, $CDCl_3$): δ (ppm) 7.91 (s, 2H), 4.62 (s, 4H), 1.91 (s, 2H), 1.18-1.25 (m, 32H), 0.81-0.82 (m, 12H), 0.48 (s, 18H). ^{13}C-NMR (100 MHz, $CDCl_3$): δ (ppm) 159.3, 143.4, 142.8, 142.7, 140.3, 134.2, 132.7, 120.3, 110.7, 48.6, 37.7, 31.8, 31.3, 31.1, 29.6, 28.7, 26.4, 23.0, 22.6, 14.1, 14.0, -8.1. m/z =1022.29, found 1022.39.

PQP:

A mixture of compound 7 (0.120 g, 0.121 mmol), dibromo perylene diimide (PDI) (0.148 g, 0.121 mmol) and Pd(PPh3)4 (7 mg, 5 mol%), tetrakis(triphenylphosphine)palladium, was dissolved in 2ml of toluene/DMF (4:1 v/v). The mixture was degased for 30 min and then heated at 120 °C for 24 h. After cooling to room temperature, the mixture was added to methanol. The precipitate was dissolved in chloroform and filtered with Celite to remove the metal catalyst. The polymer fibers were washed by Soxhlet extraction with methanol, acetone and chloroform. The final polymer was obtained after reprecipitation with methanol, yielding 175 mg (83%). 1H-NMR (400 MHz, CDCl3): δ (ppm) 8.84 (s, 2H), 8.44 (m, 4H), 8.06 (s, 2H), 7.77 (m, 2H), 4.49 (br, 4H), 4.14 (br, 4H), 2.07 (m, 4H), 1.27 (m, 112H), 0.86 (br, 12H), 0.73 (br, 12H). Anal. calcd. for [C112H158N4O6S2]n: C, 78.18; H, 9.26; N, 3.26; O, 5.58; S, 3.73. Found: C, 77.30; H, 9.54; N, 3.18.

2, Materials and Characterization Techniques

Materials: All of the chemicals were purchased from Aldrich except for tetrakis(triphenylphosphine)palladium from Strem Chemicals. All reagents purchased commercially were used without further purification except for toluene and tetrahydrofuran (THF), which were dried over sodium/benzophenone. ^{1}H NMR and ^{13}C NMR spectra were recorded on a Bruker DRX-400 spectrometers, with tetramethylsilane as an internal reference. Matrix-assisted laser desorption ionization time-of-flight (MALDI-TOF) mass spectra were recorded using a Bruker Ultraflextreme MALDI-TOF/TOF mass spectrometer with dithranol as the matrix. Elemental analysis was performed by Midwest MicroLab. The number- and weight-average molecular weights of the polymers were determined by gel-permeation chromatography (GPC) with a Waters Associates liquid chromatography instrument equipped with a Waters 510 HPLC pump, a Waters 410 differential refractometer, and a Waters 486 tunable absorbance detector. Tetrahydrofuran (THF) was used as the eluent and polystyrene as the standard. Thermogravimetric analysis (TGA) measurement of the polymers was performed using a TA Q600 instrument. UV-vis absorption spectra were measured on a Shimadzu UV-3600. Cyclic voltammetry was performed on an AUTOLAB/PG-STAT12 model system with a three-electrode cell in a 0.1 N Bu_4NBF_4

solution in acetonitrile at a scane rate of 50 mV/s. A film of each polymer was coated onto a Pt wire electrode by dipping the electrode into a polymer solution in chloroform. All measurements were calibrated against an internal standard of ferrocene (Fc), the ionization potential (IP) value of which is -4.8 eV for the Fc/Fc+ redox system. AFM images were obtained by using an Asylum MFP-3D AFM. TEM measurements were performed by using a Tecnai F-30 with an accelerating voltage at 300 kV.

Grazing Incidence Wide-Angle X-ray Scattering (GIWAXS): GIWAXS measurements were performed at the 8ID-E beamline at the Advanced Photon Source (APS), Argonne National Laboratory using x-rays with a wavelength of $\lambda = 1.6868$ A and a beam size of ~200 μm (h) and 20 μm (v). To make the results comparable to those of OPV devices, the samples for the measurements were prepared on PEDOT:PSS modified Si substrates under the same conditions as those used for fabrication of solar cell devices. A 2-D PILATUS 1M-F detector was used to capture the scattering patterns and was situated at 208.7 mm from samples. Typical GISAXS patterns were taken at an incidence angle of 0.20°, above the critical angles of neat polymers or polymer blends and below the critical angle of while the q_z linecut was achieved by a linecut at $q_y = 0$ Å^{-1} using the reflected beam center as zero the silicon substrate. Consequently, the entire structure of thin films could be detected. In addition, the q_y linecut was obtained from a linecut across the reflection beam center. The background of these linecuts was estimated by fitting an exponential function and the parameters of the scattering peaks were obtained through the best fitting using the Pseudo-Voigt type 1 peak function.

PSC device Fabrication: Organic photovoltaic cells with a device configuration of glass/indium tin oxide (ITO)/poly(3,4-ethylenedioxythiophene):poly(styrenesulfonate) (PEDOT:PSS) /polymer blend films/Ca/Al were prepared. Prior to device fabrication, the ITO substrates were cleaned with detergent and ultrasonicated in deionized water, acetone and isopropanol, and then dried overnight in an oven. The substrate was spin-coated by a PEDOT:PSS solution without or with Au nanorod (0.01% in DI water, Nanocs, USA), dried at 100 ^{o}C in N_2 for 30 min, and then transferred to a glove box for spin-casting of the polymer layer. The solution containing a blended mixture of PTB7 (or PTB10)/acceptors in CF:DIO (3 v/v%) and in CF:CN (6 v/v%) was spin casted by 5000 rpm onto the above substrate. PTB7 (or PTB10)/acceptor films were used directily without annealing process. Subsequently, the device was pumped down under vacuum (< 10^{-6} Torr) and the Ca (20 nm) and Al (80 nm) electrode was deposited by thermal evaporation in the glove box at a chamber pressure of ~5.0×10^{-7}torr. The active area of the solar cell is 3.14 mm^2, which is defined by the cathode area. Current density-voltage

(*J*-*V*) characteristics of the devices under nitrogen were measured using a Keithley 238 Source Measure unit. The photovoltaic properties were characterized under an Air Mass 1.5 Global (AM 1.5G) solar simulator with irradiation intensity of 100 mW/cm^2.

2.3 CONCLUSION

We have developed several alternating electron accepting polymers with weak acceptor-strong acceptor (WA-SA) combination. The SA moiety is necessary for the efficient electron transfer as an acceptor. The most promising polymer is **PQP**, which exhibited a PCE of 3.52 % when coupled with plasmonic effect. The improved device performance was achieved only when 1-chloronaphthalene was used as a co-solvent, which helps to organize polymer films with favored face-on polymer chain assembly and phase separation between donor and acceptor. Despite of similar backbone structures between **PQP** and **PFP**, **PQP** devices showed much better photovoltaic performance. The results suggest that the proper internal polarization of acceptor polymers, similar to what we observed in our PTB series of donor polymers, and the face-on orientation in an active layer is highly important to optimize the photovoltaic properties in all-polymer solar cells.

2.4 References

(1) Earmme, T.; Hwang, Y. J.; Subramaniyan, S.; Jenekhe, S. A. *Advanced materials* **2014**, *26*, 6080-6085.

(2) Mori, D.; Benten, H.; Okada, I.; Ohkita, H.; Ito, S. *Energy & Environmental Science* **2014**, *7*, 2939.

(3) Jung, I. H.; Lo, W.-Y.; Jang, J.; Chen, W.; Zhao, D.; Landry, E. S.; Lu, L.; Talapin, D. V.; Yu, L. *Chemistry of Materials* **2014**, *26*, 3450-3459.

(4) Poduval, M. K.; Burrezo, P. M.; Casado, J.; López Navarrete, J. T.; Ortiz, R. P.; Kim, T.-H. *Macromolecules* **2013**, *46*, 9220-9230.

(5) Liao, Q.; Cao, J.; Xiao, Z.; Liao, J.; Ding, L. *Phys Chem Chem Phys* **2013**, *15*, 19990-19993.

(6) Jung, I. H.; Zhao, D.; Jang, J.; Chen, W.; Landry, E. S.; Lu, L.; Talapin, D. V.; Yu, L. *Chemistry of Materials* **2015**, *27*, 5941-5948.

(7) Grimm, B.; Risko, C.; Azoulay, J. D.; Bredas, J.-L.; Bazan, G. C. *Chemical Science* **2013**, *4*, 1807-1819.

(8) Lee, C.; Yang, W.; Parr, R. G. *Physical Review B* **1988**, *37*, 785-789.

(9) Tirado-Rives, J.; Jorgensen, W. L. *Journal of Chemical Theory and Computation* **2008**, *4*, 297-306.

(10) Kellogg, R. E.; Bennett, R. G. *The Journal of Chemical Physics* **1964**, *41*, 3042-3045.

(11) Pommerehne, J.; Vestweber, H.; Guss, W.; Mahrt, R. F.; Bässler, H.; Porsch, M.; Daub, J. *Advanced Materials* **1995**, *7*, 551-554.

(12) Ruoff, R. S.; Kadish, K. M.; Boulas, P.; Chen, E. C. M. *The Journal of Physical Chemistry* **1995**, *99*, 8843-8850.

(13) Li, W.; Roelofs, W. S. C.; Turbiez, M.; Wienk, M. M.; Janssen, R. A. J. *Advanced Materials* **2014**, *26*, 3304-3309.

(14) Yu, L. P., Liang, Y. Y., He, F. In *PCT Int. Appl. (2013), WO 2013116643 A1 20130808.* .

(15) Carsten, B.; Szarko, J. M.; Son, H. J.; Wang, W.; Lu, L.; He, F.; Rolczynski, B. S.; Lou, S. J.; Chen, L. X.; Yu, L. *Journal of the American Chemical Society* **2011**, *133*, 20468-20475.

(16) Goh, C.; Kline, R. J.; McGehee, M. D.; Kadnikova, E. N.; Fréchet, J. M. J. *Applied Physics Letters* **2005**, *86*, 122110.

(17) Keshtov, M. L.; Marochkin, D. V.; Kochurov, V. S.; Khokhlov, A. R.;

Koukaras, E. N.; Sharma, G. D. *J. Mater. Chem. A* **2014**, *2*, 155-171.

(18) Lu, L.; Luo, Z.; Xu, T.; Yu, L. *Nano letters* **2013**, *13*, 59-64.

Chapter 3 Investigation of α-substituted PDI dimers

This chapter contains parts of the published work [Zhao, D.; Wu, Q; Cai, Z. *et al. Chem. Mater.* **2016**, 2*8*, 1139–1146] Copyright (2016) American Chemical Society.

3.1 Introduction

From the results presented in Chapter 2, we can see that perylene diimide (PDI) is the most promising motif for use in electron-deficient acceptors for OPV applications. [1,2,3] PDI exhibits several appealing properties: low cost, chemical robustness, ease of functionalization, suitable optical absorption range, and low HOMO/LUMO. [4-6] Due to the strong tendency toward aggregation of the extended conjugated backbone in PDI, two strategies were adopted to reduce the strong π-stacking, in order to enhance the processibility of materials and form favorable BHJ domains. One is to disrupt the strong π-π interaction of PDI by introducing torsion in the conjugated backbone, such as twisted PDI connected at N-position or bay-positions (1,6,7,12-positions).[7-12] Another is to synthesize A-D-A (Acceptor-Donor-Acceptor) molecules with donor coupled to PDIs at the bay positions. [5,13,14] Both approaches have been effective in generating non-fullerene electron acceptors that show improved OPV performance comparing to single PDI molecules.[5,15] Unfortunately, the functionalization at the bay-positions of PDI leads to twisting of perylene core, disrupt the close π-stacking of π-surface and diminishs the electron transport in bulk state, thus limiting OPV performance.[16-19] Therefore, strategies to functionalize PDI without introducing torsion in the perylene core are desirable. In this chapter, the design and synthesis of α-monobrominated PDI and developed A-D-A and A-wA-A acceptors by coupling donor (D)/weak acceptor (wA) with α-bromo PDI is described. Detailed studies indicate that α-substituted PDI derivatives with A-D-A structure are indeed promising electron acceptors.

3.2 Result and discussion

3.2.1 Design and Synthesis of compounds.

The selective functionalization of the ortho-position (2,5,8,11-positions) of PDI by introducing boron, alkyl and aryl substituent are known, [20-23] by which the optical, electrical, packing and film-forming properties of PDI derivatives can be tuned. Evidence exists that the perturbation of the planarity of the perylene core due to functionalization at ortho-position of PDI is minimized.[24,25] Furthermore, functional groups in the ortho-position exert limited steric hindrance with PDI. Structural analysis on single crystals of NDI-4TH showed that due to the strong interaction between oxygen (C=O in NDI) and proton (C-H in adjacent thiophene), [26] the dihedral angle between thiophene rings and NDI core is only 25° which is much smaller than simulated dihedral angle (55°

- 60°) between adjacent thiophene ring and PDI when thiophene attached at bay-position of PDI.[27] Considering the similarity between ortho-position of NDI and PDI, it is safe to assume that connecting aromatic units such as thiophenyl groups at the ortho-position of PDI can significantly increase the coplanarity of the desired compounds which will benefit electron transport properties. Based on these considerations, we synthesized α-monobrominated PDI as a new building block to develop electron acceptors. In our previous work, we demonstrated that polarity in acceptor polymers is also important for achieving high solar cell efficiency. [28] To compare the effect of polarity, we developed A-D-A and A-wA-A acceptors. BDT-Th is used as the donor. Pyrene diimide (PID) was successfully synthesized and used as the weak acceptor. This novel five ring diimide allows functionalization at 2,7-positions that are much less structural-hindered than other diimides such as PDI and NDI. [29]

The α-monobrominated PDI (compound **4**, **5**) was synthesized in a two-steps one-pot reaction. The α-position of PDI was first functionalized with pinacolatoboron (Bpin) group in the modified Ir-catalyzed reaction, developed by Shinokubo and Osuka group. [22] The reaction mixture was treated with $CuBr_2$ without separation. The synthesis of the weaker acceptor PID-2Bpin started from commercially available material 1,2,3,6,7,8-hexahydropyrene, which was brominated with bromine for 30 minutes, yielding 4,5,9,10-tetrabromo-1,2,3,6,7,8-hexahydropyrene. Use of excessive amount of bromine in the reaction medium can convert 4,5,9,10-tetrabromo-1,2,3,6,7,8-hexahydropyrene to 4,5,9,10-tetrabromopyrene (compound **1**) under light. Compound **1** was then cyanated to compound **2**, which is further hydrolyzed into compound **3**. Because compounds **1**, **2**, **3** exhibit poor solubility in common solvent, the crude products were directly used for the next step reaction without further purification. Imidization with alkylamine led to the formation of PID. It was found that reaction of PID with bromine in a $CHCl_3/CF_3COOH/H_2SO_4$, leads to undesired bromination at 1, 3, 6, 8-positions. Selective functionalization of 2,7-positions of PID with Bpin was realized by a sterically controlled Ir-catalyzed reaction.[42] The target compounds, **αPPID**, **βPPID**, **αPBDT** and **βPBDT**, were synthesized via palladium mediated Stille or Suzuki coupling reaction. These compounds exhibit high solubility in common solvent such as chloroform, chlorobenzene. Their structures were characterized and confirmed via various spectroscopic techniques, which are shown in supporting information.

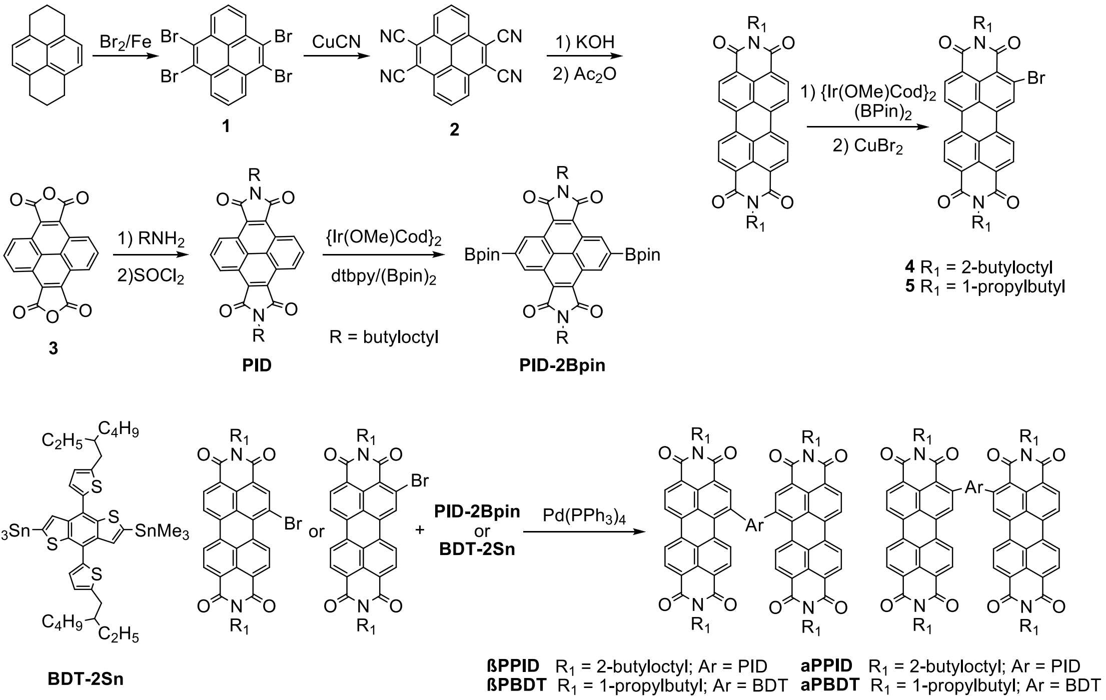

Figure 3.1 The synthetic procedure of PDI-2Bpin and synthesis of αPPID, βPPID, αPBDT and βPBDT.

3.2.2 Electronic and Optical Properties.

Cyclic voltammetry (CV) was employed to investigate the electrochemical properties of these compounds (Figure 3.2a). LUMO energy levels for different imide building motif were determined to be -3.16 eV for PID, -3.57 eV for NDI and -3.83 eV for PDI, the trend of which is in agreement with that obtained from theoretical calculation. This high LUMO suggests that PID is a weak acceptor subunit and that the electron-withdrawing ability of five-member diimide is weaker than that of six-member diimide.[30] The LUMO and HOMO energy values of the four compounds, **αPPID**, **βPPID**, **αPBDT** and **βPBDT**, are listed in Table 3-1. The four compounds show nearly identical LUMO energy levels, while the HOMO energy levels of compounds containing PID are slightly lower than those of **αPBDT** and **βPBDT** because of the electron-withdrawing nature of PID and electron-donating nature of BDT. The HOMO/LUMO energy levels for the four compounds all match well with those of **PTB7-Th**, with enough energy offset for both electron and hole transfer to each other to be facile. [31]

Table 3-1 Electrochemical and optical data and DFT calculation results of αPPID, βPPID, αPBDT and βPBDT.

	LUMO (eV)	HOMO (eV)	LUMO $(eV)^{Cal}$	HOMO $(eV)^{Cal}$	Dihedral angle (°)	Bay angle (°)	I^{00}/I^{01} sol	I^{00}/I^{01} film	QY (%)
αPPID	-3.84	-5.86[a]	-3.51	-6.04	61.4	3.2	0.80	0.77	14
βPPID	-3.79	-5.87[a]	-3.51	-5.96	57.6	17.7	1.38	0.98	43
αPBDT	-3.78	-5.60	-3.47	-5.97	58.6	4.2	1.52	0.88	0.25
βPBDT	-3.76	-5.64	-3.46	-5.53	54.4	16.8	1.33	1.11	0.01

[a] The HOMO energy level was calculated by the equation of $E_{HOMO} = E_{LUMO} - E_g^{opt}$

UV-Vis absorption spectra of the four compounds are rec-orded both in solution and in solid film (Figure 3.2 2b, 2c). They all exhibit the three vibronic peaks, resembling to PDI monomer. [21,22] The β-isomers showed red-shifted band edges, likely due to more extended electron delocalization or more twisted PDI units. However, the absorption peaks for **αPPID** at 495nm in solution are stronger than other three compounds and resemble to its film absorption, which suggest a strong tendency of **αPPID** to form aggregate in the dilute solution. In absorption spectra of films, both α-substituted compounds exhibit stronger 0-1 (I^{01}) absorption peak than 0-0 (I^{00}) transition, while β-substituted compounds show similar or weaker intensity for 0-1 in solid state than 0-0 transition. The decrease in the ratio of 0-0 to 0-1 transition intensity from solution to solid state for four compounds (blue-shift in absorption maxima) indicates the formation of H-aggregate. The largest decrease of **αPBDT** implies the strong intermolecular π-π interaction and high packing order of **αPBDT**, which is beneficial for charge transporting [16,32,33 34].. The solution emission spectra for the four compounds are showed in Figure 3.2 d and the quantum yield (QY) for the emission is shown in Table 3-1. The **αPBDT** and **βPBDT** have similar, but weak emission spectra (low QY) which are resemble to that of PDI monomer, which may indicate quenching caused by intramolecular charge transfer. The intramolecular charge transfer property also explains the lack of excimer formation in **βPBDT** and **βPBDT**. The **αPPID** and **βPPID** show the large red shift emission peak. The **αPPID** also shows a concentration-dependent emission spectrum (See Figure 3.3), indicating the formation of excimers, as evidenced by the broad peak at 600-700 nm that coincide with reported PDI excimer [34-37]. The results indicate that the π-system in **αPPID** is closed packed due to its good planarity. The excimer emission in **αPPID** is overlapped with the weak emission from monomeric **αPPID**. The emission spectrum of **βPPID** only has one peak at 579nm which corresponds to 1-0 transition of PDI, which may be due to special electronic features of the twisted PDI core.

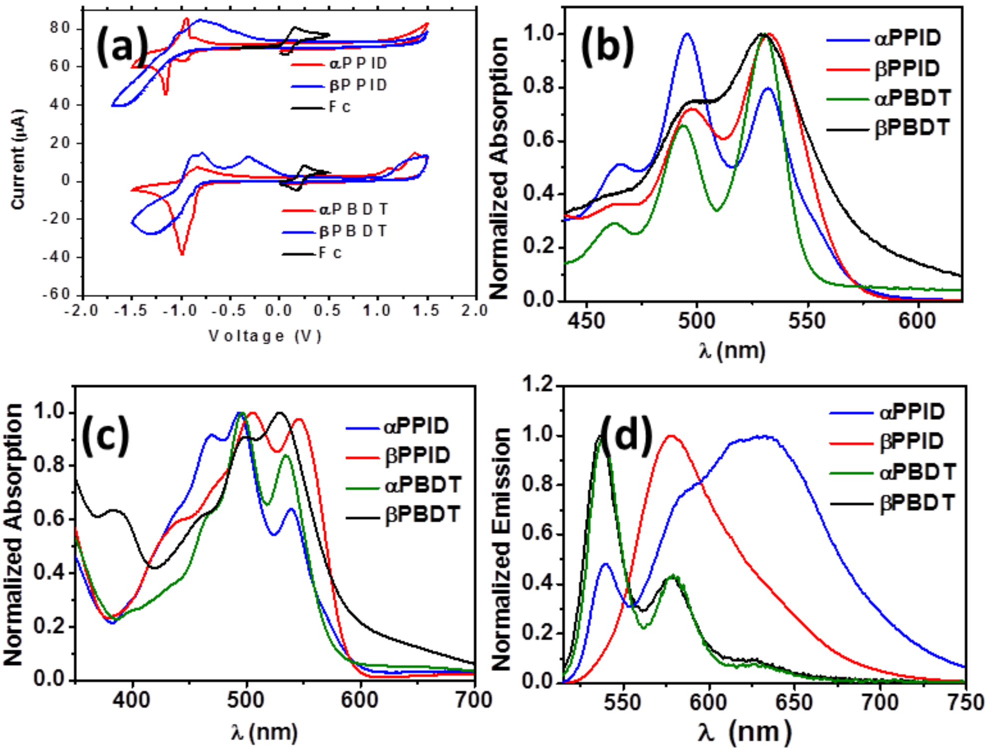

Figure 3.2 Cyclic voltammograms (CV), absorption and emission spectra of αPPID, βPPID, αPBDT and βPBDT: a) the film CV; b) solution absorption, c). film absorption, d) solution emission.

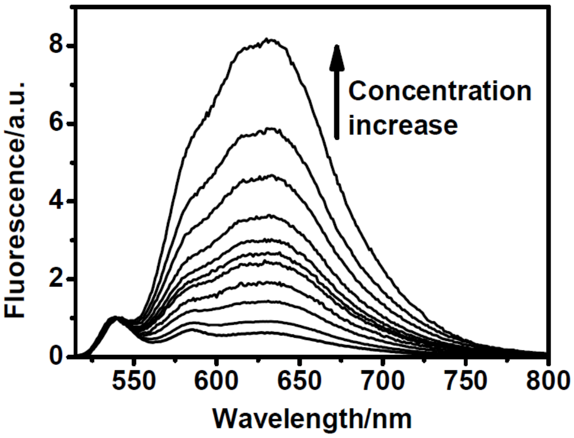

Figure 3.3 Concentration dependence fluorescence study of αPPID dissolved in chlorobenzene. Spectra were normalized at 0-0 transition emission peak (535 nm). Concentration was gradually increased from 2.1x10^{-9} M to 1.0x10^{-6} M. (Concentration from low to high: 2.1x10^{-9} M, 6.3x10^{-9} M, 1.9x10^{-8} M, 5.6x10^{-8} M, 1.1x10^{-7} M, 1.7x10^{-7} M, 2.5x10^{-7} M, 3.8x10^{-7} M, 5.7x10^{-7} M, 8.0x10^{-7} M, 1.0x10^{-6} M.)

3.2.3 DFT calculation.

In order to gain more insight into the structural and electronic difference between α-substituted and β-substituted PDIs, density functional theory (DFT) calculations by using the Gaussian package D3BJTPSS/def2-TZVP were carried out to evaluate the frontier molecular orbitals and structures of the four compounds. To facilitate the calculation, the long alkyl chains were replaced with a methyl group. A pictorial presentation of the LUMO and HOMO orbitals of the four compounds is shown as Figure 3.4, and the energy levels and torsional angles are summarized in Table 3-1. The torsion angle of the PDI backbone at the bay area is 2.0° for αPPDI and 4.5° for **αPBDT**, which is much smaller than 20.2° for βPPDI and 18.9° for **βPBDT**. The dihedral angle between the linker and PDI for α-PDI derivatives is similar to that for β-isomers, according to the calculation. Thus, the good planarity of α-position functionalized PDI could facilitate close packing and enhance electron transport.

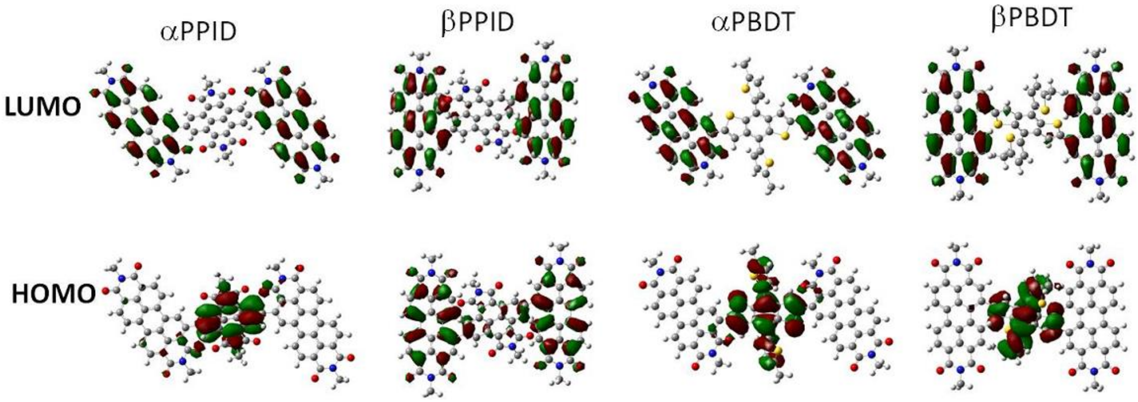

Figure 3.4 Calculated LUMO and HOMO of four compounds αPPID, βPPID, αPBDT and βPBDT.

3.2.4 OPV Properties and active layer characterization.

From the CV studies, the energy levels of these com-pounds as acceptors match with those of **PTB7-Th** as donor. We prepared the inverted solar cells with configuration of ITO/ZnO/Active Layer/MoO_3/Al to evaluate the photovoltaic properties of these small molecules. Donor/acceptor ratio of 1:1.5 was spin-casted from hot chlorobenzene with 5% 1-chloronaphthalene as additive and the active layer with the thickness of ~100 nm are formed. The above condition to make active layer gives the best OPV performance for all four PDI-based mole cules. The *J-V* characteristics of these OPV cells are shown in

Table 3-2 and *J-V* curves are plotted in Figure 3.5. The device results demonstrate that αPDI based acceptors show very similar V_{oc} with that of βPDI based acceptors if they are connected by the same liker, which is anticipated due to the similarity between their LUMO energy levels.[38] For the BDT linked acceptors, the average PCE of 4.76 % for **αPBDT** is achieved with J_{sc} of 12.74 mA/cm^2, V_{oc} of 0.81 V and *FF* of 0.46, which is 36 % higher than that for **βPBDT**. The PCE enhancement is largely due to much higher J_{sc} (12.74 mA/cm^2) values for **αPBDT** than that (9.80 mA/cm^2) for **βPBDT**. The slightly higher PCE of 3.49 % for **αPPID** than that of 3.20 % for **βPPID** can be attributed to a better intermolecular packing in **αPPID** than in **βPPID**. This is consistent with the smaller twisted angle in the αPDI moiety in DFT calculation and the excimer formation in **αPPID** solution shown by the emission spectrum, which led to a better J_{sc} value of 10.15 mA/cm^2 than that (9.14 mA/cm^2) for **βPPID**. These results indicated that acceptors based on αPDI exhibit superior photovoltaic performance over that of βPDI based acceptors. The bottleneck for these devices is the low fill factor value of 0.45±0.01, which is far behind polymer/fullerene devices' values (>0.6).[10,39,40] Further device optimization is underway to explore the potential of αPDI-based acceptors.

Table 3-2 The parameters summary of solar cell devices with αPPID, βPPID, αPBDT and βPBDT as acceptors and PTB7-Th as donor.

Acceptor	J_{sc} (mAcm^{-2})	V_{oc} (V)	*FF*	*Eff* (%) (best device)	μ_e (cm^{2}V^{-1}s^{-1})	RMS (nm)
αPPID	10.15±0.5	0.77±0.01	0.44±0.01	3.49±0.12 (3.61)	4.46×10^{-5}	0.7
βPPID	9.14±0.4	0.78±0.01	0.45±0.01	3.20±0.27 (3.47)	3.48×10^{-5}	0.7
αPBDT	12.74±0.4	0.81±0.01	0.46±0.01	4.76±0.16 (4.92)	8.00×10^{-5}	1.0
βPBDT	9.80±0.3	0.81±0.01	0.44±0.01	3.49±0.04 (3.53)	4.81×10^{-5}	0.9

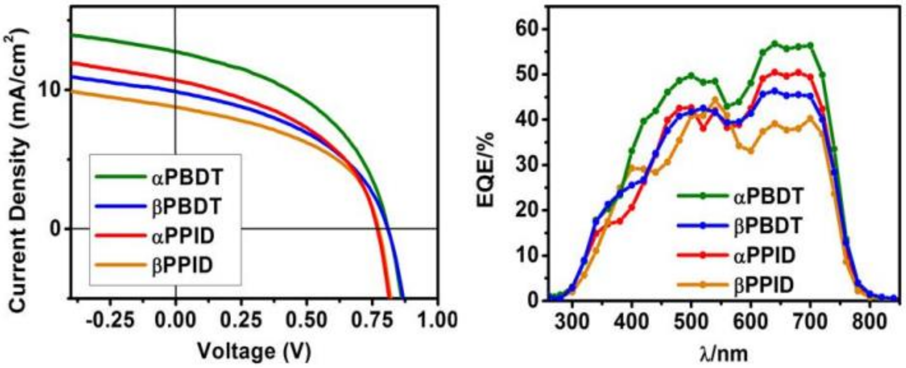

Figure 3.5 a) *J-V* characteristics of solar cell devices using αPPID(red), βPPID(orange), αPBDT(green) and βPBDT(blue) as acceptors and PTB7-Th as donor. b) External quantum efficiency spectra of PTB7-Th with αPPID (red), βPPID (orange), αPBDT(green) and βPBDT(blue).

The external quantum efficiency (EQE) of the optimal **αPPID/βPPID/αPBDT/βPBDT**:**PTB7-Th** devices were measured and are shown in Figure 3.5b. The J_{sc} values calculated from EQE all have less than 10% deviation from J_{sc} measured in solar cell device. The results shed some lights on PCE performance of these OPV cells. It can be seen that all of the four devices showed broad EQE spectra from 300 nm to 800 nm. The photon absorption for donor polymer **PTB7-Th** is between 550 nm to 800 nm. In this region, the quantum efficiency for **PTB7-Th** blended with α isomers is higher than **PTB7-Th** blends with related β isomers, indicating more efficient charge separation with α isomers. The quantum efficiency for **αPBDT** is obviously higher than all others in the whole spectrum.

The absorption spectrum of the active layer blends were further measured and recorded in Figure 3.6. It was found that the absorption spectrum of **αPPID** and **αPBDT** in the blend film is very similar with that in pure film. The **αPPID** and **αPBDT** not only maintain the two sharp and distinctive perylene diimide's 0-0 and 0-1 vibrational peaks at 540nm and 495nm, but also have a shoulder of 0-2 transition at 450nm. However, in **βPPID** and **βPBDT**'s blend films, 0-0 and 0-1 transitions are broadened and almost merged with each other, and 0-2 transition totally disappeared, which is different with their pure film absorption spectrum. A possible explanation for this phenomenon is that the **αPPID** and **αPBDT** blend films maintain the same packing order as in the pure **αPPID** and **αPBDT** domains.

The grazing-incidence wide-angle X-ray scattering (GIWAXS) measurement was employed to investigate the crystallinity of the neat and blend films (Figure 3.7). The in-plane GIWAXS patterns of neat **PTB7-Th**, **αPPID**, **βPPID**, **αPBDT**, **βPBDT** films and their blend films were shown in Figure 3.6. The neat films of PTB7-Th, **αPPID**, **βPPID**, **αPBDT** and **βPBDT** shows the Bragg reflections at $q_y \approx 0.27$, 0.31, 0.305, 0.34 and 0.34 Å^{-1} corresponding to d-spacing of 23.3, 20.3, 20.6, 18.5 and 18.5 Å, respectively. This peak can be assigned to lateral spacing along the side chains. The **βPPID/PTB7-Th** and **βPBDT/PTB7-Th** blend films both exhibit the Bragg reflections at qy ≈ 0.28 Å^{-1} (22.4 Å) that are very close to 0.27 Å^{-1} for the neat donor polymer PTB7-Th. Three diffraction peaks at 0.275 Å^{-1} (22.8 Å), 0.33 Å^{-1} (19.0 Å) and 0.40 Å^{-1} (15.7 Å) was observed for **αPBDT/PTB7-Th** blend film. The peaks at 0.275 Å^{-1} and 0.33 Å^{-1} are from the diffraction of **PTB7-Th** and **αPBDT** respectively, which implies both pure donor and acceptor domains exist in the blend film. This result is in good agreement with the observation in the absorption spectrum of **αPBDT/PTB7-T**h blend film. The **αPPID/PTB7-Th** blend film demonstrates two diffraction peaks at 0.305 Å^{-1} (18.0 Å) and 0.40 Å^{-1} (15.7 Å). The peaks at 0.305 Å^{-1} are most likely from the diffraction of **αPPID**. However, it is surprising to observe the enhanced sharp peak at q_y value of 0.40 Å^{-1}. It seems that the polymer/acceptor interaction directed **αPBDT** to self-assemble in more ordered structures, which may be the reason for observed high electron mobility. The blend film absorption and GIWAXS data both confirm that α isomers of these acceptors (**αPPID**, **αPBDT**) maintain the pure domains and the same packing order in the blend films, which may be due to their strong intermolecular interaction resulting from good planarity of α substituted PDI derivative.

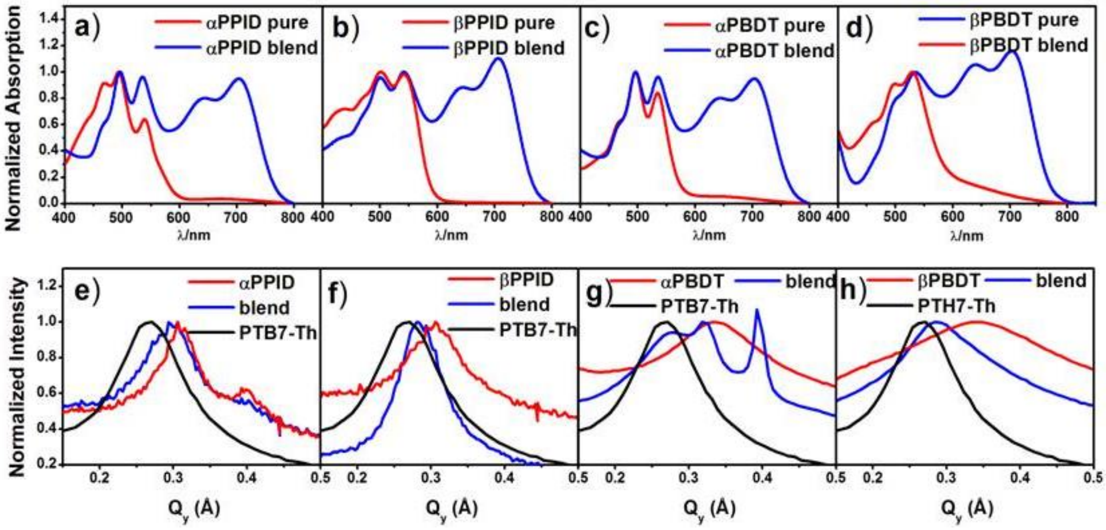

Figure 3.6 The absorption spectrum of a) neat αPPID and αPPID/PTB7-Th blend film; b) neat βPPID and βPPID/PTB7-Th blend film; c) neat αPBDT and αPBDT/PTB7-Th blend film; d) neat βPBDT and βPBDT /PTB7-Th blend film. The in-plane 2D GIWAXS patterns of: e) neat PTB7-Th, αPPID and their blend film; f) neat PTB7-Th, βPPID and their blend film; g) neat PTB7-Th, αPBDT and their blend film; h) neat PTB7-Th, βPBDT and their blend film.

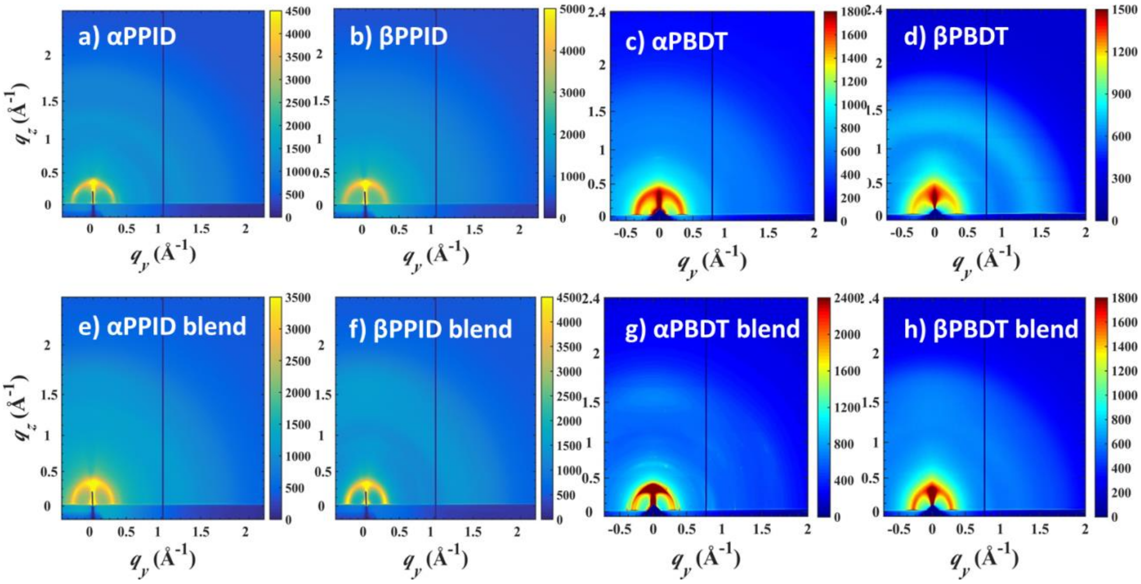

Figure 3.7 2D GIWAXS patterns of films on PEDOT:PSS-modified Si substrates. a–h, 2D GIWAXS patterns of pristine αPPID (a), pristine βPPID (b), pristine αPBDT (c), pristine βPBDT (d), PTB7-Th: αPPID (1:1.5) (e), PTB7-Th: βPPID (1:1.5) (f), PTB7-Th: αPBDT (1:1.5) (g) and PTB7_Th: βPBDT (1:1.5) (h).

The electron mobility of these four devices also help to understand the structure/property relationship, which was measured by space-charge-limited current method with the device structure is ITO/ZnO/PDIs:**PTB7-Th**/Ca/Al. The electron mobility was calculated to be 4.46×10^{-5}, 3.48×10^{-5}, 8.00×10^{-5} and 4.81×10^{-5} cm^2/Vs for **αPPID**, **βPPID**, **αPBDT** and **βPBDT** respectively (Summarized in Table 3-2) . It is clear that the αPDI based ones exhibited relatively higher electron mobility than the βPDI based compounds, which is likely the consequence of better planarity of α substituted PDI moieties and stronger intermolecular interaction of **αPPID** and **αPBDT** as showed in film absorption spectrum.

The active blend films of these devices exhibited similar morphology as characterized by atomic force microscopy (AFM) and transmission electron microscopy (TEM) (Figure 3.8). AFM height images in Figure 3.8 (2 μm × 2 μm dimension) show device blends have similar feature and comparatively smooth. Root mean square (RMS) roughness values of **αPPID** and **βPPID** blend films are both 0.7 nm while the surface for blend films of BDT linked compounds are rougher with RMS value of 1.0 nm, 0.9 nm for **αPBDT** and **βPBDT**, respectively (Table 3-2). TEM images of the four blends are also similar, this is probably due to the weak contrast between donor polymer and non-fullerene acceptor. The AFM and TEM studies suggest the solar cell efficiency difference between the four compounds is not resulted from the blend film morphology.

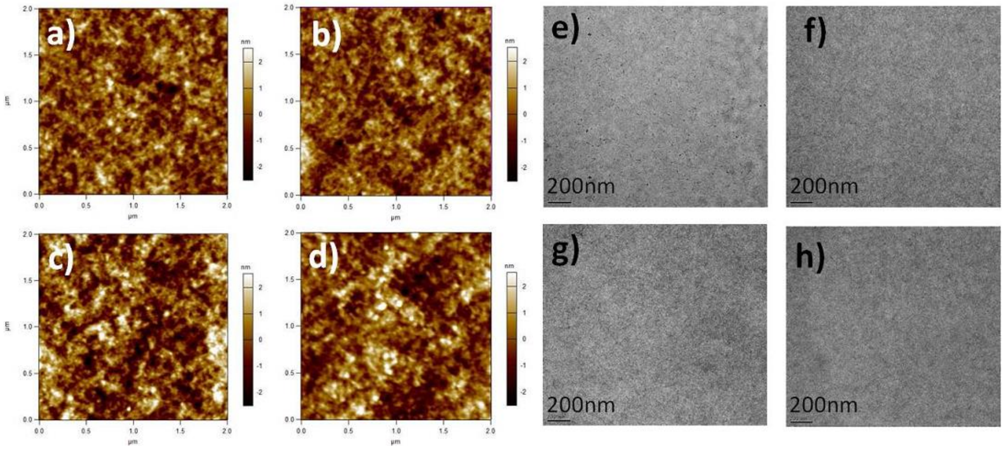

Figure 3.8 The atomic force microscopy (AFM) of films of: a) αPPID/PTB7-Th; b) βPPID/PTB7-Th; c) αPBDT/PTB7-Th; d) βPBDT/PTB7-Th. The transmission electron microscopy (TEM) images of the films of: e) αPPID/PTB7-Th; f) βPPID/PTB7-Th; e) αPBDT/PTB7-Th; e) βPBDT/PTB7-Th.

To better understand the OPV performance, the exciton dissociation and carrier collection process, the charge dissociation probability $P(E, T)$ were investigated according to the reported method. [5,41,42] As shown in Figure 3.9a, photo current density J_{ph} (defined by $J_L - J_D$, J_L and J_D are light and dark current densities) is plotted against effective voltage V_{eff} (defined by V_0-V, V_0 is voltage where J_{ph}=0) in logarithmic scale. Assuming that the J_{ph} reaches its saturation (J_{sat}) at high reverse voltage which means all the photogenerated exitons are dissociated to free charge carriers and collected by the electrodes. The $P(E, T)$ is defined as J_{ph}/J_{sat}. The calculated $P(E, T)$ under J_{sc} condition for **βPPID** and **βPBDT** are both 79%, while **αPPID** and **αPBDT** devices have higher dissociation probabilities of 83% and 88%. The higher $P(E,T)$ values of **αPPID** and **αPBDT** indicate the more efficient exciton dissociation at interfaces between αPDI based compounds and **PTB7-Th** which is in good agreement with higher J_{sc} values of **αPPID** and **αPBDT** based devices. In order to gain more insight into the recombination kinetics, the measurement of the J_{sc} as a function of illumination intensity were carried out according to literature.[43,44] In Figure 3.9b, the linear scaling of photocurrent to light intensity was observed for all four devices and the exponential factors for **αPPID**:**PTB7-Th**, **βPPID**:**PTB7-Th**, **αPBDT**:**PTB7-Th**, **βPBDT**:**PTB7-Th** devices are 0.95, 0.94, 0.93 and 0.95 respectively. The high and similar values mean that the bimolecular recombination in the four devices is all comparatively weak, which is consistent with their high electron mobility.

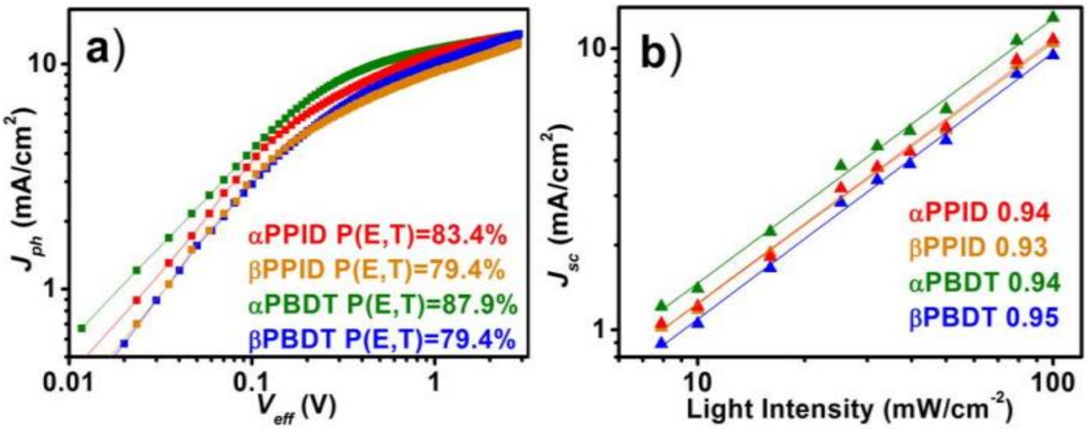

Figure 3.9 (a) photocurrent density (J_{ph}) versus effective voltage (V_{eff}) characteristics of the four devices; (b) short current density (J_{sc}) versus the light density of the four devices..

3.2.5 Experimental section

1, Synthesis and characterization

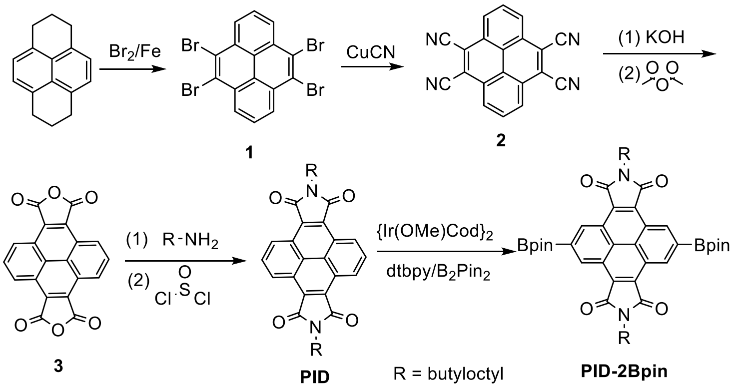

Compound **1**

1,2,3,6,7,8-hexahydropyrene (3.12 g), Bromine (27.17 g), iron powder (0.59 g) and 100 ml dichloromethane were added to a 250 mL round bottom flask and refluxed overnight.

The precipitate was filtered and washed with acetone (3×200 ml) and boiling chloroform (3×200 ml). 6.52g 4,5,9,10-tetrabromopyrene was obtained in the yield of 84%. MS (MALDI-TOF) m/z : 518.15 $(M+H)^+$

Compound **2** and **3**

4,5,9,10-tetrabromopyrene (6.20 g), CuCN (8.60 g) and anhydrous NMP were added to a 250 mL round bottom flask under nitrogen atmosphere and reacted at 200 °C for 2 hours. After cooling down, the solution was poured into saturated ammonium. The precipitate was filtered and washed with ammonium, acetone and boiling chloroform. Without further purification, the insoluble solid was added to the KOH (13.5 g) solution in $HOCH_2CH_2OH$ (60 mL) and water (15 mL) and heated to 160 for 48 hours. After cooling down to 0, concentrated hydrochloric acid were added dropwise to pH = 1. The precipitate was filtered and washed with water and acetone. The obtained crude product was refluxed in acetic anhydrate (60 ml) overnight. 0.65 g yellow product was obtained by filtration. The yield for three-step reactions is 15.8 %. The compound **2** sparingly dissolve in the common solvent.

Compound PID

0.34 g compound **2** and 0.56 g 2-butyloctylamine in 20 ml anhydrous toluene was heated to reflux for 5 hours. After removing the solvent under reduced pressure, the reaction mixture was added thionyl chloride (5 ml) and refluxed for 2 hours. The thionyl chloride was removed under reduced pressure. The crude product was purified by column chromatography, using dichloromethane as the eluent. 0.51 g compound **3** was obtained (yield: 76%). ^{1}H NMR (400 MHz, $CDCl_3$) δ (ppm): 9.49 (d, J = 80 Hz, 4H), 8.28 (T, J = 80 Hz, 2H), 3.74 (d, J = 72 Hz, 4H), 2.0 (m, 2H), 1.35 (br, 32H), 0.90 (br, 12H). ^{13}C NMR (500 MHz, $CDCl_3$) δ 14.096, 14.127, 22.663, 23.072, 26.391, 28.607, 29.707,31.276, 31.618, 31.861, 37.328, 42.367, 124.484, 126.721, 128.244, 128.715, 128.810, 169.792. MS (MALDI-TOF) m/z: 677.13 $(M + H)^+$

Compound PID-2Bpin

{Ir(OMe)Cod} (33 mg), 4,4'-di-tert-butyl-2,2'-dipyridyl (66 mg) and $(BPin)_2$ (64 mg) were mixed in20 ml anhydrous hexane under N_2 atmosphere. Then the mixture were transfer to sealed tube which contains compound 3 (0.338 g) and $(BPin)_2$ (0.254 g). After reacting at 120 °C for 24 hours, the solvent was removed under reduced pressure. 0.288 g of pure compound 4 (62 %) was obtained by column chromatography, using dichloromethane as the eluent. ^{1}H NMR (400 MHz, $CDCl_3$) δ (ppm): 9.86 (s, 4H), 3.76 (d, J = 72 Hz, 4H), 2.0 (m, 2H), 1.50 (s, 24H)1.35 (br, 32H), 0.88 (br, 12H). ^{13}C NMR (500 MHz, $CDCl_3$) δ 14.102, 14.179, 22.660, 23.122, 25.133, 26.605, 28.872, 29.776, 31.420, 31.756, 31.918, 37.388, 42.662, 84.636, 123.678, 128.034, 129.296, 132.428, 169.447.

MS (MALDI-TOF) m/z: 929.97 (M + H)$^{+}$.

Compound **βPPID**

$Pd_2(dba)_3$ (9 mg)and $P(MeOPh)_3$ was added to the mixture of compound **4** (104 mg), compound **3** (60 mg), THF (8 mL) and 2M K_2CO_3 aqueous solution (2 mL) under nitrogen. After refluxing overnight, the mixture was poured into methanol. The red precipitate was filtered and purified by column chromatography, using chloroform as the eluent. 96 mg of pure **βPPID** (70%) was obtained. ^{1}H NMR (400 MHz, $CDCl_2CDCl_2$) δ (ppm): 9.79 (s, 4H), 8.78 (br, 10H), 7.90 (d, J = 84 Hz 2H), 7.63 (d, J = 84 Hz 2H), 4.1 (br, 8H), 3.59 (br, 4H) 2.1 (br, 6H), 1.26 (br, 96H), 0.90 (br, 36H). MS (MALDI-TOF) m/z : 2125.68 (M^{+}). Anal. Calcd for $C_{140}H_{168}N_6O_{12}$: C, 79.06; H, 7.96; N, 3.95. Found: C, 79.12; H, 8.06; N, 4.04.

Compound **αPPID**

αPPID was synthesized according to the same procedure as **βPPID** in the yield of 76%. ^{1}H NMR (400 MHz, $CDCl_2CDCl_2$) δ (ppm): 9.37-9.72 (br, 4H), 8.98-7.73 (br, 14H), 4.36-3.71 (br, 12H), 2.20-1.98 (br, 6H), 1.33 (br, 96H), 0.90 (br, 36H). MS (MALDI-TOF) m/z : 2125.82 (M^{+}) Anal. Calcd for $C_{140}H_{168}N_6O_{12}$: C, 79.06; H, 7.96; N, 3.95. Found: C, 79.49; H, 8.14; N, 4.05.

Compound **βPBDT**

$Pd_2(dba)_3$ (9 mg)and P(o-tolyn)$_3$ (24 mg)was added to the mixture of compound **4** (133 mg), compound **6** (90.5 mg) and dry toluene (6 mL) under nitrogen. After refluxing overnight, the mixture was poured into methanol. The dark red precipitate was filtered and purified by column chromatography, using chloroform as the eluent. 120 mg of pure **βPBDT** (69%) was obtained. ^{1}H NMR (400 MHz, $CDCl_2CDCl_2$) δ (ppm): 8.69-8.35 (br, 14H), 7.95 (s, 2H), 7.37 (br, 2H), 6.80 (br, 2H), 5.21-5.17 (br, 4H), 2.74 (br, 4H), 2.20 (br, 16H), 1.83 (br, 16), 1.56 (br, 2), 1.32 (br, 32H), 0.96-0.81 (br, 36H). MS (MALDI-TOF) m/z: 1746.60 (M^+) Anal. Calcd for $C_{110}H_{114}N_4O_8S_4$: C, 75.57; H, 6.57; N, 3.20. Found: C, 75.48; H, 6.64; N, 3.20.

Compound **αPBDT**

αPBDT was synthesized according to the same procedure as **βPBDT** in the yield of 80%. ^{1}H NMR (400 MHz, $CDCl_2CDCl_2$) δ (ppm): 8.74-8.69 (br, 14H), 7.86 (s, 2H), 7.51 (br, 2H), 6.91 (br, 2H), 5.21-5.11 (br, 4H), 2.83 (br, 4H), 2.24 (br, 16H), 1.85 (br, 16), 1.65 (br, 2), 1.35 (br, 32H), 0.90 (br, 36H). MS (MALDI-TOF) m/z: 1746.58 (M^+) Anal. Calcd for $C_{110}H_{114}N_4O_8S_4$: C, 75.57; H, 6.57; N, 3.20. Found: C, 75.86; H, 6.54; N, 3.34.

2. Device fabrication

Polymer **PTB7-Th** was obtained from 1-material. $ZnAc_2$• $2H_2O$, 2-methoyethanol and ethanolamine were purchased from Sigma-Aldrich. Zinc Oxide Sol-Gel stock solution was prepared by stirring 0.46 g $ZnAc_2•2H_2O$ in 5ml 2-methoxyethanol and 0.15 ml ethanol amine at 60 °C under ambient condition. Then the solution was cooled to room temperature and subsequently filtered from 0.45μm PTFE film before use. The **PTB7-Th** and small molecule acceptors were co-dissolved in chlorobenzene and chloronaphthalene (95:5 vol/vol). The overall material concentration was 15 mg ml^{-1} and the solution was stirred at 110 °C for 12 h under a N_2 atmosphere. ITO glass substrate (Thin Film Devices) was cleaned in water, acetone and isopropylalcohol for 15 min under sonication. Glasses were then exposed to ultraviolet ozone irradiation for 30 min. Athin layer (~40 nm) of ZnO sol-gel was spin-coated at 4,000 rpm for 40 sec onto ITO glasses and annealed at 200 °C in ambient condition for 30 min. After treated ZnO surface with 1 % ethanolamine solution in methoxyethanol (3000 rpm for 40 s), the substrates were dried in 90 °C oven then transferred into glovebox immediately. Active layers were spin-coated using the as-prepared solutions at 1,000 rpm in a glove box. MoO_3 (7.5 nm) and Al (80 nm) anodes were thermal evaporated in a glove box at a chamber pressure of ~2.0 × 10−6 torr.

3. Solar cell characterization.

J–V characteristics of the solar cells were measured under 1 sun, AM 1.5G irradiation (100 mWcm−2) from a solar simulator with a xenon arc lamp (Oriel model 69920). Masks with a well-defined area of 3.14 mm^2 were used to determine the effective area of the *J–V* measurement. Light intensity was calibrated using an NREL-certified monocrystaline silicon reference cell (Newport, 91150V) with a fused silica window. AFM images were obtained using an Asylum Cypher AFM. UV–vis spectra were taken using a UV-2401PC model UV–Vis spectrophotometer. The EQE measurement system was composed of a 250WQuartz Tungsten Halogen lamp as the light source, a filter wheel, a chopper, a monochromator, a lock-in amplifier and a calibrated silicon photodetector. GIWAXS measurements were performed at the 8ID-E beamline at the Advanced Source (APS), Argonne National Laboratory, using X-rays with awavelength of $\lambda = 1.6868$ Å and a beam size of 200 μm (horizontal) and 20 μm (vertical).

3.3 Conclusion

In this chapter, four electron deficient compounds were synthesized and investigated as electron acceptor in BHJ OPV cells. Detailed studies revealed that the **αPPID** and **αPBDT** exhibit planarity in the PDI core which benefits the close π-π stacking. The absorption spectra **αPPID** and **αPBDT** showed the strong tendency to form aggregate due to the strong intermolecular π-π interaction, which persists in blended films, leading to relatively high electron mobility. The inverted BHJ devices employing PBT7-Th as the donor and αPDI-based compounds as acceptor demonstrate superior photovoltaic performance than that using βPDI-based derivative as acceptor; an enhancement of 39 %

was observed. The higher PCE of **αPPID** and **αPBDT** are mainly ascribed to their higher SCLC mobility and the more efficient charge separation at interfaces with **PBT7-Th**. The results suggest that α-substituted PDI derivatives are indeed promising electron acceptors and further exploration is main theme of next chapter.

3.4 References

(1) Facchetti, A. *Materials Today* **2013**, *16*, 123-132.

(2) Lin, Y.; Zhan, X. *Materials Horizons* **2014**, *1*, 470.

(3) Zhou, Y.; Kurosawa, T.; Ma, W.; Guo, Y.; Fang, L.; Vandewal, K.; Diao, Y.; Wang, C.; Yan, Q.; Reinspach, J.; Mei, J.; Appleton, A. L.; Koleilat, G. I.; Gao, Y.; Mannsfeld, S. C.; Salleo, A.; Ade, H.; Zhao, D.; Bao, Z. *Advanced materials* **2014**, *26*, 3767-3772.

(4) Wurthner, F.; Saha-Moller, C. R.; Fimmel, B.; Ogi, S.; Leowanawat, P.; Schmidt, D. *Chem Rev* **2015**.

(5) Zhao, J.; Li, Y.; Lin, H.; Liu, Y.; Jiang, K.; Mu, C.; Ma, T.; Lin Lai, J. Y.; Hu, H.; Yu, D.; Yan, H. *Energy Environ. Sci.* **2015**, *8*, 520-525.

(6) Liu, Y.; Lai, J. Y. L.; Chen, S.; Li, Y.; Jiang, K.; Zhao, J.; Li, Z.; Hu, H.; Ma, T.; Lin, H.; Liu, J.; Zhang, J.; Huang, F.; Yu, D.; Yan, H. *J. Mater. Chem. A* **2015**, *3*, 13632-13636.

(7) Rajaram, S.; Shivanna, R.; Kandappa, S. K.; Narayan, K. S. *The Journal of Physical Chemistry Letters* **2012**, *3*, 2405-2408.

(8) Jiang, W.; Ye, L.; Li, X.; Xiao, C.; Tan, F.; Zhao, W.; Hou, J.; Wang, Z. *Chemical communications* **2014**, *50*, 1024-1026.

(9) Shivanna, R.; Shoaee, S.; Dimitrov, S.; Kandappa, S. K.; Rajaram, S.; Durrant, J. R.; Narayan, K. S. *Energy Environ. Sci.* **2014**, *7*, 435-441.

(10) Zang, Y.; Li, C. Z.; Chueh, C. C.; Williams, S. T.; Jiang, W.; Wang, Z. H.; Yu, J. S.; Jen, A. K. *Advanced materials* **2014**, *26*, 5708-5714.

(11) Zhong, Y.; Trinh, M. T.; Chen, R.; Wang, W.; Khlyabich, P. P.; Kumar, B.; Xu, Q.; Nam, C. Y.; Sfeir, M. Y.; Black, C.; Steigerwald, M. L.; Loo, Y. L.; Xiao, S.; Ng, F.; Zhu, X. Y.; Nuckolls, C. *Journal of the American Chemical Society* **2014**, *136*, 15215-15221.

(12) Sun, D.; Meng, D.; Cai, Y.; Fan, B.; Li, Y.; Jiang, W.; Huo, L.; Sun, Y.; Wang, Z. *J Am Chem Soc* **2015**, *137*, 11156-11162.

(13) Yan, Q.; Zhou, Y.; Zheng, Y.-Q.; Pei, J.; Zhao, D. *Chemical Science* **2013**, *4*, 4389.

(14) Zhang, X.; Zhan, C.; Yao, J. *Chemistry of Materials* **2015**, *27*, 166-173.

(15) Singh, R.; Aluicio-Sarduy, E.; Kan, Z.; Ye, T.; MacKenzie, R. C. I.; Keivanidis, P. E. *Journal of Materials Chemistry A* **2014**, *2*, 14348.

(16) Huang, C.; Barlow, S.; Marder, S. R. *J Org Chem* **2011**, *76*, 2386-2407.

(17) Oh, J. H.; Liu, S.; Bao, Z.; Schmidt, R. d.; Würthner, F. *Applied Physics Letters* **2007**, *91*, 212107.

(18) Schmidt, R.; Oh, J. H.; Sun, Y. S.; Deppisch, M.; Krause, A. M.; Radacki, K.; Braunschweig, H.; Konemann, M.; Erk, P.; Bao, Z.; Wurthner, F. *J Am Chem Soc* **2009**, *131*, 6215-6228.

(19) Gsanger, M.; Oh, J. H.; Konemann, M.; Hoffken, H. W.; Krause, A. M.; Bao, Z.; Wurthner, F. *Angew Chem Int Ed Engl* **2010**, *49*, 740-743.

(20) Teraoka, T.; Hiroto, S.; Shinokubo, H. *Org Lett* **2011**, *13*, 2532-2535.

(21) Nakazono, S.; Imazaki, Y.; Yoo, H.; Yang, J.; Sasamori, T.; Tokitoh, N.; Cedric, T.; Kageyama, H.; Kim, D.; Shinokubo, H.; Osuka, A. *Chemistry* **2009**, *15*, 7530-7533.

(22) Nakazono, S.; Easwaramoorthi, S.; Kim, D.; Shinokubo, H.; Osuka, A. *Org Lett* **2009**, *11*, 5426-5429.

(23) Battagliarin, G.; Li, C.; Enkelmann, V.; Mullen, K. *Org Lett* **2011**, *13*, 3012-3015.

(24) Hartnett, P. E.; Timalsina, A.; Matte, H. S. S. R.; Zhou, N.; Guo, X.; Zhao, W.; Facchetti, A.; Chang, R. P. H.; Hersam, M. C.; Wasielewski, M. R.; Marks, T. J. *J Am Chem Soc* **2014**, *136*, 16345-16356.

(25) Teraoka, T.; Hiroto, S.; Shinokubo, H. *Org Lett* **2011**, *13*, 2532-2535.

(26) Ahmed, E.; Ren, G.; Kim, F. S.; Hollenbeck, E. C.; Jenekhe, S. A. *Chem Mater* **2011**, *23*, 4563-4577.

(27) Zhang, X.; Lu, Z.; Ye, L.; Zhan, C.; Hou, J.; Zhang, S.; Jiang, B.; Zhao, Y.; Huang, J.; Zhang, S.; Liu, Y.; Shi, Q.; Liu, Y.; Yao, J. *Adv Mater* **2013**, *25*, 5791-+.

(28) Jung, I. H.; Lo, W.-Y.; Jang, J.; Chen, W.; Zhao, D.; Landry, E. S.; Lu, L.; Talapin, D. V.; Yu, L. *Chemistry of Materials* **2014**, *26*, 3450-3459.

(29) Zou, L.; Wang, X. Y.; Zhang, X. X.; Dai, Y. Z.; Wu, Y. D.; Wang, J. Y.; Pei, J. *Chemical communications* **2015**, *51*, 12585-12588.

(30) Zhao, Z.; Zhang, F.; Zhang, X.; Yang, X.; Li, H.; Gao, X.; Di, C.-a.; Zhu, D. *Macromolecules* **2013**, *46*, 7705-7714.

(31) Dennler, G.; Scharber, M. C.; Brabec, C. J. *Advanced Materials* **2009**, *21*, 1323-1338.

(32) Ford, W. E.; Kamat, P. V. *The Journal of Physical Chemistry* **1987**, *91*, 6373-6380.

(33) Gómez, R.; Veldman, D.; Blanco, R.; Seoane, C.; Segura, J. L.; Janssen, R. A. J. *Macromolecules* **2007**, *40*, 2760-2772.

(34) Ramanan, C.; Kim, C. H.; Marks, T. J.; Wasielewski, M. R. *The Journal of Physical Chemistry C* **2014**, *118*, 16941-16950.

(35) Zhou, Y.; Ding, L.; Shi, K.; Dai, Y. Z.; Ai, N.; Wang, J.; Pei, J. *Advanced materials* **2012**, *24*, 957-961.

(36) Chen, Z.; Stepanenko, V.; Dehm, V.; Prins, P.; Siebbeles, L. D.; Seibt, J.; Marquetand, P.; Engel, V.; Wurthner, F. *Chemistry* **2007**, *13*, 436-449.

(37) Giaimo, J. M.; Lockard, J. V.; Sinks, L. E.; Scott, A. M.; Wilson, T. M.; Wasielewski, M. R. *J Phys Chem A* **2008**, *112*, 2322-2330.

(38) Gong, X.; Tong, M.; Brunetti, F. G.; Seo, J.; Sun, Y.; Moses, D.; Wudl, F.; Heeger, A. J. *Advanced materials* **2011**, *23*, 2272-2277.

(39) Liu, Y.; Zhao, J.; Li, Z.; Mu, C.; Ma, W.; Hu, H.; Jiang, K.; Lin, H.; Ade, H.; Yan, H. *Nat Commun* **2014**, *5*, 5293.

(40) Guo, X.; Zhou, N.; Lou, S. J.; Smith, J.; Tice, D. B.; Hennek, J. W.; Ortiz, R. P.; Navarrete, J. T. L.; Li, S.; Strzalka, J.; Chen, L. X.; Chang, R. P. H.; Facchetti, A.; Marks, T. J. *Nature Photonics* **2013**, *7*, 825-833.

(41) Lu, R.-Q.; Zheng, Y.-Q.; Zhou, Y.-N.; Yan, X.-Y.; Lei, T.; Shi, K.; Zhou, Y.; Pei, J.; Zoppi, L.; Baldridge, K. K.; Siegel, J. S.; Cao, X.-Y. *J. Mater. Chem. A* **2014**, *2*, 20515-20519.

(42) Li, Z.; Lin, J. D. A.; Phan, H.; Sharenko, A.; Proctor, C. M.; Zalar, P.; Chen, Z.; Facchetti, A.; Nguyen, T.-Q. *Advanced Functional Materials* **2014**, *24*, 6989-6998.

(43) Koster, L. J. A.; Mihailetchi, V. D.; Xie, H.; Blom, P. W. M. *Applied Physics Letters* **2005**, *87*, 203502.

(44) Lu, L.; Xu, T.; Chen, W.; Landry, E. S.; Yu, L. *Nature Photonics* **2014**, *8*, 716-722.

Chapter 4 Bay-cyclized PDI-diPDI

4.1 Introduction

In the previous chapter, we demonstrated that by retaining planarity of PDI unit, PCE of PDI-containing small molecules can be enhanced. To reduce the distortion of PDI core, α-substitution of PDI is not the only choice. Since the distortion is a result of H-H repulsion between H on linker unit and β-H of PDI, annulation reaction to form fused aromatic ring will eliminate the repulsion as well.

This chapter describes the synthesis, characterization, electrochemical and photophysical properties, and photovoltaic performance of a new class of A-D-A fully conjugated ladder-type oligomers. These compounds were based on thienoacenes derivatives (D_n) as the donor linker and perylene-diimide (PDI) as the acceptor units. Meanwhile, ladder-type polymers or oligomers by themselves have been continuously investigated in the past few decades for their potential applications as organic electronic materials.[1-3] Different types of structures have been studied in this regards, ranging from all hydrocarbon polyacenes to systems containing heterocyclic aromatic rings.[4,5] Recently, several soluble polyacenes have been reported, but their stability and processibility are still an issue.[4] In this work, by introducing PDI units and proper solubilizing groups, some aforementioned issues can be addressed. Materials presented in this chapter are examples of a new class of materials that will open up a door for a series of new studies encompassing topics in linear and nonlinear optical properties, and solar cell applications.

4.2 Result and discussion

4.2.1 Design and synthesis

To stabilize the heteroacene compounds and extend the conjugation, a synthetic strategy as shown in Figure 4.1 was developed. The ladder type linkers were synthesized according to the procedures developed in our lab. [6,7] Non-fused ring molecules (**3r**, **5r** and **9r**) were obtained by Pd-mediated coupling reaction between Br-PDI$^{\beta}$ and distanylated linkers. The annulated compounds (**C3r**, **C5r**, **C9r**) are obtained in high yields by following the Scholl cyclodehydrogenation using ferric chloride. All the materials are soluble in common organic solvents such as CH_2Cl_2, $CHCl_3$, THF, and toluene. Thermogravimetric analysis (TGA) reveals that both non-fused ring and fused ring molecules are thermally stable up to 400 °C

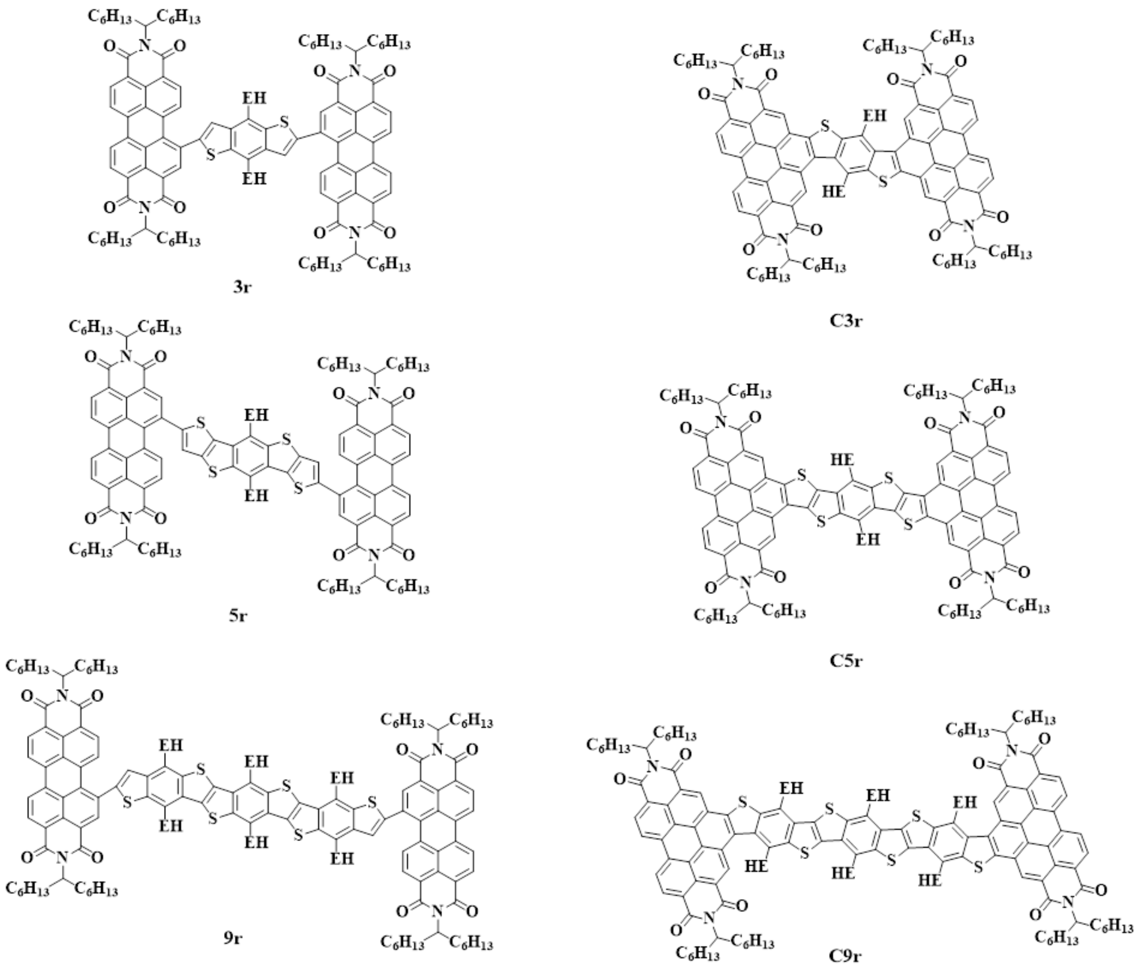

3r

C3r

5r

C5r

9r

C9r

Figure 4.1 Structures of cyclized di-PDI, 3r, 5r, 9r; and C3r, C5r and C9r. EH=ethylhexyl.

4.2.2 DFT calculation.

In order to gain more insight into the structural and electronic differences between non-fused and fused ring compounds, density functional theory (DFT) calculations were carried out by using the Gaussian package b3lyp/6-31g**. To facilitate the calculation, the heptylhexyl chains in PDI were replaced with a methyl group, while the ethylhexyl groups in heteroacenes were replaced by isobutyl to avoid missing the steric hindrance effect. A pictorial presentation of their structures of the six compounds are shown in Table

4-2, respectively, and the energy levels are summarized in Table 4-1. All the non-fused compounds showed similar twisted structures, with a torsion angle of 58.1°, 49.5 °, 66.4 °, respectively. The compound **5r** shows smallest dihedral angle due to least steric hindrance among the non-fused compounds. The fused ring compounds **C3r** and **C9r** show twisted structures because the strong steric hindrance between the alkyl chain in heteroacenes and PDI core, while the **C5r** shows a high coplanarity after cyclization with a dihedral angle only 2.0° Table 4-1.

Table 4-1 HOMO/LUMO energies, band gaps, fluorescence quantum yields and dipole moments of conjugated materials.

	HOMO (eV)	LUMO (eV)	Band gap (opt[a]/cv[b]/cal[c])	Q.Y. (%)	Dihedral[c]
3r	-5.82	-3.87	1.82/1.95/2.19	0.23	58.1^o
5r	-5.68	-3.87	1.72/1.81/1.94	0.17	49.5^o
9r	-5.44	-3.87	1.64/1.57/1.68	0.35	66.4^o
C3r	-5.90	-3.84	2.03/2.06/2.48	13.5	23.9^o
C5r	-5.69	-3.82	1.86/1.87/2.22	5.0	2.0^o
C9r	-5.51	-3.78	1.77/1.73/2.02	0.17	28.6^o

[a] Based on the absorption spectral data; [b] Based on redox potentials; [c] Dihedral angles between the PDI plane and adjacent BDT based on DFT calculations; [d] $\Delta\mu_{ge}$ was determined by accounting for the changes of the dipole along each coordinate axis.

3r	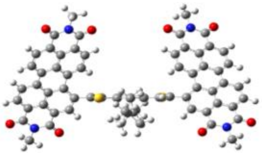	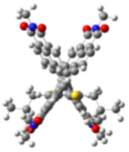
C3r	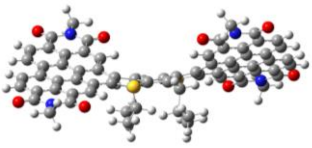	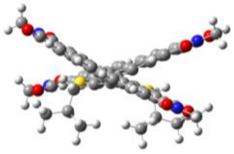
5r	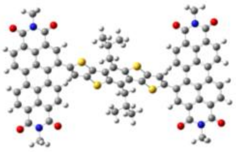	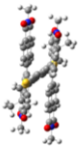
C5r	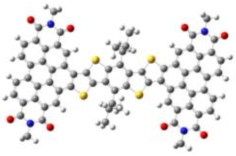	
9r	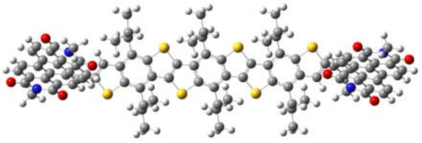	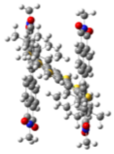
C9r	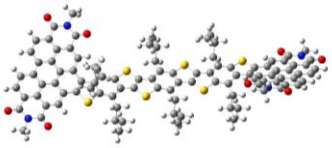	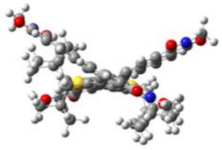

Table 4-2 Optimized geometry of A-D-A series molecules at DFT B3LYP/6-31G

4.2.3 Optical properties.

The steady-state absorption spectra of the compounds synthesized were recorded in chloroform solutions. The absorption spectra of non-fused ring series are shown in Figure 4.2a and those of the fused ring series are shown in Figure 4.2b. The steady state absorption spectrum for both the fused rings series and non-fused ring series showed that the BDT-DPI systems retains many of the localized absorption peaks observed in BDT and PDI. [6,7] For non-fused compounds, the plane of thienoacene moieties are twisted with the perylene ring due to the steric hindrance, which limited the π-electron delocalization interactions. The BDT unit acts as the electron donor in these compounds. Red shifts were observed for the peaks at 300-450 nm of the non-fused systems (Figure 4.2). As expected, the molar extinction coefficient increased as the conjugation of the BDT derivative units is increased. The absorption peaks from 450-500 nm with characteristic vibronic fine structures were assigned to the PDI[2], in which the BDT has weak or no absorption. The absorption peak at 600-650 nm range was attributed to the charge transfer state between BDT and PDI units. The spectra of the fused ring series exhibit a red-shift compared the non-fused ring compounds at the 300-500 nm range. Two shoulder peaks were shown in **C3r** molecule, while the vibronic fine structures disappeared for **C9r** molecule. Interestingly, **C3r** and **C5r** show a new peak at 450 nm (the peak of **C9r** is over-lapped in thienoacene region). This is because more symmetry allowed transition occurs after the cyclization.[8] The absorption at 500-550 nm due to the PDI is much weaker compared to the non-fused system and the characteristic vibronic fine structures disappear. The **C5r** with a high coplanarity extends the perylene core along the short molecular axis, which leads to blue-shifted absorption.[9] The new absorption bands that observed in the 600-650 nm range exhibit higher intensity than the non-fused system, indicating a stronger intramolecular charge transfer in fused ring compounds. Additionally, the onset peaks are blue-shifted when the non-fused ring molecules and their fused ring molecules analogs are compared. So the optical band gap becomes broader after cyclization (Table 4-1).

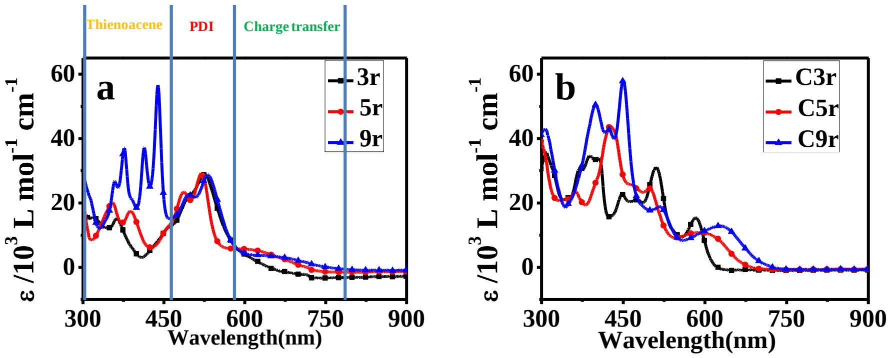

Figure 4.2 (a) Solution absorption of non-fused ring compounds; (b) Solution absorption of fused ring compounds.

The emission spectra of **3r** and **9r** are shown at Figure 4.3a. The emission spectra of the **C3r** and **C9r** are shown at Figure 4.3b. The spectra for the **5r** and **C5r** are shown in Figure 4.3c. The three non-fused molecules displayed a very weak emission with quantum yields less than 1% (Table 4-1). [10] The significant fluorescence quenching come from the following two reasons: (1) Electron transfer from BDT core to perylene core may quench the fluorescence of the molecule because of incompletely conjugated aromatic system; (2) Strong molecular vibration of non-fused ring compounds may consume the most energy and make it nonfluorescent.[11] The emission spectrum of the non-fused BDT-PDI series shows two emission peaks in the 450-550 nm that are typical for BDT derivatives (450-500 nm) and PDI (550 nm) units,[12] and another weak emission peak towards the 600-700 nm region. In addition, the **5r** shows another strong emission peak towards the high 600-700 nm region. This should be attributed to charge transfer state of the **5r**.[13]

A completely different emissive behavior is observed for the fused rings series. The fused rings BDT-PDI compounds show a higher quantum yields than the non-fused analogs. This can be explained by the rigid structure nature of the fused system. This rigid nature may promote radiative relaxation pathways of the excited state. Both the **C3r** and **C9r** showed emission peaks between 450 nm to 550 nm (Figure 4.3b), while **C5r** showed very weak emission in that region (Figure 4.3c). The emission peak at 550 nm in **C3r** and **C9r** is characteristic of the PDI unit. The emission observed from the PDI unit can be attribute to the twisted structures of the **C3r** and **C9r**. This same twisted conformation may explain the Q.Y. values of the **C3r** and **C9r** compounds.

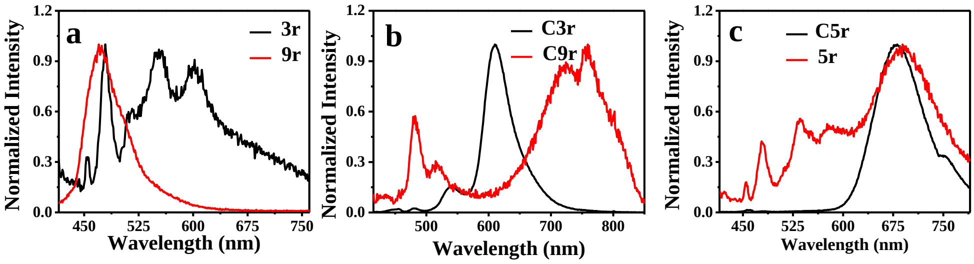

Figure 4.3 (a) Emission spectra of 3r and 9r; (b) Emission spectra of C3r and C9r; (c) Emission spectra of 5r and C5r. All of the spectra were calculated at 400 nm excitation wavelength.

4.2.4 Electrical properties and energy levels.

Both the HOMO and LUMO, energy levels for different ladder-type molecules were determined by cyclic voltammetry (CV) (Figure 4.4), as listed in Table 4-1. All the non-fused ring molecules showed the identical LUMO energy level (-3.87 eV), while the HOMO energy levels slightly increase as the donor length increase because the LUMO energy level was localized on the PDI moiety while the HOMO energy level was localized on the heteroacene moieties before cyclization. However, fused ring compounds with planar aromatic core show a slightly higher LUMO energy, lower HOMO energy, and broader band gap relative to non-fused ring compounds. All these trends are in agreement with those obtained from theoretical calculation and optical measurements.

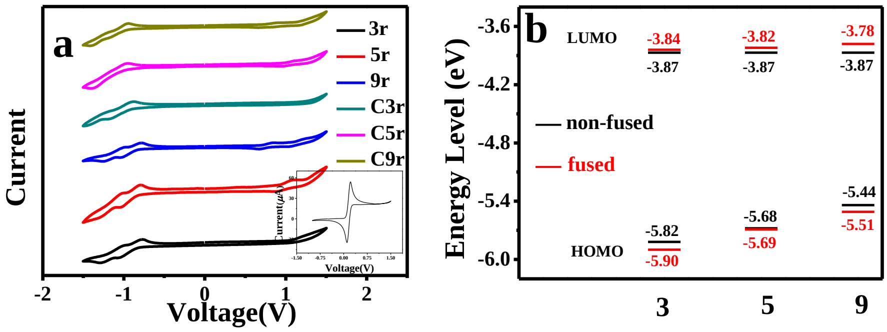

Figure 4.4 (a) Cyclic voltammograms of ladder molecules in $CHCl_3$ (1.0×10^{-3} M) with Pt as the working and counter electrodes and Ag/AgCl electrode as the reference electrode and Fc/ Fc^{2+} was used as inner reference, n-Bu_4NPF_6 (0.1 M) as supporting electrolyte; (b) Measured energy levels of ladder molecules based on CV data.

4.2.5 Photovoltaic properties

Photovoltaic effects of all six novel compounds were evaluated via inverted thin film solar cell devices. The energy levels of the six compounds are suited as electron acceptor; all match well with that of **PTB7-Th**, an efficient donor polymers for bulk heterojunction organic solar cells with enough energy offset for charge separation. Device structure is ITO/ZnO/Active Layer/MoO_3/Ag. **PTB7-Th** was employed as donor polymer with donor/acceptor ratio of 1:2. Active layer thickness was controlled at about 80 nm. Preliminary device results are listed in Table 4-3 and their J-V curves were shown in Figure 4.5. In general, all the fused ring materials exhibit better photovoltaic performance with higher V_{oc} and *FF* compared to their non-fused counterparts.

Table 4-3 Solar cell efficiencies of PTB7-Th/conjugated molecules[a].

	J_{sc}/mA/cm^2	V_{oc}/V	FF(%)	Eff(%)	μ_h (cm^2/Vs)	μ_e (cm^2/Vs)
3r	8.96	0.87	0.42	3.26±0.02	4.43×10^{-4}	5.00×10^{-5}
C3r	9.31	0.94	0.43	3.75±0.07	3.08×10^{-4}	$1.43\text{x}10^{-5}$
5r	8.39	0.89	0.40	2.97±0.03	2.67×10^{-4}	3.46×10^{-5}
C5r	12.50	0.95	0.47	5.59±0.10 (6.06)[b]	3.55×10^{-4}	6.21×10^{-5}
9r	5.38	0.88	0.39	1.85±0.12	2.91×10^{-4}	2.03×10^{-5}
C9r	8.89	0.98	0.43	3.69±0.01	2.16×10^{-4}	$1.22*10^{-5}$

[a] Results are averaged over 10 devices, [b] With 0.5% DIO as an additive

It was found that fused ring acceptor materials exhibit enhanced V_{oc} value. Cyclization of **3r** to **C3r** increased V_{oc} from 0.87 V to 0.94 V, **5r** to **C5r** from 0.89 V to 0.95 V, **9r** to **C9r** from 0.88 V to 0.98 V. This enhancement of V_{oc} correlates with the band gap increase in the acceptor molecules (Table 4-3). The LUMO energy levels were dominated by PDI moiety and HOMO by BDT ladder unit for the non-fused ring compounds, so they show almost the same LUMO energy and similar V_{oc} with the molecular length increase (Figure 4.5). For the fused ring molecules, the HOMO energy levels are reduced slightly due to electron withdrawing effect of the PDI and LUMO energy level increased due to electron donating effect of BDT moiety. Thus, both the energy levels and V_{oc} of the fused ring compounds increase linearly with the length of the molecular structures (Figure 4.5).

A dilemma of material design in BHJ solar cells is that, to achieve high V_{oc} with a certain donor polymer, acceptor with higher LUMO would be desirable for high V_{oc} value, however at the same time, higher LUMO of acceptor also implies smaller difference between LUMO of donor and LUMO of acceptor, which will reduce driving force for charge separation, and is detrimental to J_{sc} value. The system described here shows that devices benefits from obvious V_{oc} enhancement without sacrificing their J_{sc}. The **C3r** show almost same J_{sc} with **3r**, and **C5r** and **C9r** even have much higher J_{sc} than that of **5r** and **9r**. **C9r** device has J_{sc} of 8.9 mA/cm^2 which is 35% higher than J_{sc} of **9r** device (5.4 mA/cm^2). The **C5r** device showed J_{sc} of 12.5 mA/cm^2, which is of 50% enhancement compared to 8.4 mA/cm^2 of **5r** device. Overall, all fused ring acceptors show higher photo conversion efficiency over their non-fused ring counterparts. Without any processing additive, highest efficiency 5.6% was achieved by **C5r** device which has outstanding J_{sc} and *FF* compared to others. PCE as high as 6.1% was achieved by introducing 0.5% DIO as processing additive of **C5r** device, implying **C5r** has great potential as efficient[6,76,7] electron acceptor after more careful optimization.

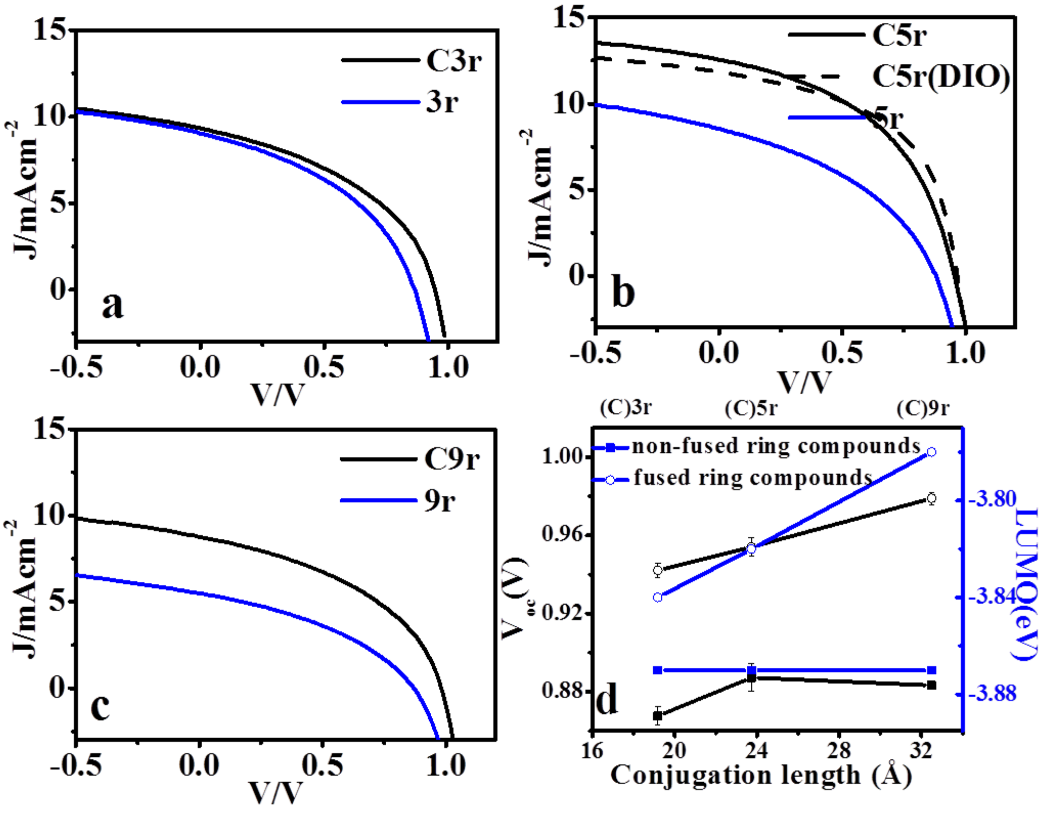

Figure 4.5 J-V curves of PTB7-Th/conjugated molecules devices. a) PTB7-Th/3r and PTB7-Th/C3r; b) PTB7-Th/5r, PTB7-Th/C5r and PTB7-Th/C5r-DIO; c) PTB7-Th/9r and PTB7-Th/C9r; d) Open circuit voltage (V_{OC}) versus and lowest unoccupied molecular orbital energy (E_{LUMO}) versus the backbone conjugation length of a series of A-D-A molecules.

To understand the reason of J_{sc} enhancement, we measured external quantum efficiencies (EQE) of the devices (Figure 4.6). The **C3r** and **3r** devices show overall similar EQE spectrum and almost identical J_{sc} value. For **5r** and **C5r**, **C5r** shows much higher quantum efficiency, with **PTB7-Th** reaching 60% at 600-800 nm. The high quantum efficiency of 50% between 400-500 nm corresponds to the strong absorption peak of **C5r**, indicating an efficient hole transfer from acceptor to donor. For **9r** and **C9r**, although both acceptor materials show high absorbance between 400 to 500 nm, their quantum efficiency are lower than 40%, meaning they are inefficient in generating charge carriers.

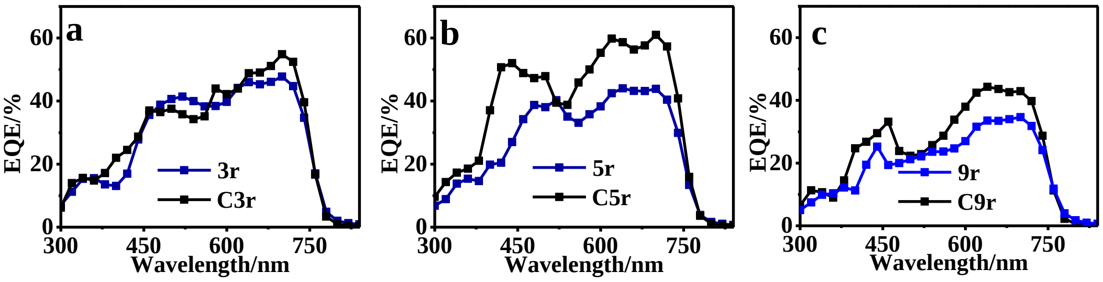

Figure 4.6 External quantum efficiency (EQE) spectra of PTB7-Th/conjugated molecules devices. a) PTB7-Th/3r and PTB7-Th/C3r; b) PTB7-Th/5r and PTB7-Th/C5r; c) PTB7-Th/9r and PTB7-Th/C9r.

Charge carrier mobility is evaluated by SCLC method. Hole-only devices are fabricated with the structure of ITO/PEDOT/Active layer/MoO_3/Ag, and electron-only devices are fabricated with the structure of ITO/ZnO/Active layer/Ca/Al. Mobility results are summarized in Table 4-3 and the mobility curves are shown in Figure 4.7. Hole mobilities of blend devices are similar and are of magnitude of 10^{-4} $cm^2V^{-1}s^{-1}$. Electron mobility differs greatly between different acceptors. The best performing device, **C5r**, show highest electron mobility of 6.21×10^{-5} $cm^2V^{-1}s^{-1}$. With hole mobility of 3.55×10^{-4} $cm^2V^{-1}s^{-1}$, the hole to electron mobility ratio of **C5r** blend device is only 5.7. This fairly balanced mobility helps to explain the best J_{sc} and *FF* value of **C5r** device among the six acceptors. This high electron mobility of **C5r** blend is clearly due to the highly planarity of the molecular structure of **C5r**.

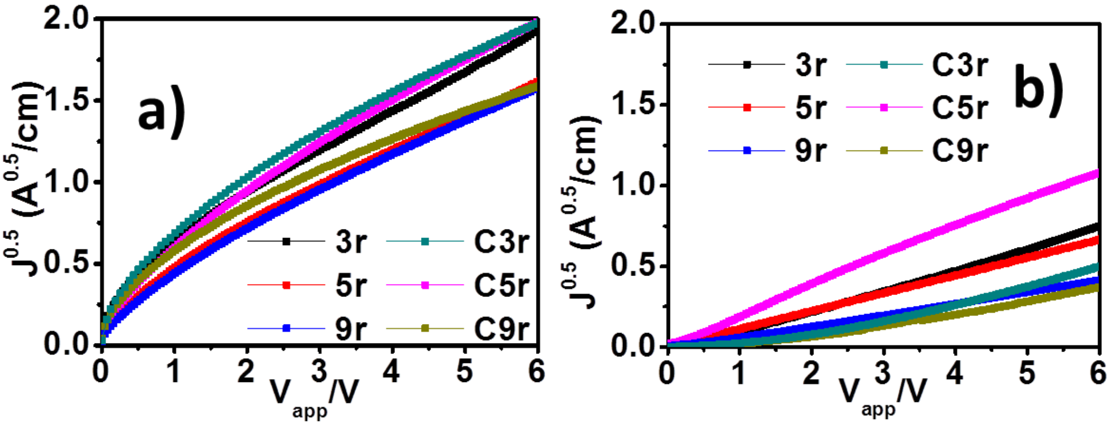

Figure 4.7 Hole mobility (a) and electron mobility (b) curves of PTB7-Th/conjugate acceptor blend films.

The grazing-incident wide-angle X-ray scattering (GIWAXS) measurement was employed to investigate the crystallinity of the neat and blend films. For the pure acceptor materials, diffraction peaks are Gaussian-fitted and peak q values are listed in Table 4-4. As shown in 2D GIWAXS figures (Figure 4.8), acceptor diffractions all have ring-like features, indicating they do not have a preferred orientation. By carefully comparing the q values of diffraction peaks, the q-value of the fused ring compounds in π-π stacking region are all larger than those of the non-fused ring compounds, which means molecules are more closely packed. This result is expected from our DFT calculations that fused molecules have smaller dihedral angle. Especially for **C5r**, which has a perfectly flat structure as predicted by DFT and supported by NMR spectra, has the shortest intermolecular distance (4 Å). The 2D GIWAXS spectra of blend films were also recorded in Figure 4.10 and their linecuts in Figure 4.11. The π-π signals in q_z direction were all stronger than those in q_r direction indicating that the molecules preferred to lay down on the substrates. In addition, all q_z peaks of π-π at 1.6, which resembles stacking distance of **PTB7-Th**. In addition, in-plane π-π stacking distances in blend films are all smaller than that of pure acceptors with the help of donor-acceptor interaction.

The active blend films of these devices exhibit similar morphologies, as characterized by atomic force microscopy (AFM) (see Figure 4.12). AFM images (with dimensions of 2 μm × 2 μm) show that the device blends have similar features and comparatively similar smoothness. The root-mean-square (RMS) roughness values of all blend films are around 1 nm. AFM studies suggest that the solar cell efficiency difference between the six compounds is not due to blend morphology.

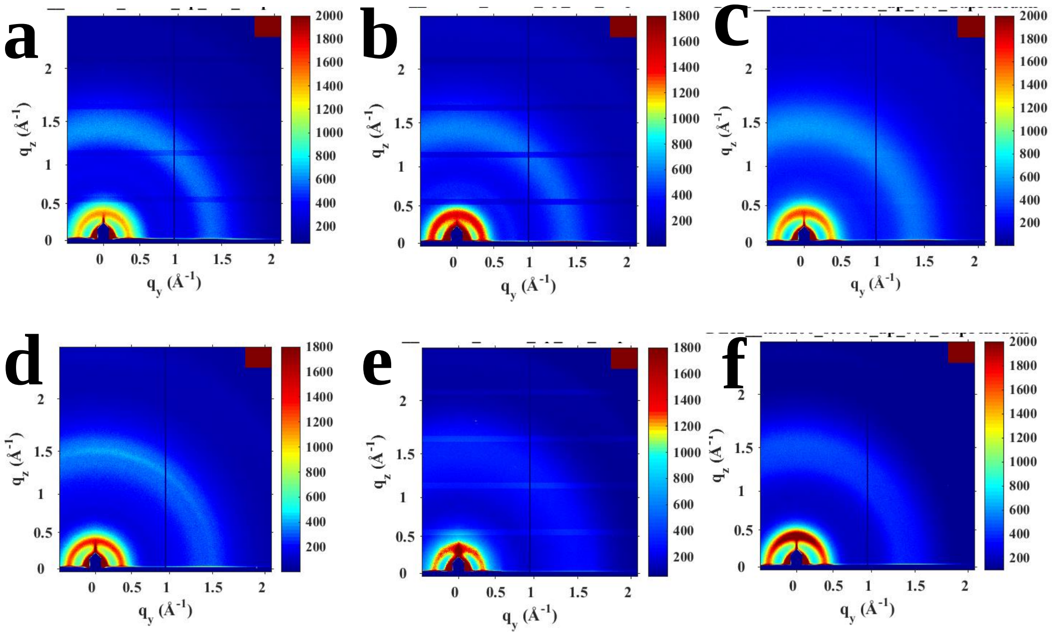

Figure 4.8 2D GIWAXS patterns of pristine acceptor films on ZnO-modified Si substrates. (a) 3r, (b) 5r, (c) 9r, (d) C3r, (e) C5r, (f) C9r.

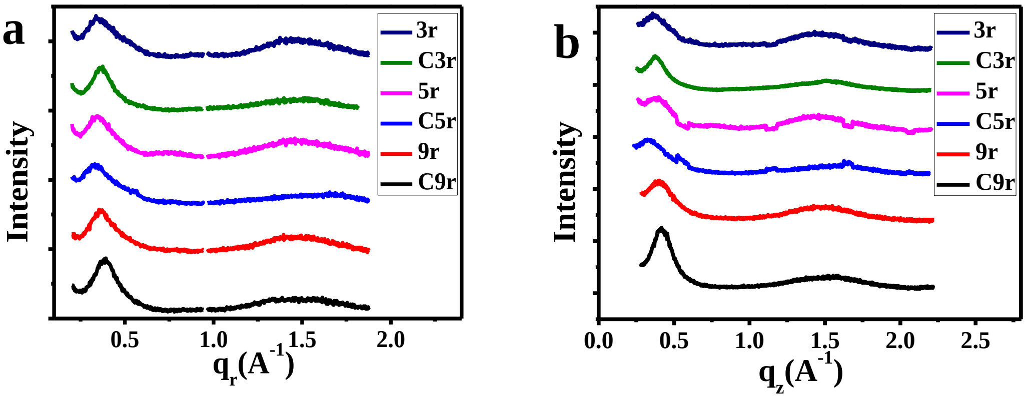

Figure 4.9 In-plane (a)/out-of-plane (b) line cuts of pristine acceptor films.

Table 4-4 Neat acceptor line cut peaks

	q_r		q_z	
q	Lamellar (Å^{-1})	π-π (Å^{-1})	Lamellar (Å^{-1})	π-π (Å^{-1})
3r	0.35	1.48	0.34	1.47
C3r	0.36	1.50	0.37	1.50
5r	0.35	1.46	0.37	1.45
C5r	0.33	1.56	0.33	1.56
9r	0.36	1.47	0.40	1.47
C9r	0.39	1.48	0.42	1.51

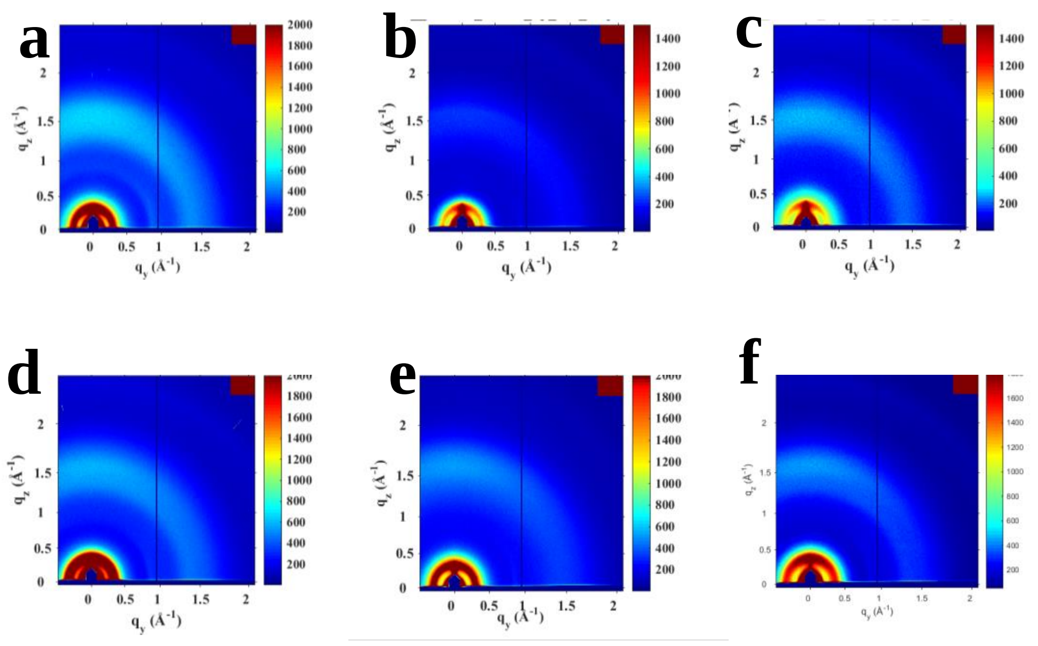

Figure 4.10 2D GIWAXS patterns of blend films on ZnO-modified Si substrates. (a) 3r, (b) 5r, (c) 9r, (d) C3r, (e) C5r, (f) C9r.

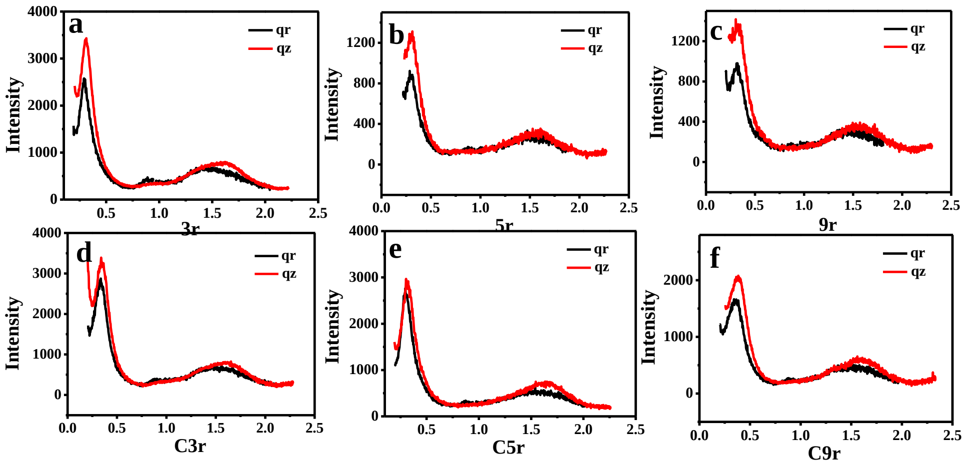

Figure 4.11 Line cuts of blend films (a) 3r, (b) 5r, (c) 9r, (d) C3r, (e) C5r, (f) C9r.

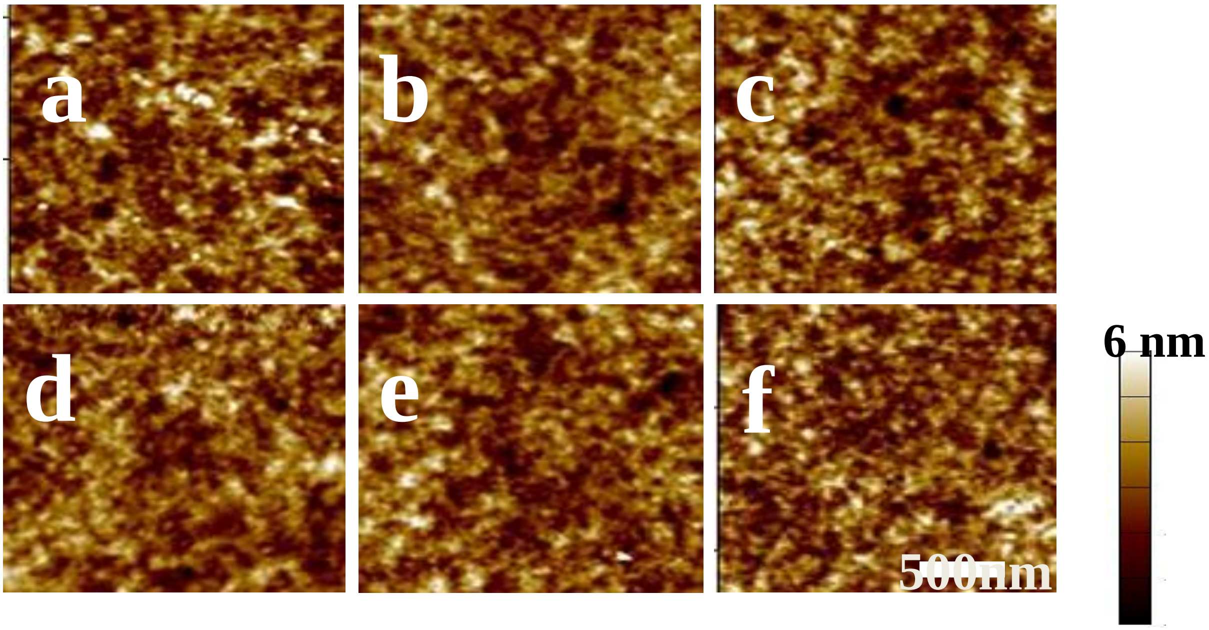

Figure 4.12 Atomic force microscopy (AFM) of blend films 3r (a), C3r (b), 5r (c), C5r (d), 9r (e) and C9r(f)

4.2.6 Experimental section

Synthesis of materials:

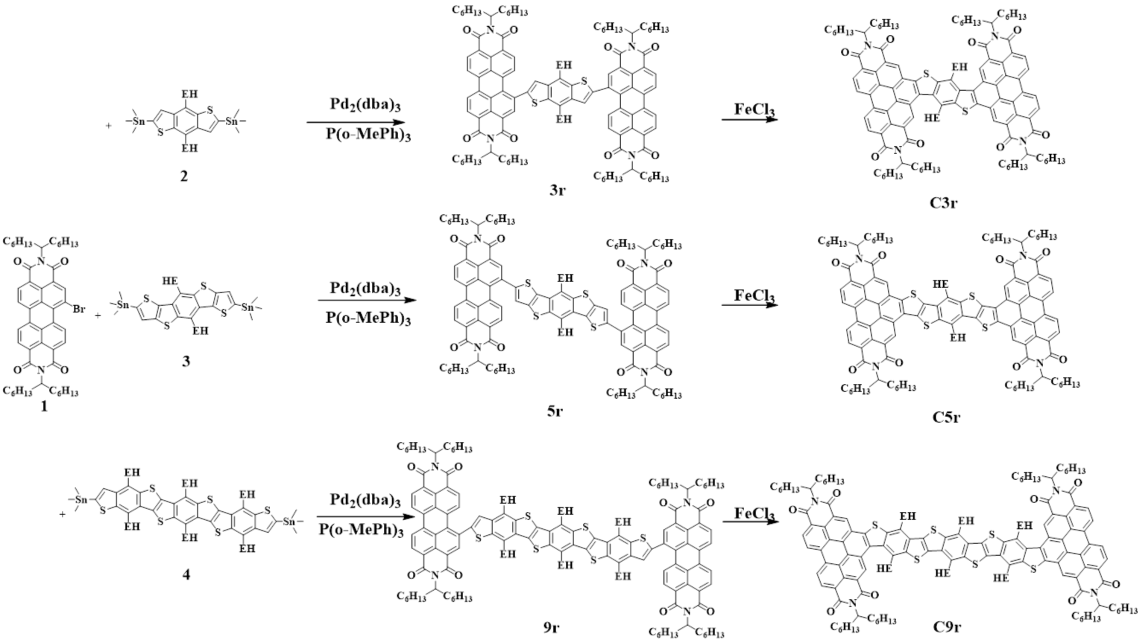

Figure 4.13 A-D-A molecules and their fused ring-expanded compounds.

Synthesis of Compound **3r**: To a round-bottom flask equipped with a condenser was added **1** (530 mg, 0.64 mmol), **2** (215 mg, 0.29 mmol), $Pd_2(dba)_3$ (53 mg, 0.06 mmol) and $P(o\text{-}MePh)_3$ (85 mg, 0.24). The system was evacuated and refilled with N_2 three times, then charged with toluene (50 ml). The reaction mixture was refluxed under N_2 for 16 hours. After cooling to room temperature, the reaction mixture was concentrated under reduced pressure. The residue was purified by column chromatography with hexane and CH_2Cl_2 (1:1, v/v) as the eluent. Compound **3r** was obtained as a red solid (422 mg, 75.8% yield). ^1H NMR ($CDCl_3$ ppm): δ 8.54 (d, *J* = 16, 2H), 8.66 (m, 8H), 8.35 (s, 2H), 8.21 (d, *J* = 19.5, 2H), 7.68 (s, 2H), 5.20 (m, 4H), 3.12 (s, 2H), 3.02 (s, 2H), 2.28-2.02 (m, 8H), 1.89-1.81 (m, 10H), 1.24-1.21 (m, 78H), 0.83 (m, 32H), 0.77 (s, 6H). ^{13}C NMR ($CDCl_3$, ppm): δ 164.7, 164.3, 163.7, 163.5, 144.4, 139.5, 139.01, 139.4, 137.9, 137.8, 136.9, 136.1, 135.0, 134.2, 131.8, 131.5, 131.1, 130.8, 130.1, 130.0, 129.2, 129.1, 128.1, 127.5, 124.1, 123.7, 123.4, 123.0, 122.7, 122.2, 122.0, 54.9, 54.7, 40.3, 38.4, 32.4, 31.8, 31.8, 29.3, 29.2, 28.8, 27.0, 26.9, 23.0, 22.6, 22.6, 14.1, 14.1, 14.0, 11.1. MS (m/z, MALDI-TOF), calcd for $C_{126}H_{158}N_4O_8S_2$, 1919.2, found, 1920.8, Elemental analysis: calcd. for $C_{126}H_{158}N_4O_8S_2$: C, 78.79; H, 8.29, N, 2.92, S, 3.34; found: C, 78.66; H, 8.38, N, 2.97, S, 3.14.

Synthesis of Compound **5r**: To a round-bottom flask equipped with a condenser was added **1** (462 mg, 0.55 mmol), **3** (215 mg, 0.25 mmol), $Pd_2(dba)_3$ (23 mg, 0.03 mmol) and $P(o\text{-}MePh)_3$ (31 mg, 0.09). The system was evacuated and refilled with N_2 three times, then charged with toluene (40 ml). The reaction mixture was refluxed under N_2 for 16 hours. After cooling to room temperature, the reaction mixture was concentrated under reduced pressure. The residue was purified by column chromatography with hexane and CH_2Cl_2 (1:1, v/v) as the eluent. Compound **5r** was obtained as a red solid (403 mg, 78.4% yield). ^1H NMR ($CDCl_3$ ppm): δ 8.84 (d, *J* = 18, 2H), 8.60 (m, 8H), 8.25 (s, 2H), 8.13 (s, 2H), 7.60 (s, 2H), 5.23 (s, 2H), 5.12 (s, 2H), 2.95 (s, 4H), 2.30-2.18 (m, 8H), 1.99-1.90 (m, 10H), 1.25-1.21 (m, 78H), 0.84-0.81 (m, 32H), 0.69 (s, 6H). ^{13}C NMR ($CDCl_3$, ppm): δ 164.7, 164.5, 164.2, 163.6, 163.3, 163.1, 147.0, 141.8, 139.0, 137.1, 136.3, 135.1, 135.0, 134.1, 133.8, 133.1, 131.8, 131.5, 130.8, 130.1, 129.9, 129.1, 129.0, 128.7, 127.5, 124.1, 123.7, 123.4, 122.9, 122.7, 122.3, 119.9, 54.9, 54.7, 39.1, 39.0, 32.8, 32.4, 31.8, 31.8, 29.7, 29.2, 28.7, 27.0, 23.0 22.6, 22.6, 14.1, 14.0, 13.9, 11.2. MS (m/z, MALDI-TOF), calcd for $C_{130}H_{158}N_4O_8S_4$, 2031.1, found, 2032.8, Elemental analysis: calcd. for $C_{130}H_{158}N_4O_8S_4$: C, 76.81, H, 7.83, N, 2.76, S, 6.31; found: C, 77.00; H, 7.90, N, 2.80, S, 6.13.

Synthesis of Compound **9r**: To a round-bottom flask equipped with a condenser was added **1** (240 mg, 0.29 mmol), **4** (198 mg, 0.13 mmol), $Pd_2(dba)_3$ (12 mg, 0.01 mmol) and $P(o\text{-}MePh)_3$ (18 mg, 0.05). The system was evacuated and refilled with N_2 three times, then charged with toluene (40 ml). The reaction mixture was refluxed under N_2 for 16 hours. After cooling to room temperature, the reaction mixture was concentrated under reduced pressure. The residue was purified by column chromatography with hexane and CH_2Cl_2 (1:1, v/v) as the eluent. Compound **9r** was obtained as a red solid (323 mg, 91.7% yield). ^1H NMR ($CDCl_3$ ppm): δ 8.87 (d, *J* = 16, 2H), 8.76 (m, 8H), 8.29 (s, 2H), 8.14 (s, 2H), 7.73 (s, 2H), 5.23 (s, 2H), 5.16 (s, 2H), 3.43-3.22 (m, 12H), 2.30-2.20 (m, 12H), 2.04(s, 2H), 1.89-1.86 (m, 8H), 1.34-1.25 (m, 108H), 0.92-0.81 (m, 64H). ^{13}C NMR ($CDCl_3$, ppm): δ 164.7, 163.7, 144.0, 142.1, 141.5, 140.1, 137.6, 136.8, 136.1, 135.0, 134.0, 133.8, 132.3, 131.8, 130.6, 130.3, 129.9, 129.1, 128.8, 128.5, 128.1, 127.3, 123.7, 123.4, 122.9, 122.0, 54.9, 54.7, 40.1, 39.8, 39.4, 38.8, 37.9, 31.8, 29.2, 27.0, 23.2, 22.6, 22.6, 14.1, 14.1, 11.2, 11.0. MS (m/z, MALDI-TOF), calcd for $C_{174}H_{226}N_4O_8S_6$, 2691.6, found, 2693.3, Elemental analysis: calcd. for $C_{174}H_{226}N_4O_8S_6$: C, 77.57; H, 8.46, N, 2.08, S, 7.14; found: C, 77.72; H, 8.51, N, 2.09, S, 6.95.

Synthesis of Compound C**3r**: A solution of $FeCl_3$ (676 mg, 4.17 mmol) in 2 ml nitromethane was added dropwise to a stirred solution of compound **3r** (400 mg, 0.21

mmol) in 10 ml CH_2Cl_2. The reaction was stirred with argon. After stirring for 10 h at room temperature, 1 ml methanol was added to the solution. The solvent was evaporated under reduced pressure, and the crude product was filtered with silicone gel with a large amount of $CHCl_3$ to yield the solid product (367mg, 92%).^{1}H NMR (CD_2Cl_4, ppm, 353 K): δ 10.01 (s, 2H), 9.84 (s, 2H), 9.42 (d, *J* = 7.5, 4H), 9.13 (s, 4H), 5.95 (s, 4H), 4.11 (s, 4H), 2.38 (s, 8H), 2.01 (br, 10H), 1.45-1.14 (m, 78H), 0.93-0.72 (m, 32H), 0.42 (m, 6H). ^{13}C NMR ($CDCl_3$, ppm): δ 165.4, 164.1, 141.6, 140.1, 134.7, 133.7, 133.3, 131.9, 131.4, 129.3, 128.7, 127.7, 126.6, 125.7, 124.6, 124.4, 123.5, 122.9, 122.3, 122.0, 55.1, 39.6, 39.1, 32.6, 32.2, 31.8, 29.7, 29.3, 27.1, 22.6, 14.1, 10.8. MS (m/z, MALDI-TOF), calcd for $C_{126}H_{154}N_4O_8S_2$, 1915.1, found, 1916.7, Elemental analysis: calcd. for $C_{126}H_{154}N_4O_8S_2$: C, 78.95; H, 8.10, N, 2.92, S, 3.35; found: C, 78.65; H, 8.11, N, 2.95, S, 3.51.

Synthesis of Compound C**5r**: A solution of $FeCl_3$ (319 mg, 1.97 mmol) in 2 ml nitromethane was added dropwise to a stirred solution of compound **5r** (200 mg, 0.10 mmol) in 8 ml CH_2Cl_2. The reaction was stirred with argon. After stirring for 10 h at room temperature, 1 ml methanol was added to the solution. The solvent was evaporated under reduced pressure, and the crude product was filtered with silicone gel with a large amount of $CHCl_3$ to yield the solid product (180 mg, 90%).^{1}H NMR

(CD_2Cl_4 ppm, 353 K): δ 9.88 (s, 2H), 8.82-8,70 (br, 10H), 5.51 (s 2H), 5.52 (s 2H), 3.76 (s, 4H), 2.61-0.81 (m, 134H). ^{13}C NMR ($CDCl_3$, ppm): δ 164.6, 163.6, 142.6, 141.6, 134.2, 134.0, 131.7, 129.7, 129.1, 128.8, 128.7, 128.5, 128.0, 126.7, 125.8, 124.8, 124.4, 123.7, 123.2, 122.7, 122.2, 121.1, 55.7, 33.4, 32.4, 32.3, 32.2, 31.9, 30.3, 30.1, 29.7, 29.3, 29.1, 27.7, 27.2, 23.1, 23.0, 22.6, 14.4, 14.1. MS (m/z, MALDI-TOF), calcd for $C_{130}H_{154}N_4O_8S_4$, 2027.1, found, 2028.9, Elemental analysis: calcd. for $C_{130}H_{154}N_4O_8S_4$: C, 76.96, H, 7.65, N, 2.76, S, 6.32; found: C, 77.12; H, 7.73, N, 2.80, S, 6.46.

Synthesis of Compound C**9r**: A solution of $FeCl_3$ (240 mg, 1.48 mmol) in 2 ml nitromethane was added dropwise to a stirred solution of compound **9r** (200 mg, 0.07 mmol) in 8 ml CH_2Cl_2. The reaction was stirred with argon. After stirring for 10 h at room temperature, 1 ml methanol was added to the solution. The solvent was evaporated under reduced pressure, and the crude product was filtered with silicone gel with a large amount of $CHCl_3$ to yield the solid product (187 mg, 94%). ^{1}H NMR ($C_2D_4Cl_4$ ppm): δ 10.22 (br, 2H), 9.83 (s, 2H), 9.42 (s, 4H), 9.16 (s, 4H), 5.46 (s, 4H), 3.99 (br, 2H), 2.10 (br, 12H), 1.84 (br, 10H), 1.48-0.92 (m, 182H). ^{13}C NMR ($CDCl_3$, ppm): δ 165.5, 164.4, 131.9, 131.5, 129.2, 128.0, 127.6, 126.7, 124.6, 123.5, 122.5, 121.9, 55.0, 39.6, 39.4, 32.6, 32.2, 32.0, 31.9, 29.7, 29.3, 27.4, 27.1, 22.8, 22.7, 14.2, 14.1. MS (m/z, MALDI-TOF), calcd for $C_{174}H_{222}N_4O_8S_6$, 2687.5, found, 2688.6, Elemental analysis: calcd. for $C_{174}H_{222}N_4O_8S_6$: C, 77.69, H, 8.32, N, 2.08, S, 7.15; found: C, 76.67, H, 8.42, N, 2.05, S, 6.97.

Materials and Characterization Techniques are similar to what described in Chapter 3, except for that Ag is used for device counter electrode instead of Al.

4.3 Conclusion

A series of heteroacene based A-D-A conjugated molecules were designed and synthesized in order to study their structure-property relationship. All fused ring molecules show excellent solubility and air stability. Optical and electrochemical characterization of these ladder-type molecules suggested that there are energy transfer/intramolecular charge transfer states between donor and acceptor units, resulting in broadening in the optical and electrical bandgaps after the cyclization. Inverted BHJ devices were fabricated employing **PTB7-Th** as the donor and PDI-based compounds as the acceptor. Performance indicated that the **C5r** have the higher power conversion efficiency (PCE) among the six compounds (6.1%), which are mainly ascribed to its planarity, higher SCLC mobility, and the more-efficient charge separation at interfaces with **PTB7-Th**.

4.4 References

(1) Liu, J.; Osella, S.; Ma, J.; Berger, R.; Beljonne, D.; Schollmeyer, D.; Feng, X.; Müllen, K. *Journal of the American Chemical Society* **2016**, *138*, 8364-8367.

(2) Cai, Z.; Zhang, H.; Geng, H.; Liu, Z.; Yang, S.; Luo, H.; Jiang, L.; Peng, Q.; Zhang, G.; Chen, J.; Yi, Y.; Hu, W.; Zhang, D. *Chemistry – A European Journal* **2013**, *19*, 14573-14580.

(3) Bunz, U. H. F. *Accounts of Chemical Research* **2015**, *48*, 1676-1686.

(4) Stępień, M.; Gońka, E.; Żyła, M.; Sprutta, N. *Chemical Reviews* **2016**.

(5) Narita, A.; Wang, X.-Y.; Feng, X.; Mullen, K. *Chemical Society Reviews* **2015**, *44*, 6616-6643.

(6) Cai, Z.; Luo, H.; Qi, P.; Wang, J.; Zhang, G.; Liu, Z.; Zhang, D. *Macromolecules* **2014**, *47*, 2899-2906.

(7) Zheng, T.; Cai, Z.; Ho-Wu, R.; Yau, S. H.; Shaparov, V.; Goodson, T.; Yu, L. *Journal of the American Chemical Society* **2016**, *138*, 868-875.

(8) Zhong, Y.; Kumar, B.; Oh, S.; Trinh, M. T.; Wu, Y.; Elbert, K.; Li, P.; Zhu, X.; Xiao, S.; Ng, F.; Steigerwald, M. L.; Nuckolls, C. *Journal of the American Chemical Society* **2014**, *136*, 8122-8130.

(9) Yu, Y.; Li, Y.; Qin, Z.; Jiang, R.; Liu, H.; Li, Y. *Journal of Colloid and Interface Science* **2013**, *399*, 13-18.

(10) Kc, C. B.; Stranius, K.; D'Souza, P.; Subbaiyan, N. K.; Lemmetyinen, H.; Tkachenko, N. V.; D'Souza, F. *The Journal of Physical Chemistry C* **2013**, *117*, 763-773.

(11) Yuan, Z.; Xiao, Y.; Yang, Y.; Xiong, T. *Macromolecules* **2011**, *44*, 1788-1791.

(12) Wurthner, F.; Saha-Moller, C. R.; Fimmel, B.; Ogi, S.; Leowanawat, P.; Schmidt, D. *Chem Rev* **2015**.

(13) Bernard Valeur, M. N. B.-S. *Molecular Fluorescence, Wiley-VCH Verlag GmbH & Co* **2012**.

Chapter 5 Cyclized tetra PDI

5.1 Introduction

To date, the most widely studied strategy in the design of electron acceptors is to utilize a π-conjugated backbone of twisted 3D geometry that could improve the morphological compatibility with the donor polymer and lead to enhanced photovoltaic performance.[1-5] However, introducing steric hindrance and/or different orientation of chemical bonding to create the twisted 3D molecular geometry of acceptors would inevitably result in the conformational isomers in the solid packing state, and its impact on organic photovoltaic (OPV) performance is still unknown. Although several examples of high performance non-fullerene OPV have been released, [6-11] design guidelines for efficient non-fullerene acceptors is still insufficient. We believe that careful design of the chemical structure of the acceptor and thorough investigation into its impact on OPV performance would benefit and accelerate the development of non-fullerene solar cells.

In this chapter, the design and the syntheses of two acceptor structures: **β-TPB** and **bri-TPB** are described. In compound **β-TPB**, four perylene diimides (PDIs) are covalently bonded with the benzodithiophene (BDT) - thiophene (Th) core at the b-position with free rotation of PDIs resulting in **β-TPB** of varying molecular geometries. The cyclization between PDIs and the BDT-Th core generates **bri-TPB** which not only has enlarged conjugated skeleton, but also possesses a more rigid molecular geometry compared with **β-TPB**. **Bri-TPB** based inverted solar cells with **PTB7-Th** as the donor polymer shows the highest efficiency of 7.69%, which is 31% higher than the 5.85% obtained from **β-TPB** based device. The detailed study reveals that the rigidity of the molecular geometry has great impact on the packing patterns of itself and the donor polymer in the solid state, and is closely related to the OPV properties. The results demonstrate that enhancing the rigidity of the acceptor molecular geometry is an effective and new pathway to create high performance acceptor for OPV.

5.2 Result and discussion

5.2.1 Design and Synthesis.

β-TPB was synthesized by Suzuki coupling of BDT-Th-4Bpin with 4 equivalents of β-monobrominated PDI. As revealed in our previous study,[12] functionalization at the bay-position of PDI could lead to distortion in the conjugated backbone of PDI which is undesired for solar cell OPV properties. This problem can be fixed by 1) substitution on the α-position instead of the β-position as we reported before; or 2) by cyclization between BDT and PDI to eliminate repulsion between the β-hydrogen of PDI and the 3-position hydrogen on thiophene. As shown in Figure 5.1, cyclized via iron chloride, **β-TPB** is transformed into the bridged structure, bri-TPB, with a large PDI-BDT-PDI plane and two standing-up bridged PDI-Th units. **Bri-TPB** is obtained in moderate yield, and demonstrates high solubility in common organic solvent like chloroform, chlorobenzene. The structures of the two compounds were characterized and confirmed by mass spectrum, ^{1}H NMR and elemental analysis.

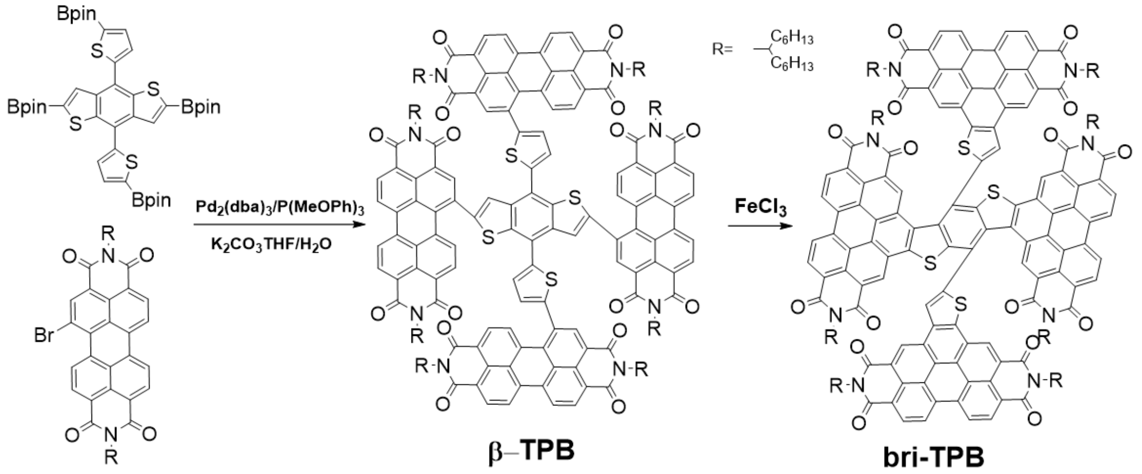

Figure 5.1 Synthetic scheme of β-TPB and bri-TPB.

5.2.2 DFT calculation.

To study the electronic properties and the structural difference of **β-TPB** and **bri-TPB**, density functional theory calculations using the Gaussian package b3lyp/6-31g (d) were performed to evaluate the frontier molecular orbitals and the geometry of **β-TPB** and **bri-TPB**. In order to facilitate the calculation, the long alkyl chains were replaced with methyl group. LUMO and HOMO orbitals configurations are shown in Figure 5.2. In **β-TPB**, LUMO orbitals localize on the electron poor PDI units while HOMO electron density localizes in the electron rich BDT-Th core, implying intramolecular charge transfer. However, in bri-TPB, the LUMO orbitals localize in the whole PDI-BDT-PDI conjugated plane while the HOMO orbitals spread out across both the electron rich BDT-Th core and the electron poor bridged PDI-Th, Loss of intramolecular charge transfer feature resulted in wider bandgap of **bri-TPB**.[13]

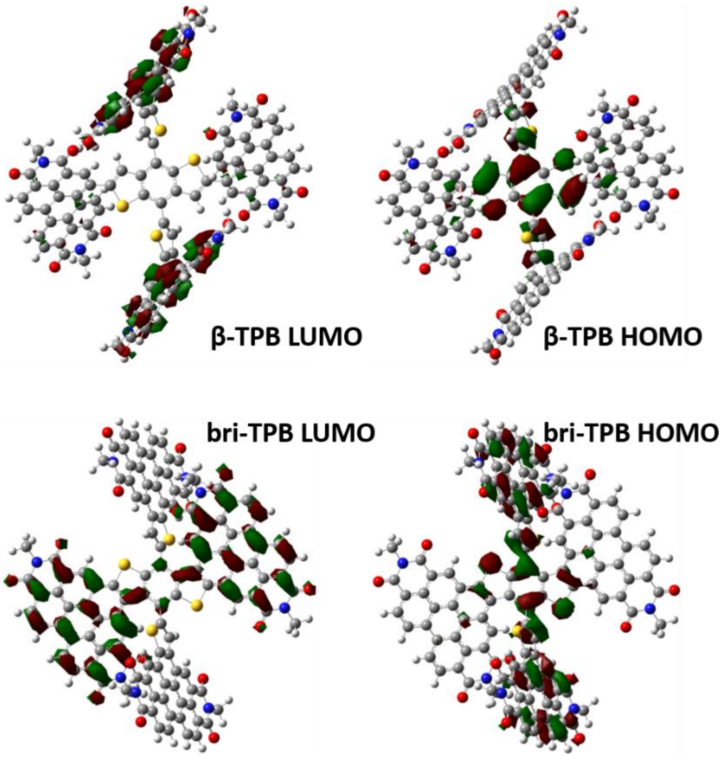

Figure 5.2 Frontier orbital configuration of β-TPB and bri-TPB.

The optimized molecular geometries of **β-TPB** and **bri-TPB** are presented in Figure 5.3. In **β-TPB**, all six dihedral angles between any two aromatic rings are between 53 to 55°, resulting in a 3D geometry of four PDIs. In **bri-TPB**, the fused PDI-BDT-PDI structure forms a large horizontal plane, and two bridged PDI-Th align parallel with each other making a 60° angle with horizontal plane. The angle between the fused PDI-BDT-PDI and the bridged PDI-Ths is 60° instead of 90° because of the steric repulsion between the alkyl diimide group of the horizontal PDI and the π plane of the perpendicular PDI. The 3D molecular geometry was observed in both **β-TPB** and **bri-TPB,** making them promising electron acceptor. The major difference between these two compounds is their conjugated skeleton size and rigidity. Since **β-TPB** contains six free-rotating single bonds, the PDIs in **β-TPB** have more freedom to rotate, resulting in varying molecular geometries of **β-TPB**. On the other hand, the **bri-TPB** has only two rotating bonds and more planar and rigid building units. The rotation of PDI-Ths is actually confined within 180° because of the steric confinement set by the diimide groups of the horizontal PDIs.

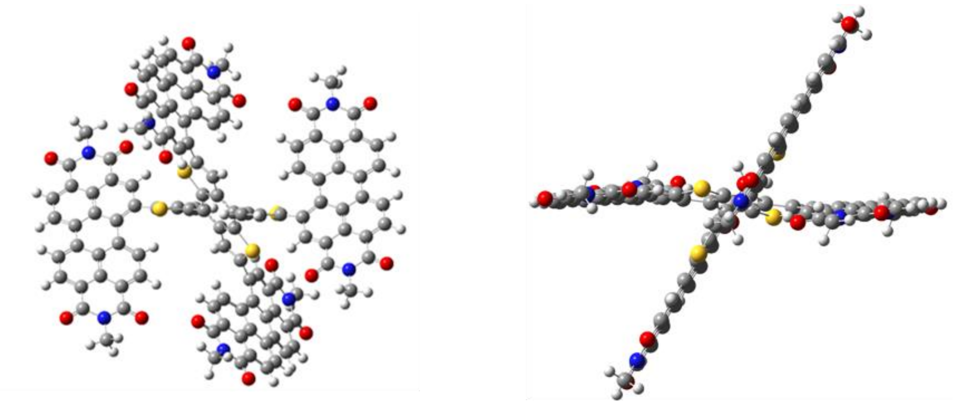

β-TPB **bri-TPB**

Figure 5.3 Optimized molecular geometry of β-TPB and bri-TPB, both with benzodithiophene core lying horizontally.

5.2.3 Electronic and optical properties.

The LUMO and the HOMO energy levels of the two compounds were measured by cyclic voltammetry. Compared with the LUMO energy levels of -3.79 eV for **β-TPB**, **bri-TPB** exhibits a higher LUMO energy level of -3.75 eV. By increasing the value of the difference between the LUMO of acceptor and the HOMO of donor, **bri-TPB** has the advantage of improving the V_{oc} value of OPV devices, thus facilitate the enhancement of solar cell performance. The deeper HOMO energy level of -6.21 eV for **bri-TPB** is observed while that for **β-TPB** is -5.92 eV. The bandgaps calculated from CV is 2.46 eV for **bri-TPB**, which is 0.33 eV larger than that for **β-TPB**.

The larger bandgap is further confirmed by their solution and film absorption spectra, which are shown in Figure 5.4. The solution spectrum of **β-TPB** shows the vibronic peaks between 450 and 600 nm with stronger 0-0 (I^{00}) absorption peaks than 0-1 (I^{01}) transition, which is similar with the PDI monomer. The absorption of **β-TPB** film made by spin-casting from chloroform solution exhibit stronger 0-1 (I^{01}) absorption peaks than 0-0 (I^{00}) transition. Blue shift of the highest absorption peak indicates strong intermolecular interaction of **β-TPB** in solid state, which is consistent with the formation of excimer in very dilute solution (10^{-9}mol/L), as evidenced by the concentration-dependent emission spectra. The strong intermolecular interaction of **β-TPB** in solid state can be explained by its low rigidity in the molecular geometry. This is because **β-TPB** can easily change its molecular geometry to facilitate the close packing of PDIs. The UV-vis absorption of **bri-TPB** in chlorobenzene (10^{-8}) exhibit five vibronic peaks between 350 nm and 550 nm with maximum absorption at 502 nm. To facilitate the peak assignment, the absorption of PDITh and PDIBDT in solution was measured separately. It can be assigned that the peaks 0-1 (I^{01}) and 0-2 (I^{02}) originate from the absorption of PDI-Ths while the absorption peaks of 0-0 (I^{00}), 0-3 (I^{03}) and 0-4 (I^{04}) correspond tothe absorption of PDI-BDT-PDI. However, the 0-0 (I^{00}) absorption peak of **bri-TPB** is apparently blue shifted compared with that of PDI-BDT-PDI, which is caused by the interruption of electron density distribution in PDI-BDT-PDI after introducing two fused PDI-Ths at the bay position. Due to the introduction of fused PDI-Ths, **bri-TPB** shows weak intermolecular interaction in solid state, as indicated by the similarities between the film absorption spectra and the solution absorption spectra in shapes and intensities. As a result of the removal of intramolecular charge transfer after cyclization, the maximum absorption of **bri-TPB** in solution is blue-shifted by 49 nm compared with that of **β-TPB**, which is in good agreement with its larger band gap calculated from CV data.

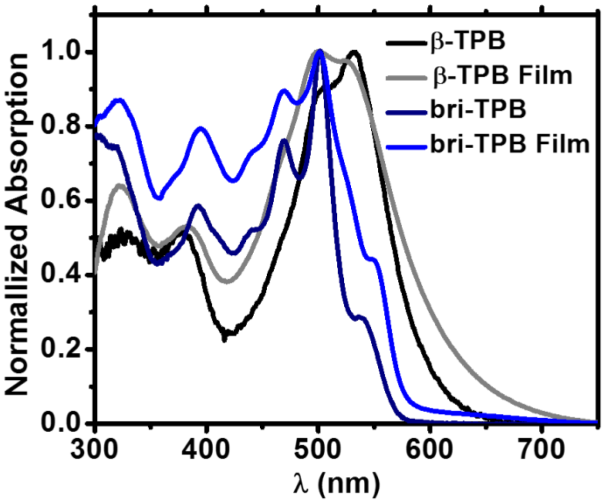

Figure 5.4 Solution and film optical absorption spectrum of βTPB and bri-TPB.

5.2.4 Photovoltaic Properties.

To evaluate the photovoltaic properties of **β-TPB** and **bri-TPB**, inverted solar cell devices were fabricated with the configuration of ITO/ZnO/**β-TPB** or **bri-TPB**: **PTB7-Th**/MoO_3/Ag. The device performance was measured under a simulated solar illumination of 100 mW/cm^2 Am 1.5G under nitrogen atmosphere. The J-V characteristics under illumination are shown in Figure 5.5. The photovoltaic properties are summarized in Table 5-1. The active layer with thickness of around 100 nm was spin-casted from hot chlorobenzene solution. The acceptor/donor mass ratio ranged from 2:1 to 0.8:1 was first investigated and the best acceptor/donor ratio was determined to be 1.5:1 for both **bri-TPB** or **β-TPB**:**PTB7-Th** devices. The **β-TPB**:**PTB7-Th** devices with 1.5:1 blend ratio show an optimized average PCE of 5.58 % with V_{oc} of 0.82 eV, J_{sc} of

11.9 mAcm^{-2} and *FF* of 0.57, while **bri-TPB**:**PTB7-Th** devices give the higher average PCE of 6.58 % with V_{oc} of 0.92 eV, J_{sc} of 12.8 mAcm^{-2} and *FF* of 0.56. The higher V_{oc} of **bri-TPB** based devices originate from its higher LUMO energy level after cyclization. Although the 0.09 eV difference in the LUMO energy level between **bri-TPB** and **PTB7-Th** is lower than the empirical 0.3 eV driving force for efficient charge separation, the **bri-TPB**:**PTB7-Th** devices still demonstrated promising photovoltaic performance. Addition of a small amount of diiodooctane (DIO) and diphenyl ether (DPE) can further increase the J_{sc} values from 12.8 to 14.7 mAcm^{-2} and result in an enhanced average PCE of 7.56 %. The highest PCE was found to be 7.69 % with V_{oc} of 0.92 eV, J_{sc} of 15.1 mAcm^{-2} and *FF* of 0.56. Performance enhancement was absent for the **β-TPB**:**PTB7-Th** based devices with DIO and DPE additives. Additions of the 2.5% DIO and 2.5% DPE deteriorated the J_{sc} from 11.9 mAcm^{-2} to 10.2 mAcm^{-2}, but slightly enhanced the V_{oc} and *FF*, which are typical characteristics of larger domain size caused by additives, and the overall result is a lower PCE of 5.16%.

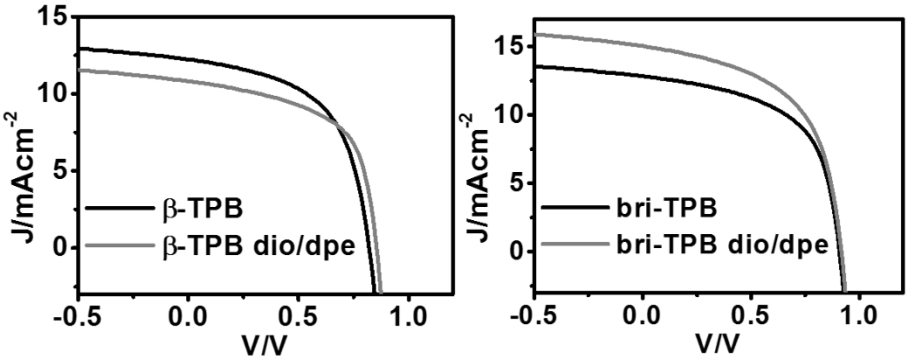

Figure 5.5 J-V curves of PTB7-Th/ β-TPB and bri-TPB devices.

Table 5-1 J-V characteristics of solar cell devices based on β-TPB:PTB7-Th and bri-TPB:PTB7-Th blend film; the hole and electron mobility of blend films using SCLC method.

Device	Additives	J_{sc} (mAcm^{-2})	V_{oc} (V)	FF	Eff(%) (best device)	μ_e (cm^{-2}V^{-1}s^{-1})	μ_h (cm^{-2}V^{-1}s^{-1})
β-TPB	N	11.9 ±0.6	0.82±0	0.57±0.01	5.58±0.27 (5.85)	5.23x10^{-5}	2.72x10^{-4}
β-TPB	DIO/DPE 2.5+2.5%	10.4 ±0.3	0.85±0	0.59±0.00	5.16±0.17 (5.33)	1.88x10^{-5}	1.62x10^{-4}
bri-TPB	N	12.8 ±0.2	0.92±0	0.56±0.00	6.58±0.13 (6.72)	4.45x10^{-5}	2.01x10^{-4}
bri-TPB	DIO/DPE 2.5+2.5%	14.7 ±0.4	0.92±0	0.56±0.00	7.56±0.13 (7.69)	4.67x10^{-5}	2.67x10^{-4}

The external quantum efficiency (EQE) of these devices was measured to evaluate the J_{sc} (Figure 5.6). The J_{sc} values calculated from EQE are all in less than 10% deviation from the J_{sc} calculated from OPV devices. The curves of the EQE spectra are very similar to the corresponding blend film absorption, indicating both the donor and the acceptors contribute to the J_{sc}. It should be noted that even the HOMO energy level difference between **bri-TPB** and **PTB7-Th** is around 1 eV, the holes generated in acceptor **bri-TPB** still can be efficiently transferred to donor polymer **PTB7-Th**[14].

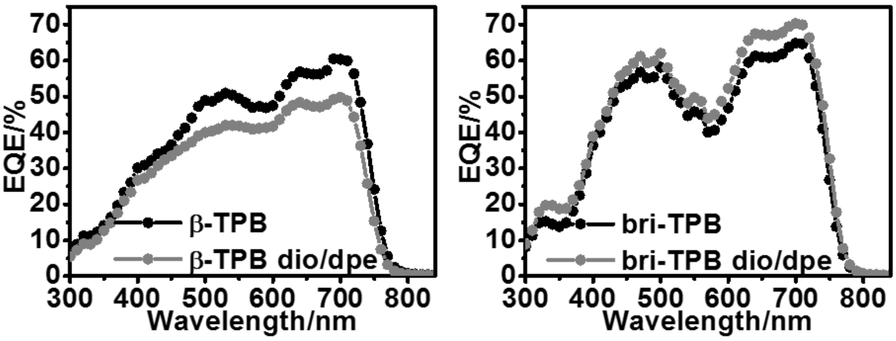

Figure 5.6 EQE spectrum of PTB7-Th/ β-TPB and bri-TPB devices.

The charge separation and recombination dynamics were also investigated by charge dissociation probability *P (E, T)* and light intensity dependence of J_{sc}, as shown in Figure 5.7. By plotting the photocurrent density J_{ph} (defined by J_L-J_D; J_L and J_D are light and dark current density) against the effective voltage V_{eff} (defined by V_o-V, V_o is the voltage where $J_{ph} = 0$) in logarithmic scale, the *P (E, T)* can be calculated by the equation J_{ph}/J_{sat}, where J_{sat} is the saturated J_{ph} at high reverse voltage, which is an indication of all the photogenerated exitons are dissociated to free charges and swept out. The *P (E, T)* under J_{sc} condition for **bri-TPB/PTB7-Th** without /with additives are 90 % and 87 %, respectively, which is in accordance with the slightly decrease of J_{sc} after the addition of DIO and DPE. The *P (E, T)* under J_{sc} condition for **bri-TPB/PTB7-Th** without /with additives are both 90 %, indicatingefficient exciton dissociation at the interfaces. The measurement of the J_{sc} as a function of illumination intensity in logarithmic scale was performed to evaluate the bimolecular recombination kinetics. A higher value of slope implies a weaker bimolecular recombination. If the slope reaches 1, all free carrier can be swept out and collected by the electrode. The linear scaling of photocurrent to light intensity was demonstrated for all four devices with the exponential factors of 0.96 and 0.94 for **β-TPB**:**PTB7-Th** devices without/with additive, and 0.96 and 0.95 for **bri-TPB**:**PTB7-Th** devices without/with additive, respectively. The relatively high and similar values imply that the bimolecular recombination in all the four devices is very weak.

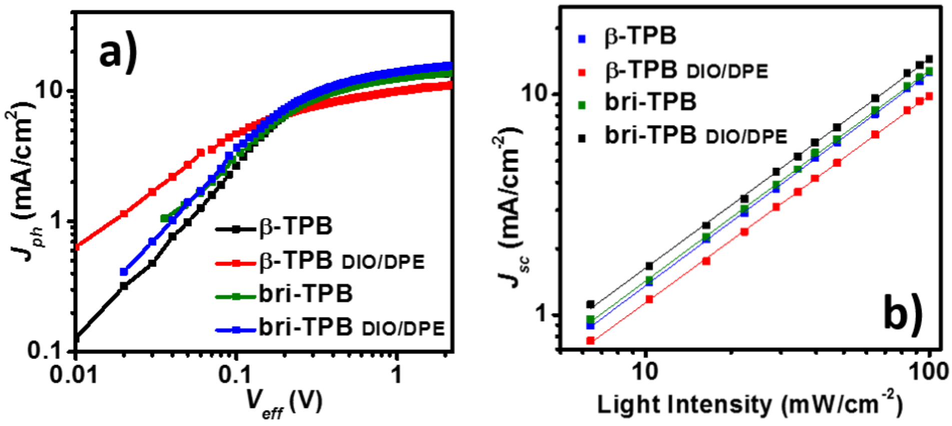

Figure 5.7 the photocuttent density (J_{sc}) versus effective voltage (V_{eff}) characteristics of the four solar cell devices; (f) the short current density (J_{sc}) agaist the light density of the four solar cell devices.

5.2.5 Active layer characterization.

The blend films UV-vis absorption was measured and presented in Figure 5.8. It was found that the shape and intensity of absorption spectrum of **bri-TPB** in blend film is very similar to that in neat film. This phenomenon indicates **bri-TPB** in blend films maintains the same packing order as in neat film, which may be due to its enlarged conjugation skeleton and rigid molecular geometry. However, the absorption of **β-TPB** in the blend film shows a sharp 0-0 vibrational peak at 533 nm and a lower 0-1 vibrational peak at 499 nm. This varies dramatically with its neat film absorption, but is very similar to its solution absorption spectrum. This indicates **β-TPB** in blend film takes a different packing pattern, which may be caused by the free rotation of PDIs in **β-TPB** forming different molecular geometry when the surrounding changes. It was also evidenced in the 2D grazing-incidence wide-angle X-ray scattering (GIWAXS) data.

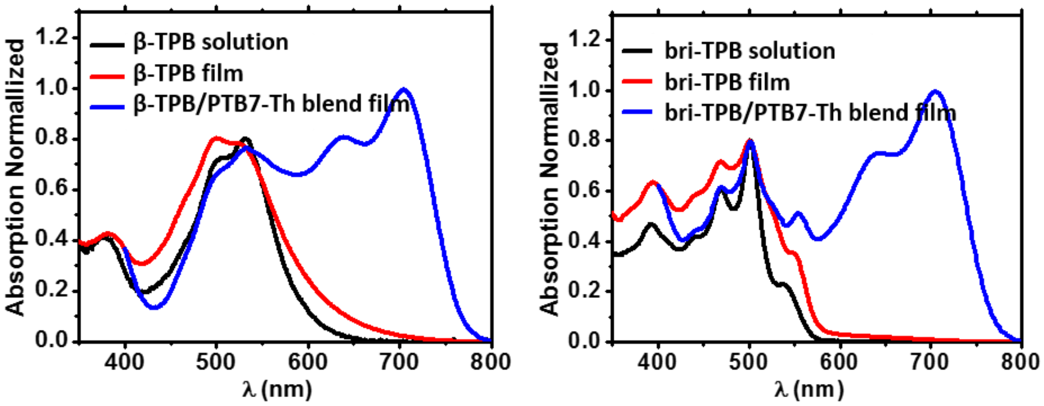

Figure 5.8 absorption of blend films with donor polymer or neat acceptors of βTPB and bri-TPB

The GIWAXS analysis was used to investigate the crystallinity and the molecular orientation of the pure and blend films. The 2D diffraction patterns are shown in Figure 5.9 and the out-of-plane/in-plane line cuts from GIXWAXS patterns are presented in Figure 5.10. Due to the 3D molecular geometry, the GIWAXS patterns of **β-TPB** and **bri-TPB** neat films both show two strong arc-like scattering, suggesting their crystalline nature and molecular orientation isotropy similar to $PC_{61}BM/PC_{71}BM$. The Bragg reflections at $q_y \approx 0.27$ Å $^{-1}$, 1.40 Å $^{-1}$ and 0.29 Å $^{-1}$, 1.36 Å $^{-1}$ was observed for **β-TPB** and **bri-TPB**, which corresponds to the d-spacing of 23.3, 4.5 and 22.1, 4.6 Å, respectively. The polymer **PTB7-Th** has two Bragg reflections at $q_y \approx 0.27$ Å $^{-1}$ (lamellar d-spacing) and q_z= 1.65 Å $^{-1}$ (π-π stacking). While its Bragg reflections at 0.27 Å $^{-1}$ is overlapped with that of the acceptors, the π-π stacking reflections at 1.65 Å $^{-1}$ can be used to study the crystallinity and the molecular orientation of **PTB7-Th**. In the blend film of **bri-TPB**:**PTB7-Th**, the π-π stacking reflections of **PTB7-Th** can be observed both in out-of-plane (q_z) and in-plane (q_y) direction. The intensity in q_z direction is higher than that in q_y direction, suggesting **PTB7-Th** preferentially takes a face-on orientation. In **β-TPB:PTB7-Th blend film**, the reflections of **β-TPB** at $q_y \approx 1.40$ Å $^{-1}$ in neat film down-shifts to 1.31 Å $^{-1}$, further reflecting **β-TPB** takes a different packing pattern in the blend film. After adding the DPE/DIO additive, the Bragg reflections at 1.65 Å $^{-1}$ in q_z

direction is enhanced for the **bri-TPB** blend film, suggesting more **PTB7-Th** domains take a face-on orientation that is beneficial for vertical charge transport and its corresponding OPV performance. For **β-TPB:PTB7-Th** blend film, the obvious enhancement of Bragg reflections at 0.31 Å $^{-1}$ most likely implies the additives further promote the edge-on orientation in **β-TPB** and/or **PTB7-Th.** Because of the ease of changing molecular geometry, **β-TPB** not only changes its packing pattern easily when the surrounding varies, but also promotes **PTB7-Th** preferentially takes an edge-on orientation that is undesired for OPV performance.

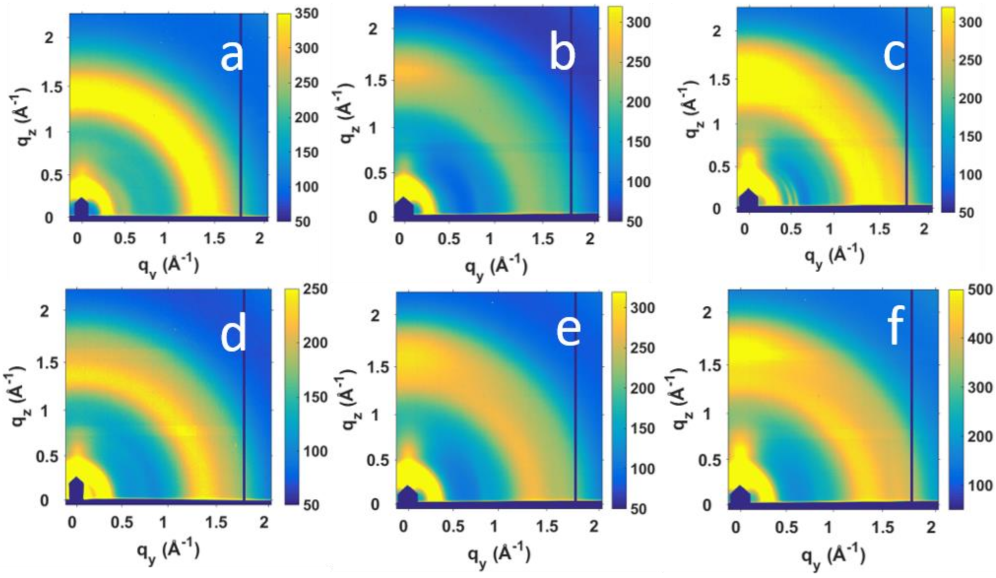

Figure 5.9 2D GIWAXS patterns of films on ZnO-modified Si substrates. a) neat β-TPB film; b), blend film of β-TPB:PTB7-Th without DIO:DPE additive; c), blend film of β-TPB:PTB7-Th with 2.5%DIO:2.5%DPE additive; d) neat Bri-TPB film; e), blend film of Bri-TPB:PTB7-Th without DIO:DPE additive; f), blend film of Bri-TPB:PTB7-Th with 2.5%DIO:2.5%DPE additive.

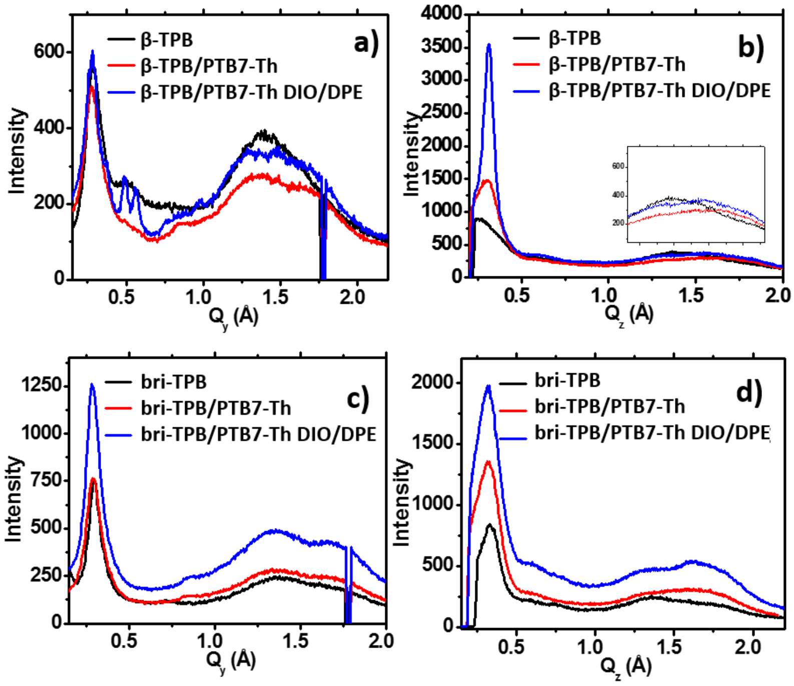

Figure 5.10 (a) in-plane line and (b) out-plane cuts of neat β-TPB film and blend films of β-TPB:PTB7-Th without/with 2.5%DIO:2.5%DPE additive. (c) in-plane line and (d) out-plane cuts line cuts of neat bri-TPB film and blend films of bri-TPB:PTB7-Th without/with 2.5%DIO:2.5%DPE additive.

Electron and hole mobility of the devices are measured by using the space-charge-limited current (SCLC) method with device configuration of ITO/PEDOT:PSS/**β-TPB** or **bri-TPB**:**PTB7-Th**/MoO_3/Ag for hole and ITO/ZnO/**β-TPB** or **bri-TPB**:**PTB7-Th**/Al for electron. The electron and hole mobility for **β-TPB** based device are 5.23x10^{-5} $cm^2V^{-1}s^{-1}$ and 2.72x10^{-4} $cm^2V^{-1}s^{-1}$, respectively. The DPE and DIO co-additives significantly reduce the mobilities to 1.88x10^{-5} $cm^2V^{-1}s^{-1}$ and 1.62x10^{-4} $cm^2V^{-1}s^{-1}$, which is consistent with the observation in GIWAXS data that additives promote **β-TPB** and **PTB7-Th** taking an edge-on orientation. The **bri-TPB** based device gives the electron and hole mobilities of 4.45x10^{-5} cm^{2}V^{-1}s^{-1} and 2.01x10^{-4} cm^{2}V^{-1}s^{-1} respectively. Similar hole and electron mobilities of 4.67 x10^{-5} cm^{2}V^{-1}s^{-1} and 2.67x10^{-4} cm^{2}V^{-1}s^{-1}, respectively, are observed for devices with DIO and DPE additives. The atomic force microscopy (AFM) was employed to investigate the films morphology of the blend films. Both **β-TPB**:**PTB7-Th** and **bri-TPB**:**PTB7-Th** blend films exhibit fibrous morphology with fine and similar domain size, suggesting their 3D molecular geometry facilitate to form favorable morphology for solar cells. The good blend film morphology could be further evidenced by the efficient photoluminescence quenching of **PTB7-Th** when it is excited at 640 nm Figure 5.12, indicating efficient charge separation following the excitation of the donor. Larger domain size is observed for both films after adding DIO and DPE additives. The additives also increase the root-mean-square (RMS) roughness of the blend films from 0.72 nm to 3.24 nm for **β-TPB**:**PTB7-Th**, and from 0.67 nm to 1.13 nm for **bri-TPB**:**PTB7-Th**. The large roughness enhancement of **β-TPB**:**PTB7-Th** indicate large domains are formed after adding additives, which is responsible for the reduced J_{sc} and PCE values.

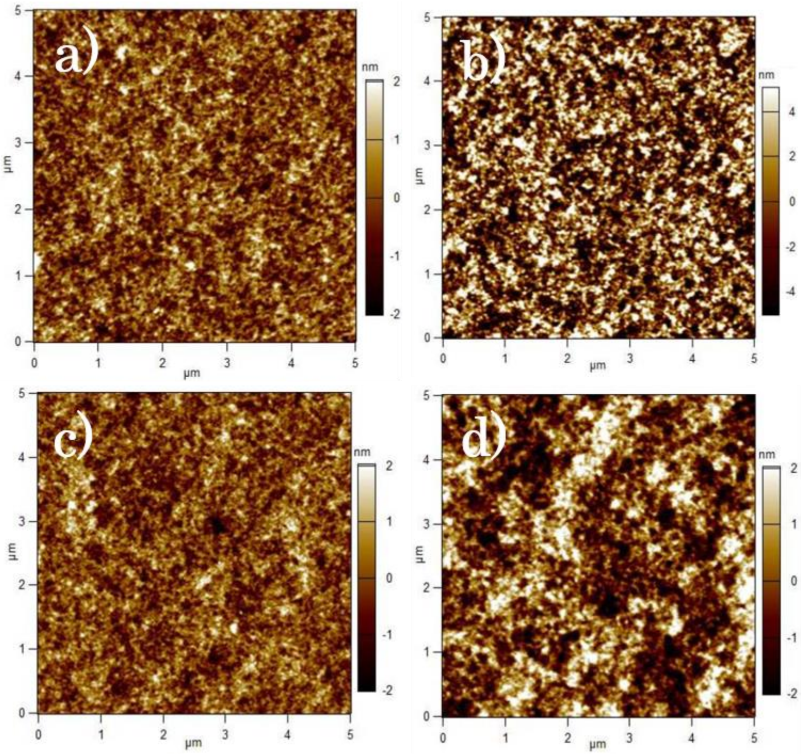

Figure 5.11 AFM of films of a) β-TPB:PTB7-Th film deposited without additives, b) β-TPB:PTB7-Th film with 2.5%DIO:2.5%DPE, c) bri-TPB:PTB7-Th film deposited without additives, d) bri-TPB :PTB7-Th film with 2.5%DIO:2.5%DPE.

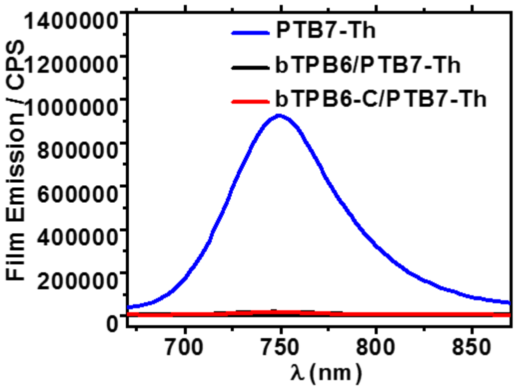

Figure 5.12 Film emission spectra of neat PTB7-Th film and the photoluminescence quenching of PTB7-Th in β-TPB:PTB7-Th and bata-bri-TPB:PTB7-Th blend film, excited at 640 nm.

5.2.6 Experimental section

Compound **β-TPB**

$Pd_2(dba)_3$ (25 mg)and $P(MeOPh)_3$ (75 mg) was added to the mixture of compound BDT-Th-4Bpin (107.3 mg), compound PDI-Br^{β} (437.8 mg), THF (12 mL) and 2M K_2CO_3 aqueous solution (3 mL) under nitrogen. After refluxing overnight, the mixture was poured into methanol. The red precipitate was filtered and purified by column chromatography, using dichloromethane/hexane = 1:1 as the eluent. 256 mg of pure **β-TPB** (73.8%) was obtained. ^1H NMR (500 MHz, CDCl3) δ (ppm): 8.86-8.68 (Br, 33H), 8.57 (Br, 4H), 8.06-8.12 (Br, 4H), 7.61 (Br, 2H), 7.28 (Br, 2H), 5.19-4.71 (Br, 8H), 2.12 (Br, 16H), 1.86 (Br, 16H), 1.18 - 0.75 (Br, 176H). MS (MALDI-TOF) $C_{218}H_{250}N_8O_{16}S_4$ m/z: 3363.79; Found: 3364.22 $(M + H)^+$ Anal. Calcd for $C_{218}H_{250}N_8O_{16}S_4$: C, 77.77%; H, 7.49 %; N, 3.33 %. Found: C, 77.54 %; H, 7.43 %; N, 3.19 %.

Compound **bri-TPB**

$FeCl_3$ (1 g) in 3 mL CH_3NO_2 was added to 6 mL CH_2Cl_2 solution of β–TPB (100 mg) at 0 °C. After one hour stirring at room temperature, 10 mL 1 M hydrochloride was added. The organic part was separated and the solvent was removed under reduced pressure. The product was purified by column chromatography, using dichloromethane/hexane = 1:1 as the eluent. 61 mg of pure **bri-TPB** (61.1 %) was obtained ^1H NMR (500 MHz,

$CDCl_2CDCl_2$) δ (ppm): 11.78 (Br, 2H), 10.18 (Br, 2H), 9.51 - 9.07 (Br, 18H), 8.76 (Br, 4H), 5.43-4.61 (Br, 8H), 2.06-0.73 (Br, 176H). MS (MALDI-TOF) $C_{218}H_{242}N_8O_{16}S_4$ m/z: 3355.73; Found: 3355.43 (M) $^+$ Anal. Calcd for $C_{170}H_{154}N_8O_{16}S_4$: C, 77.96; H, 7.26; N, 3.34. Found: C, 76.65; H, 7.03; N, 3.35.

Materials and Characterization Techniques are similar to what described in Chapter 3, except for that Ag is used for device counter electrode instead of Al.

5.3 Conclusion

The **β-TPB** can be cyclized with iron chlorideand the resulting **bri-TPB** possesses a large and planar fused PDI-BDT-PDI structure and two fused PDI-Th cores. The cyclization removes the intramolecular charge transfer. This is confirmed by the increase in band gap indicated by the large blue-shifted observed in the UV-Vis absorption spectrum and by the CV data. DFT calculation revealed that both **β-TPB** and **bri-TPB** show a 3D molecular geometry that encourages favorable blend film morphology with **PTB7-Th**. This point is reconfirmed by efficient photoluminescence quenching of **PTB7-Th**, indicating efficient charge separation following the excitation of the donor. The difference between **β-TPB** and **bri-TPB** is the conjugated backbone size and the flexibility of molecular geometry. The free rotation of PDIs can render the **β-TPB** with varying molecular geometry, thus, its packing pattern in solid state can be easily changed when composition of blend varies. This characteristic makes donor polymer **PTB7-Th** preferentially take on an edge-on orientation. Due to high rigidity of molecular geometry and enlarged conjugated skeleton, **bri-TPB** promotes **PTB7-Th** to take on a face-on orientation in solid state packing. The **bri-TPB** based inverted solar cells shows the highest efficiency of 7.69 % with V_{oc} of 0.92 eV, J_{sc} of 15.1 mAcm^{-2} and FF of 0.56, which is 31% higher than the 5.85% of the **β-TPB** based devices. The close relationship between molecular geometry rigidity and its OPV performance for non-fullerene solar cell indicates a new pathway to design highly efficient non-fullerene acceptors.

5.4 References

(1) Sun, D.; Meng, D.; Cai, Y.; Fan, B.; Li, Y.; Jiang, W.; Huo, L.; Sun, Y.; Wang, Z. *J Am Chem Soc* **2015**, *137*, 11156-11162.

(2) Li, H.; Hwang, Y.-J.; Courtright, B. A. E.; Eberle, F. N.; Subramaniyan, S.; Jenekhe, S. A. *Adv Mater* **2015**, *27*, 3266-3272.

(3) Zang, Y.; Li, C.-Z.; Chueh, C.-C.; Williams, S. T.; Jiang, W.; Wang, Z.-H.; Yu, J.-S.; Jen, A. K. Y. *Adv Mater* **2014**, *26*, 5708-+.

(4) Lee, J.; Singh, R.; Sin, D. H.; Kim, H. G.; Song, K. C.; Cho, K. *Adv Mater* **2016**, *28*, 69-+.

(5) Liu, Y.; Mu, C.; Jiang, K.; Zhao, J.; Li, Y.; Zhang, L.; Li, Z.; Lai, J. Y. L.; Hu, H.; Ma, T.; Hu, R.; Yu, D.; Huang, X.; Tang, B. Z.; Yan, H. *Adv Mater* **2015**, *27*, 1015-1020.

(6) Lin, Y.; He, Q.; Zhao, F.; Huo, L.; Mai, J.; Lu, X.; Su, C.-J.; Li, T.; Wang, J.; Zhu, J.; Sun, Y.; Wang, C.; Zhan, X. *J Am Chem Soc* **2016**, *138*, 2973-2976.

(7) Wu, Q. H.; Zhao, D. L.; Schneider, A. M.; Chen, W.; Yu, L. P. *J Am Chem Soc* **2016**, *138*, 7248-7251.

(8) Meng, D.; Sun, D.; Zhong, C.; Liu, T.; Fan, B.; Huo, L.; Li, Y.; Jiang, W.; Choi, H.; Kim, T.; Kim, J. Y.; Sun, Y.; Wang, Z.; Heeger, A. J. *J Am Chem Soc* **2016**, *138*, 375-380.

(9) Zhong, Y.; Trinh, M. T.; Chen, R.; Purdum, G. E.; Khlyabich, P. P.; Sezen, M.; Oh, S.; Zhu, H.; Fowler, B.; Zhang, B.; Wang, W.; Nam, C.-Y.; Sfeir, M. Y.; Black, C. T.; Steigerwald, M. L.; Loo, Y.-L.; Ng, F.; Zhu, X. Y.; Nuckolls, C. *Nature communications* **2015**, *6*, 8242-8242.

(10) Zhao, W. C.; Qian, D. P.; Zhang, S. Q.; Li, S. S.; Inganas, O.; Gao, F.; Hou, J. H. *Adv Mater* **2016**, *28*, 4734-4739.

(11) Bin, H. J.; Zhang, Z. G.; Gao, L.; Chen, S. S.; Zhong, L.; Xue, L. W.; Yang, C.; Li, Y. F. *J Am Chem Soc* **2016**, *138*, 4657-4664.

(12) Zhao, D.; Wu, Q.; Cai, Z.; Zheng, T.; Chen, W.; Lu, J.; Yu, L. *Chem Mater* **2016**, *28*, 1139-1146.

(13) Zhong, H.; Wu, C. H.; Li, C. Z.; Carpenter, J.; Chueh, C. C.; Chen, J. Y.; Ade, H.; Jen, A. K. *Advanced materials* **2015**.

(14) Lu, L.; Xu, T.; Chen, W.; Landry, E. S.; Yui, L. *Nat Photonics* **2014**, *8*, 716-722.

Chapter 6 Covalently Bound Clusters of Alpha-substituted PDI—Rival Electron Acceptors to Fullerene for Organic Solar Cells

This chapter contains parts of the published work [Wu, Q; Zhao, D.; Schneider A.M. *et al. J. Am. Chem. Soc.* **2016**, 13*8*, 7248–7251] Copyright (2016) American Chemical Society.

6.1 Introduction

As demonstrated in chapter 3, α-substituted PDIs are ideal building blocks for non-fullerene acceptors. In the following studies shown in chapter 4 and chapter 5, acceptor molecules with a 3D geometry exhibited higher J_{sc} value and higher solar cell performance, compared to the 2D counterpart. The knowledge we learned so far lead us to design a molecule with 3D geometry and alpha-PDI building blocks.

In this chapter, the synthesis and characterization of a new electron acceptor based on covalently bound clusters of alpha-substituted PDI which rival fullerene for organic photovoltaic (OPV) solar cells with an efficiency > 8.4% is described. The resulting acceptor molecules rival fullerene as electron acceptor. [1]

Small electron-rich moiety coupled with multiple electron deficient moieties (A_m-D-A_m) hold promise as high efficient acceptors for solar cells.[2,3] The versatility of donor and acceptor structures makes the fine-tuning in optical, electronic and film forming properties possible.[4-9] Previous studies have shown that acceptors with twisted 3D structure improves the morphological compatibility with the donor polymers and leads to enhanced photovoltaic performance.[3a, 3b, 6] Hence, highly-twisted or non-fully conjugated donor moieties were used to build the acceptors with the nonplanar 3D geometry. [10-12] However, the strongly twisted π-conjugation is likely to undermine the charge transport and diminish their potential as effective electron acceptors. We developed a high efficient electron acceptor TPB for solar cells (Figure 6.1). The BDT-Th unit has a coplanar π-conjugated backbone, which is conjugated through at least three directions with each terminal. The α-substituted PDI derivatives was shown to exhibit superior photovoltaic performance over β-isomer because the α-position functionalized PDI shows better planarity which facilitates close packing of π-conjugated backbone. [13,14]

6.2 Results and discussion

6.2.1 Synthesis.

Selective borylation of BDT-Th via Ir-catalyzed reaction yields compound BDT-Th-4Bpin, which is purified by recrystallization in hexane. Suzuki coupling between BDT-Th-4Bpin with 4 equivalents of a-monobrominated PDI generates **TPB**. **TPB** exhibit high solubility in common organic solvents such as chlorobenzene and chloroform. The structure of **TPB** was characterized and confirmed by ^{1}H NMR, mass spectrum and elemental analysis.

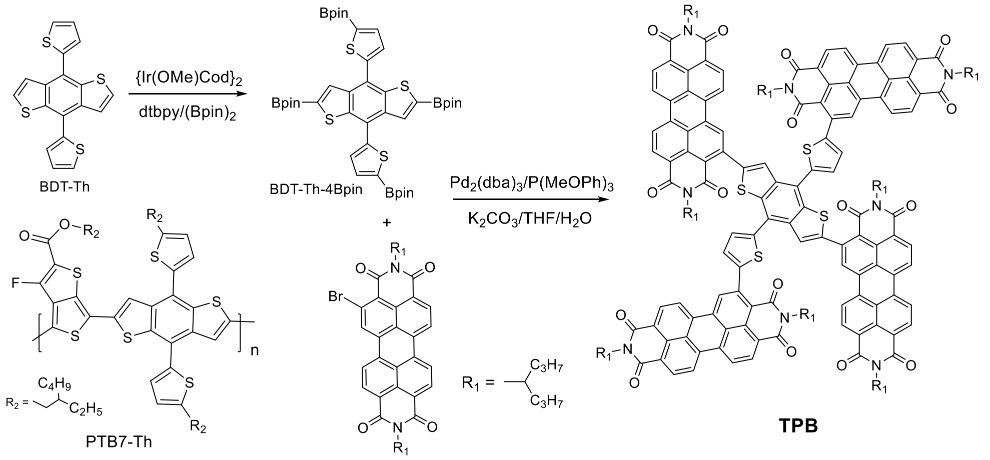

Figure 6.1 Synthetic route of TPB and chemical structure of PTB7-Th.

6.2.2 OPV properties.

Inverted solar cell devices were fabricated with the configuration of ITO/ZnO/**TPB:PTB7-Th**/MoO_3/Ag The active layer with thickness of approximately 80 nm was deposited by spin-casting from hot chlorobenzene. The solar cell devices were tested under a simulated solar illumination of 100 mW/cm^2 AM 1.5G under nitrogen atmosphere. Table 6-2 summarizes the photovoltaic properties of the solar cells. The *J*-*V* curves and EQE spectra are shown in the Figure 6.2.

Devices with varying **TPB/PTB7-Th** mass ratio from 1.5:1 to 1:1.5 were prepared and tested. The solar cells with 1:1 blend ratio show optimized average power conversion efficiency (PCE) of 6.62 % with J_{sc} of 17.6 mAcm^{-2}, V_{oc} of 0.8 V and *FF* of 0.47.

Additives such as 1,8-diodooctane (DIO), dimethyl sulfoxide (DMSO) and diphenyl ether (DPE) is proved effective to further enhance the performance of devices. As shown in Table 6-1, addition of a small amount of DIO (0.12% v/v) or DMSO (0.15% v/v) can significantly improve the PCE from 6.62 % to 7.34 % and 7.44 %, respectively. The PCE enhancement is largely come from the increase of *FF* from 0.47 to 0.53, 0.54, respectively.

Table 6-1 *J-V* characteristics of solar cell devices with TPB:PTB7-Th (1:1) active layer.

Additive (%)	J_{sc} (mAcm^{-2})	V_{oc} (V)	*FF*	Eff$_{ave}$ (%)	Eff$_{max}$ (%)
DIO 0.12 %	17.71±0.6	0.79±0.01	0.52±0.01	7.34±0.14	7.48
DIO 0.3 %	17.04±0.5	0.79±0.01	0.52	7.03±0.19	7.22
DIO 1%	16.68±0.4	0.79±0.01	0.52	6.90±0.21	7.11
DMSO 0.15%	17.85±0.4	0.77±0.01	0.54±0.01	7.44±0.15	7.59

It was also found that the addition of 5% diphenylether (DPE) can improve the *FF* of device from 0.47 to 0.58; accompanied with slight decreases in the J_{sc} value. The highest PCE of 8.47 % (average PCE of 8.11 %) was achieved with 8% DPE. The high J_{sc} value (>18 mAcm^{-2}) is comparable with that (15 mAcm^{-2} - 19 mAcm^{-2}) for solar cells based on PC$_{71}$BM/**PTB7-Th**.[15] However, the bottleneck is the low the *FF* values of devices (< 0.6), yet indicating the potential for further improvement. Further increase in DPE concentration to 10% deteriorates J_{sc}, V_{oc} and FF values, thus PCE (6.70 %). The J_{sc} values calculated from EQE of encapsulated **TPB:PTB7-Th** devices without/with 8% DPE as additive match well with J_{sc} values measured in encapsulated solar cell devices in less than 5% deviation. The **TPB:PTB7-Th** devices showed broad EQE spectra from 300 nm to 800 nm, in which the maximum values approach 75%. The spectral shape of EQE curves is similar to the absorption spectrum of blend films. To fulfill the potential of **TPB** based solar cells, further device optimization is in progress.

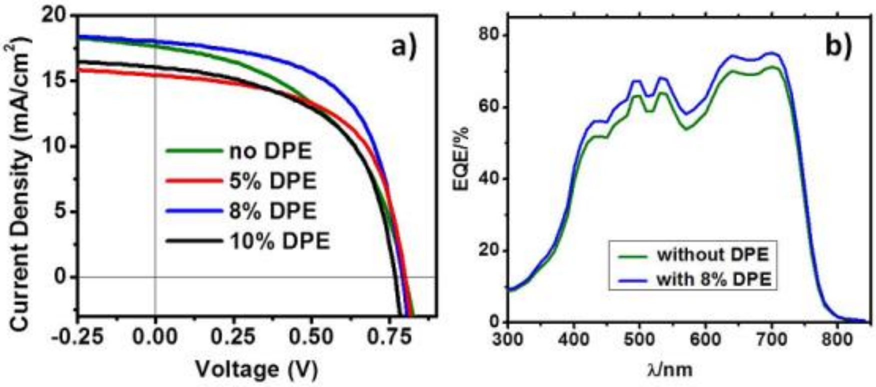

Figure 6.2 a) J−V characteristics of TPB:PTB7-Th based solar cell devices without/with 5%, 8% and 10% DPE as additive; b) External quantum efficiency spectra of TPB:PBT7-Th devices without/with 8% DPE as additive, which were sealed by Norland UV glue.

Table 6-2 *J-V* characteristics of solar cell devices with TPB:PTB7-Th active layer.

DPE(%)	J_{sc} (mA cm^{-2})	V_{oc} (V)	*FF*	Eff$_{ave}$ (%)[a]	Eff$_{max}$ (%)
0	17.6 ±0.2	0.80±0.00	0.47±0.02	6.62±0.33	7.03
5	15.6±0.5	0.80±0.00	0.58±0.00	7.22±0.22	7.62
8	17.9±0.4	0.79±0.00	0.58±0.01	8.11±0.26	8.47
10	16.1±0.4	0.77±0.01	0.54±0.01	6.70±0.20	6.90

[a] The PCEs were obtained for over 18 devices.

6.2.3 DFT calculation, electronic and optical properties.

To answer the question of why **TPB** exhibits high PCE values in OPV devices, the frontier molecular orbitals and the geometry of **TPB** were calculated based on the density functional theory with Gaussian package b3lyp/6-31g(d). In order to facilitate the calculation, one of the two alkyl chains in the PDI, far away from substitution position, was replaced with a methyl group. The resulting molecular geometry is shown in Figure 6.5a, and the LUMO and HOMO orbitals are presented in the Figure 6.3. It is clear that the HOMO electron density localizes at BDT-Th core while the LUMO orbital localizes at PDI unit, suggesting a significant charge polarization in the exited state.

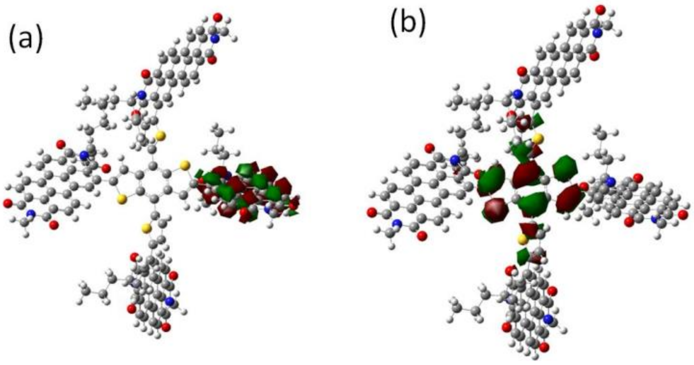

Figure 6.3 LUMO (a, -3.55 eV) and HOMO (b, - 5.37 eV) orbitals of TPB, which is simulated with Gaussian b3lyp/6-31gd

The optimized molecular geometry showed the dihedral angle between two PDIs and BDT is 58.9° and 50.2°, respectively, twist angle of 9° between the two PDI units connected with BDT. The dihedral angle between thiophene and BDT, thiophene and PDI are 50°, 50°, 55°, 55°, respectively, which lead to two parallel PDI units. The two PDI units connected through thiophene are nearly perpendicular to the plane of two PDIs connected through BDT. Therefore, the PDI moieties are still partially conjugated with the BDT-Th core. It can be envisioned that when a donor polymer chain interacts with a TPB molecule, only one of the four PDI units can have optimized π-π interaction due to steric effect, shown in Figure 6.4. Photo-induced charge transfer occurs from **PTB7-Th** to one of the PDI units; the electron can further find a pathway to be transmitted to other PDI units that is farther away from the donor polymer chain so that electron-hole binding energy between donor polymer and acceptor can be reduced due to longer distance.

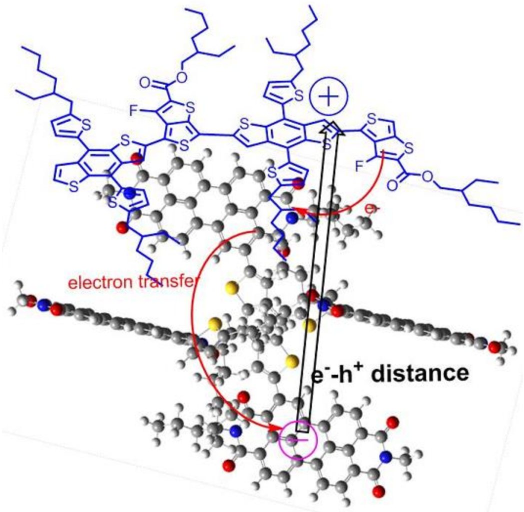

Figure 6.4 Graphic illustration of impact of cross-like geometry on charge separation.

As shown in Figure 6.5 c, the UV-Vis absorption of **TPB** solution in chlorobenzene (10^{-7} M) exhibits three vibronic peaks between 450 - 550 nm with a maximum extinction coefficient of 2.33×10^{-5} $M^{-1}cm^{-1}$ at 530 nm. The maximum absorption of TPB film appears at 575 nm, red-shifted by 24 nm from that in solution, which might reflect the extension of conjugation in solid state due to forced planarity caused by intermolecular interaction of **TPB** in the film. In contrast to the solution spectra, in which the strongest absorption peak is the 0-0 (I^{00}) transition, the strongest absorption peak in film is 0-1 (I^{01}) peak. The red-shifted maximum absorption and the strongest 0-1 (I^{01}) absorption peak of the film might suggest the intermolecular π-π stacking of **TPB** in the solid state.[13,14] The film absorption range (450 to 580 nm) of **TPB** complements to that of **PTB7-Th** (550 to 770 nm) and favors solar energy harvesting.

The LUMO and HOMO energy levels of **TPB** were determined to be - 3.89 eV and -5.71 eV, respectively, (Figure 6.5 b) with cyclic voltammetry studies using ferrocene (-4.8 eV) as standard reference. Both of which match with the LUMO and HOMO of **PTB7-Th** with enough energy offset for both electron and hole transfer to each other (Figure 6.5 d). It is worth to note that the HOMO energy difference between **PTB7-Th** and **TPB** is 0.49 eV, much smaller than that between **PTB7-Th** and $PC_{71}BM$ (0.89 eV). Thus, holes generated in **TPB** can be more effectively extracted by **PTB7-Th**.[15]

The emission spectra of **TPB** in dilute chlorobenzene (10^{-7} M) are similar to those of PDI, with very limited emission quantum yield (QY) too weak to calculate, which is consistent with the significant polarization in the excited state as shown by the DFT calculation. There is no significant change in absorption spectra of **TPB** in **TPB/PTB7-Th** blend films (Figure 6.5 c) from that of pure **TPB**. The most relevant observation is that both **TPB** and **PTB7-Th** photoluminescence are almost completely quenched when they are excited at either 490 or 640 nm, indicating an efficient charge separation following excitation of either donor or acceptor (Figure 6.5 f).

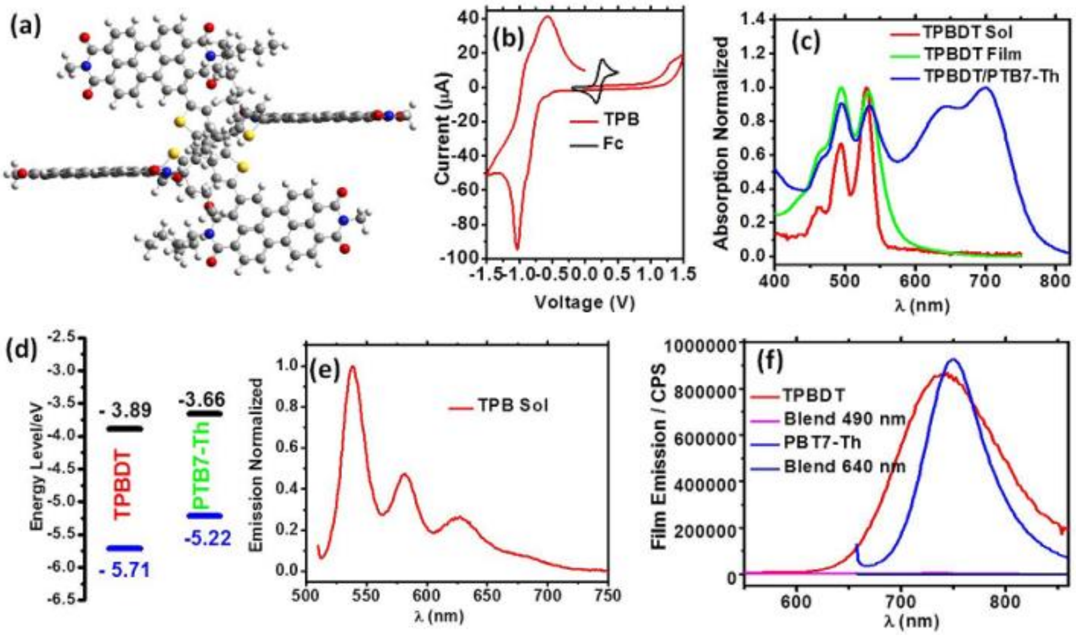

Figure 6.5 : (a) the side view of calculated geometries of TPB. (b) Cyclic voltammograms of TPB film with Fc/Fc^+ as the reference. (c) absorption spectra of TPB solution and film and blend film of TPB:PTB7-Th. (d) Schematic energy level of TPB and PTB7-Th. (e) emission spectra of TPB solution in chlorobenzene (10^{-7} M). (f) emission spectra of TPB, PTB7-Th films, and TPB:PTB7-Th blend film.

This point is further reinforced by measurements of the charge dissociation probability $P(E, T)$. The $P(E, T)$ is defined as J_{ph}/J_{sat}; J_{ph} is defined by $J_L - J_D$ (J_L and J_D are light and dark current densities); J_{sat} is where the J_{ph} reaches its saturation at high reverse voltage which means all the photogenerated exitons are dissociated to free charge carriers and collected by the electrodes. The plot of photo current density against the effective voltage V_{eff} (defined by V_0-V, V_0 is voltage where J_{ph}=0) in logarithmic scale allows the calculation of $P(E, T)$ under J_{sc} condition, yielding 96% and 94% for the as-deposited blend film and the blend film with 8% DPE as the additive, respectively (Figure 6.6a). The high and similar *P(E,T)* values indicate the efficient exciton dissociation occurs at interfaces between **TPB** and **PTB7-Th**. The *P(E,T)* values for the blend film with 8 % DPE under 0 - 0.7 V work condition is higher than that for blend film without DPE, which is consistent with the *FF* improvement after adding 8 % DPE. The measurement of the J_{sc} as a function of illumination intensity in logarithmic scale reveals insight into the recombination kinetics. If the slope of the curve reaches 1, it implies weak bimolecular recombination and the free carriers can be swept out and collected by the electrodes efficiently. In Figure 6.6 b, the linear scaling of photocurrent to light intensity was observed for both two devices with the same exponential factors of 0.97, indicating that the bimolecular recombination in the two devices is both very weak.

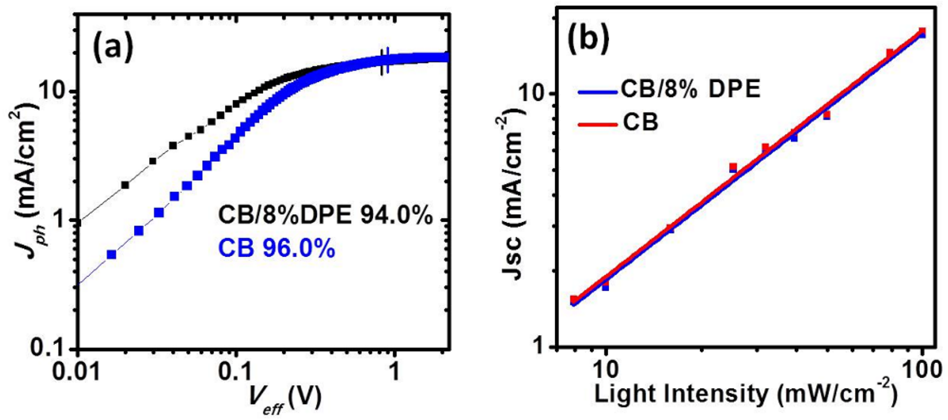

Figure 6.6 (a) photocurrent density (J_{ph}) versus effective voltage (V_{eff}) characteristics of the two devices; (b) short current density (J_{sc}) versus the light density of the two devices.

6.2.4 Active layer characterization.

An intriguing observation is that the electron and hole mobility of the devices are very low, as measured by using space-charge-limited current (SCLC) method with device structure of ITO/ZnO/**TPB:PTB7-Th**/Ca/Al for electrons, ITO/PEDOT:PSS/**TPB:PTB7-Th**/MoO_3/Ag for holes. The device without DPE additive gives electron and hole mobility of 4.13×10^{-6} and 6.65×10^{-6} $cm^2V^{-1}s^{-1}$, respectively. After adding 8% DPE as the additive, the electron and hole mobility increases to 6.10×10^{-6} and 1.08×10^{-5} $cm^2V^{-1}s^{-1}$, consistent with the observed *FF* increase from 0.47 to 0.58. The relatively low electron mobility is in agreement with the amorphous nature of **TPB** film (see Figure 6.7, the GIWAXS data), which is the reason of low *FF* value for **TPB** based OPV devices, indicating further research direction.

The crystallinity and molecular orientation of pristine **TPB** and blend films were investigated by grazing-incidence wide-angle X-ray scattering (GIWAXS) measurement and the 2D-GIWAXS patterns and the corresponding in-plane/out-plane line cuts were shown in Figure 6.7. The neat film of **TPB** shows very weak Bragg reflections at $q_y \approx 0.30$ $Å^{-1}$, corresponding to the d-space of 20.9 Å. The weak Bragg reflections indicate the lack of crystalline domains or the amorphous nature of **TPB** film which might be caused by the cross-like geometry of **TPB** molecular. The amorphous TPB film is in accord with its low electron mobility (<10^{-5} $cm^2V^{-1}s^{-1}$). The blend films with/without DPE as additive both demonstrate an arc-like scattering from the Bragg diffraction of periodic **PTB7-Th** layers at $q_y \approx 0.28$ Å^{-1}, and Bragg reflections at $q_z \approx 1.63$ Å^{-1}, corresponding to the π-π stacking distance of **PTB7-Th**, indicating the preferential face-on orientation of **PTB7-Th**. The in-plane/out-plane line cuts data both demonstrate that the blend films with/without the DPE as additive exhibit the similar diffraction intensity which implies the minimal impact of 8% DPE additive on the film crystallinity.

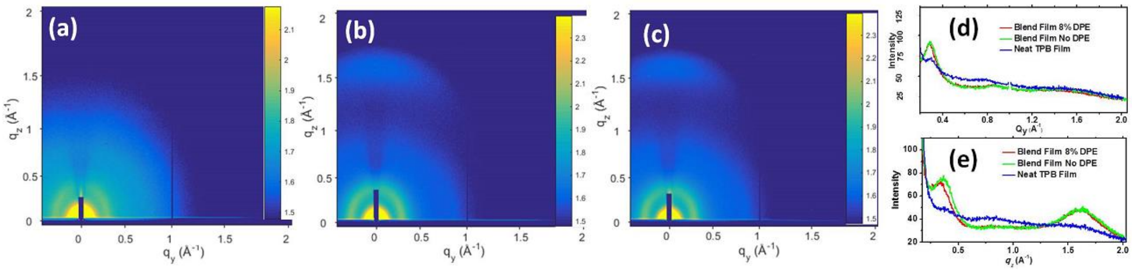

Figure 6.7 2D GIWAXS patterns of films on ZnO-modified Si substrates. a) pristine TPB film; b), blend film of TPB:PTB7-Th without DPE additive; c), blend film of TPB:PTB7-Th with 8% DPE additive; d, e) in-plane/out-plane line cuts of pristine TPB film and blend films of TPB:PTB7-Th without/with 8% DPE additive.

An intriguing observation is that the electron and hole mobility of the devices are very low, as measured by using space-charge-limited current (SCLC) method with device structure of ITO/ZnO/**TPB:PTB7-Th**/Ca/Al for electrons, ITO/PEDOT:PSS/**TPB:PTB7-Th**/MoO_3/Ag for holes. The device without DPE additive gives electron and hole mobility of 4.13×10^{-6} and 6.65×10^{-6} $cm^2V^{-1}s^{-1}$, respectively. After adding 8% DPE as the additive, the electron and hole mobility increases to 6.10×10^{-6} and 1.08×10^{-5} $cm^2V^{-1}s^{-1}$, consistent with the observed *FF* increase from 0.47 to 0.58. The relatively low electron mobility is in agreement with the amorphous nature of **TPB** film, which is the reason of low *FF* value for **TPB** based OPV devices, indicating further research direction.

Changes in PCE and mobility values imply changes in blend film morphology/topography. Since both donor and acceptor materials exhibit minimal contrast in atomic composition, TEM results are not informative in phase separation (Figure 6.8). As shown in Figure 6.8 c, d, the morphology of blend films spin-cast from chlorobenzene with and without 8% DPE both show fibrous feature with fine and similar domain sizes, suggesting the minimal impact of DPE additive on the blend film morphology. However, it can be ascertain that the fibrous film morphology with fine domain size is beneficial to achieving the high J_{sc} values. However, AFM images indicated that the 8% DPE additive increases the root-mean-square (RMS) roughness of the blend film surface from 0.5 nm to 0.9 nm (Figure 6.8 a b). The higher RMS roughness of surface increases the contact area between the active layer and interfacial electrode, thus enhance charge collection.[16]

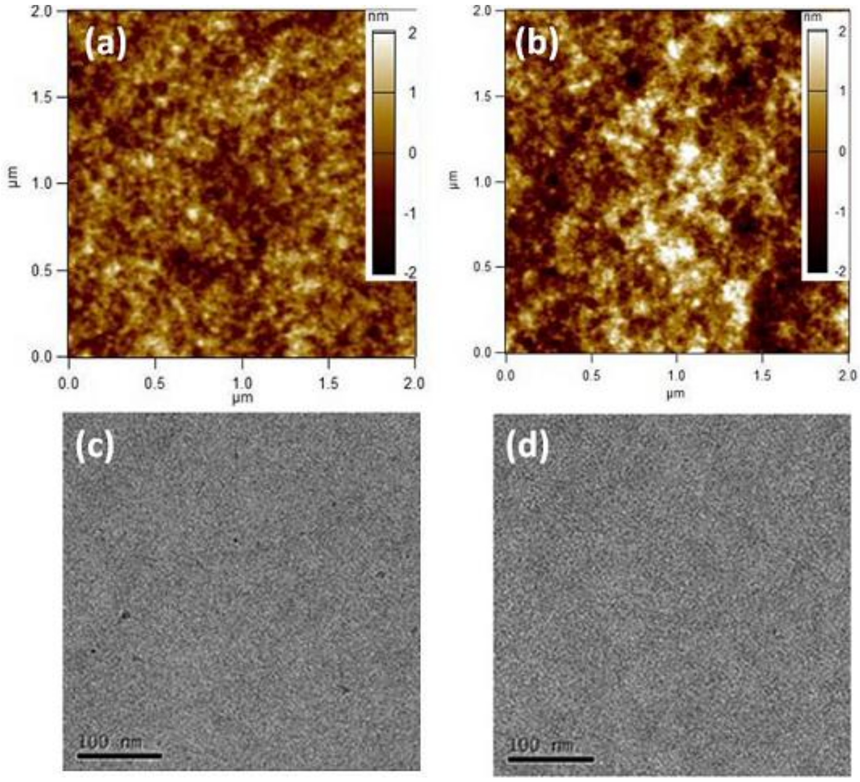

Figure 6.8 Atomic force microscopy (AFM) of TPB/PTB7-Th films: a) without additive; b) 8% DPE as additive; Transmission electron microscopy (TEM) images of the TPB/PTB7-Th films: c) without additive; d) with 8% DPE as additive.

6.2.5 Experimental section

Compound BDT-Th-4Bpin

To a mixture of BDT-Th (0.445g, 1.25 mmol), $(BPin)_2$ (1.91 g, 7.52 mmol), 4,4'-di-tert-butyl-2,2'-dipyridyl (91 mg, 0.34 mmol) and {Ir(OMe)Cod} (45 mg, 0.068 mmol) in 50 mL sealed tube, 20 ml anhydrous hexane were added under N_2 atmosphere. After reacting at 120 °C for 48 hours, the solvent was removed under reduced pressure. 0.746 g of pure compound BDT-Th-4Bpin (69 %) was obtained by recrystalization in hexane and methanol. M.p. 329 °C. ^{1}H NMR (400 MHz, $CDCl_3$) δ (ppm): 8.09 (s, 2H), 7.74 (d, J = 36 Hz, 2H), 7.56 (d, J = 36 Hz, 2H), 1.40 (s, 24H), 1.34(s, 24H). ^{13}C NMR (500 MHz, $CDCl_3$) δ 24.78, 24.83, 84.25, 84.59, 124.65, 129.78, 133.35, 137.60, 138.25, 142.60, 146.34; MS (MALDI-TOF) m/z = 858.29 (M^+); HRMS (ESI) m/z calcd for [$C_{42}H_{54}B_4O_8S_4^+$] 858.3073, found 858.3152.

Compound **TPB**

$Pd_2(dba)_3$ (16 mg, 0.017 mmol)and $P(MeOPh)_3$ (48 mg, 0.136 mmol)was added to the mixture of compound BDT-Th-4Bpin (128.7 mg, 0.15 mmol), compound PDI-Br$^{\alpha}$ (419.3 mg, 0.63 mmol), THF (12 mL) and 2M K_2CO_3 aqueous solution (3 mL) under nitrogen. The mixture was poured into methanol after refluxing 16 hours. The red precipitate was filtered and purified by column chromatography, using chloroform/dichloromethane = 1/3 as the eluent. 298 mg of pure TPB (73.8%) was obtained. M.p. 368 °C. ^{1}H NMR (500 MHz, $CDCl_2CDCl_2$) δ (ppm): 8.76-8.61 (Br, 28H), 8.14 (Br, 2H), 7.91 (Br, 2H), 7.52 (Br, 2H), 5.18-4.93 (Br, 8H), 2.20 (Br, 16H), 1.82 (Br, 16H), 1.33-1.14 (Br, 32H), 0.92-0.63 (Br, 48H). MS (MALDI-TOF) $C_{170}H_{154}N_8O_{16}S_4$ m/z: 2691.04; Found: 2692.11 $(M + H)^+$ Anal. Calcd for $C_{170}H_{154}N_8O_{16}S_4$: C, 75.81; H, 5.76; N, 4.16; S, 4.76. Found: C, 75.66; H, 5.71; N, 4.13, S, 4.84.

Materials and Characterization Techniques are similar to what described in Chapter 3, except for that Ag is used for device counter electrode instead of Al.The TPB:**PTB7-Th** devices showed bad stability under ambient condition. Therefore, EQE measurement was performed on devices after encapsulation using UV glue. However, the encapsulation procedure deteriorate the J_{sc} from 17.5, 18.1 mA/cm^2 to 15.2, 16.1 mA/cm^2 for TPB:**PTB7-Th** devices without/with 8% DPE as additive. The J_{sc} values calculated from EQE of sealed TPB:**PTB7-Th** devices without/with 8% DPE as additive are 14.5mA/cm^2 and 15.5mA/cm^2, respectively, which are all in less than 5% deviation from J_{sc} measured in sealed solar cell devices.

6.3 Conclusion

In summary, a new electron acceptor based on covalently bound clusters of alpha-substituted PDI was synthesized and exhibits promising potential for applications in OPV devices. The OPV device performance can be enhanced by using a small amount of DPE as co-solvent, which is accompanied by the improvement of hole/electron mobility. **TPB**-based devices also show the highest J_{sc} higher than 18 mA/cm^2, which is comparable with that of PC$_{71}$BM/**PTB7-Th** based solar cells. DFT calculation shows that four PDIs in the **TPB** molecular form a cross-like molecular geometry while they are still partially conjugated with the BDT-Th core. The effective photoluminescence quenching and charge dissociation probability measurements both demonstrate the efficient charge separation. The internal polarization is also important since EQE data showed significant contribution of charge generation from **TPB** within spectral range between 300-550 nm.

6.4 References

(1) Ala'a F. Eftaiha, a. J.-P. S., b Ian G. Hill*b and Gregory C. Welch *Journal of Materials Chemistry A* **2014**, *2*, 1201-1213.

(2) Lin, Y.; Wang, Y.; Wang, J.; Hou, J.; Li, Y.; Zhu, D.; Zhan, X. *Advanced materials* **2014**, *26*, 5137-5142.

(3) Kwon, O. K.; Park, J. H.; Kim, D. W.; Park, S. K.; Park, S. Y. *Advanced materials* **2015**, *27*, 1951-1956.

(4) Li, H.; Hwang, Y.-J.; Courtright, B. A. E.; Eberle, F. N.; Subramaniyan, S.; Jenekhe, S. A. *Advanced Materials* **2015**, *27*, 3266-3272.

(5) Holliday, S.; Ashraf, R. S.; Nielsen, C. B.; Kirkus, M.; Rohr, J. A.; Tan, C. H.; Collado-Fregoso, E.; Knall, A. C.; Durrant, J. R.; Nelson, J.; McCulloch, I. *Journal of the American Chemical Society* **2015**, *137*, 898-904.

(6) Lin, Y.; Wang, J.; Dai, S.; Li, Y.; Zhu, D.; Zhan, X. *Advanced Energy Materials* **2014**, *4*, 1400420.

(7) Yan, Q.; Zhou, Y.; Zheng, Y.-Q.; Pei, J.; Zhao, D. *Chemical Science* **2013**, *4*, 4389.

(8) Lin, Y.; Zhang, Z.-G.; Bai, H.; Wang, J.; Yao, Y.; Li, Y.; Zhu, D.; Zhan, X. *Energy Environ. Sci.* **2015**, *8*, 610-616.

(9) Zhao, J.; Li, Y.; Lin, H.; Liu, Y.; Jiang, K.; Mu, C.; Ma, T.; Lin Lai, J. Y.; Hu, H.; Yu, D.; Yan, H. *Energy Environ. Sci.* **2015**, *8*, 520-525.

(10) Lin, Y.; Wang, J.; Zhang, Z. G.; Bai, H.; Li, Y.; Zhu, D.; Zhan, X. *Advanced materials* **2015**, *27*, 1170-1174.

(11) Liu, Y.; Mu, C.; Jiang, K.; Zhao, J.; Li, Y.; Zhang, L.; Li, Z.; Lai, J. Y. L.; Hu, H.; Ma, T.; Hu, R.; Yu, D.; Huang, X.; Tang, B. Z.; Yan, H. *Advanced Materials* **2015**, *27*, 1015-1020.

(12) Lee, J.; Singh, R.; Sin, D. H.; Kim, H. G.; Song, K. C.; Cho, K. *Advanced*

Materials **2016**, *28*, 69-+.

(13) Zhao, D.; Wu, Q.; Cai, Z.; Zheng, T.; Chen, W.; Lu, J.; Yu, L. *Chemistry of Materials* **2016**.

(14) Zhang, J.; Singh, S.; Hwang, D. K.; Barlow, S.; Kippelen, B.; Marder, S. R. *Journal of Materials Chemistry C* **2013**, *1*, 5093.

(15) Richter, L. J.; DeLongchamp, D. M.; Bokel, F. A.; Engmann, S.; Chou, K. W.; Amassian, A.; Schaible, E.; Hexemer, A. *Advanced Energy Materials* **2015**, *5*, n/a-n/a.

(16) Lu, L.; Xu, T.; Chen, W.; Landry, E. S.; Yui, L. *Nature Photonics* **2014**, *8*, 716-722.